Feasibility Assessment of an Uncontrolled Nanosatellite Constellation Mission for Radar Depth Sounding of Ice Sheets

Bailey J. Miller

B.S. Aerospace Engineering, University of Kansas, 2017

Submitted to the graduate degree program in Department of Aerospace Engineering and the Graduate Faculty of the University of Kansas in partial fulfillment of the requirements for the degree of Doctor of Philosophy.

Committee members

Dr. Emily Arnold, Chairperson

Dr. Shawn Keshmiri

Dr. Mark Ewing

Dr. Richard Hale

Dr. John Paden

Dr. Carl Leuschen, Graduate Studies Representative

Date defended: August 30th, 2022

The Dissertation Committee for Bailey J. Miller certifies
that this is the approved version of the following dissertation :

Feasibility Assessment of an Uncontrolled Nanosatellite Constellation Mission for Radar Depth Sounding of Ice Sheets

Dr. Emily Arnold, Chairperson

Date approved: September 1st, 2022

Abstract

To improve ice sheet models used to estimate future sea level rise, major contributions must be made to ice thickness datasets. To date, ice thickness measurements have primarily been made by using depth sounding radars on airborne platforms, such as those fielded by the Center for Remote Sensing of Ice Sheets (CReSIS) group at the University of Kansas (KU). Measurements collected over the last three decades by CReSIS and other groups are used to produce bedrock elevation and ice thickness maps of the Antarctic and Greenland ice sheets. However, there are still large geographic areas that have never been sounded. In addition, the datasets used to generate the full bedrock Digital Elevation Model (DEM) are collected using disparate systems over large temporal baselines, which can result in interpolation errors. Proposed in this document is an uncontrolled orbital radar sounding constellation of nanosatellites designed to fill coverage gaps of the major ice sheets. Similar concepts have been proposed in the literature, but this work contributes a unique vehicle analysis for this uncontrolled orbital constellation mission. Nanosatellites are of interest due to the benefits of limited cost and development time. Given the small size of the vehicle, in order to achieve the necessary cross-track aperture size, a constellation is required. Using multiple antenna channels from individual satellites limits design complexity and implementation time for a single vehicle, while maintaining the benefits of multi-channel radar data collection. A primary design driver for this report is the use of current technologies to allow for rapid implementation after publication; thus only an uncontrolled constellation (the nanosatellites include no propulsion or station-keeping technology) is considered. The unique challenge of this design is determining the likelihood of success for an uncontrolled constellation, especially as it relates to the accuracy of launch vehicle jettison. Only the uncontrolled constellation is investigated but all of the concepts discussed in this document are relevant to a controlled mission concept, but the complexity of propulsion systems can greatly increase development time and cost; therefore the simplest solution

must be analyzed first.

This document presents the mission design in the context of other fielded airborne systems and uses the available literature to define mission requirements. These and other mission requirements are set to define an initial system architecture. This architecture includes radar operating parameters and analysis as well as defining satellite operations on-orbit and the accompanying satellite hardware. Satellites designed for this work utilized only Commercial Off The Shelf (COTS) hardware as the standard practices of commercial products will limit complexity and development time. Analysis of the power and data cycles of a single satellite showed that reasonable margin is present such that the battery does not fully deplete, the data does not accumulate too quickly, and nominal mission operations can be conducted for more than 40 orbits uninterrupted. Once defined, the architecture is then investigated from an orbital mechanics perspective. To do so required the development and validation of an orbit propagator. In the validation process, it was found that it is difficult to find propagation datasets to verify against; thus this document also provides a validation dataset for future assessments of this mission. By propagating the orbits of eight uncontrolled nanosatellites, considering perturbations from J2 and drag, the viability of this mission is fully evaluated. This evaluation is the major contribution of this work. Evaluating the constellation requires first defining the ideal orbital elements for each constellation constituent such that ideal spacing, as defined by radar array performance, is maintained over the targets and chance of collision is minimized during close approaches. The ideal configuration is evaluated as a baseline to determine the approximate data coverage as well as the Useful Mission Lifetime (UML). However, errors in orbital insertion play a major role in the ability to conduct this mission for a significant lifetime. Using a Monte Carlo analysis, the effects of orbital insertion errors is assessed to determine mission lifespan. The culmination of this evaluation is the first in-depth look at the orbital mechanics for uncontrolled multi-satellite proximity constellation missions.

It is shown in this report that an uncontrolled constellation is not well suited for this mission type. An ideal configuration of nanosatellites is found that utilizes offsets in Inclination, Right Ascension of the Ascending Node, and True Anomaly. This ideal configuration could collect over

100,000 line-km of data within 20 orbits. However, after 20 orbits it is expected that satellites in the constellation would collide leading to mission end and concerns of subsequent space debris. Similarly, it is found from the Monte Carlo jettison analysis that sub-millimeter accuracy is required in position and velocity for the launch vehicle to place satellites into the ideal configuration without excessive risk of collision. Considering the time to confirm with each satellite after jettison and the risk of collision, it is suggested that satellites should not be jettisoned directly into the ideal configuration, even for a controlled mission concept, should it be pursued. Future work beyond this report should focus on confirming that the controlled concept is capable of entering and maintaining the ideal configuration after jettison for a significant period of time. The Monte Carlo error analysis indicates that future concepts for this mission will not only require a propulsion systems, but will also require a system with the ability to accurately measure relative satellite spacing as small deviations from the ideal configuration will greatly increase collision risk.

Acknowledgements

Five years ago when I began my pursuit towards a PhD, I never would have expected that this is what I would contribute to my field. With the guidance, strength, and support of my advisor, I was able to accomplish this feat. For that and many other things, Dr. Emily Arnold, you have my sincerest thanks.

My family and friends were invaluable to me during this process. They lifted me up in my darkest times and motivated me in my most trying times. For that, and so much more, you have my love and my thanks.

Contents

List of Figures

List of Tables

Chapter 1

Introduction

Improving the ability to predict future sea level rise is critical to inform political and social actions needed to combat climate change. In 2019 the International Panel on Climate Change (IPCC), produced a special report indicating that climate change has reached the farthest corners of the Earth and immediate action is needed to measure and predict the effects[1]. Ice sheet models serve as a primary tool for integrating observations in the pursuit of predicting future sea level rise. Even with the well-established connection between the ice sheet mass balance and the global sea level, large uncertainties remain in prediction capabilities due to an incomplete understanding of ice sheet dynamics[2–5]. A key to improving these models is increasing our knowledge of ice thickness across the polar regions[6].

Highly accurate methods of measuring ice thickness, such as *in situ* borehole measurements, have the inherent problem of limited spatial and temporal coverage. The primary method for direct measurement of bed topography and ice thickness over large geographic areas utilizes ice sounding radars from airborne platforms. These airborne systems have made large contributions to the bedmap datasets of Antarctica and Greenland[7–11]. While airborne systems significantly extend the spatial coverage of measurement, the typical grid spacing of airborne measurements is around five kilometers which is much larger than the spatial resolution required for modeling ice sheet dynamics[12–15]. As such, modelers must use interpolation methods, like Kringing[16, 17] or mass conservation[18–20] to produce higher resolution grids of the bed elevation. While these interpolation methods have substantially improved modeling capabilities, the accuracy of such methods remains heavily reliant on nearby measurements[18–20]. Thickness estimates made using mass conservation interpolation can be off by more than 100 meters if not properly constrained and

these errors increase as the distance from the nearest measurement increases[19]. Interpolation methods can also suffer from large temporal baselines between measurements and measurements from dissimilar platforms.

Interpolation methods such as mass conservation can overcome temporal baselines by combining ice velocity measurements and ice thickness data in an optimum fashion. Morlinghem et. al. indicates that the error of mass conservation interpolation is inversely proportional to ice velocity and is best suited for fast flowing regions[19]. Regions of slow moving ice are not well suited for mass conservation interpolation, but Kringing interpolation can offer a more accurate estimation for these areas. Even with these complementary methods of interpolation, all methods are highly sensitive to errors in the input data[19]. Ice thickness measurements are susceptible to user bias as the different interface returns must often be "picked" manually and the results from two different radar systems over the same geographic area can vary a significant amount even when "picked" by the same user. Therefore, it is highly desirable to have ice-sounding data collected from a single system over a large geographic area over a short amount of time. Doing so will help to overcome the current disparities in the ice thickness datasets.

Several recent high-profile published works have emphasized the current disparity in the thickness data especially at the margins and near the grounding line[21–23]. An international action group, RINGS, of the Scientific Committee on Antarctic Research (SCAR) has set the primary goal of reducing gaps in data coverage of ice thickness and bedrock topography in the Antarctic[24]. An assessment by RINGS suggests that almost two-thirds of the Antarctic margin lacks any ice thickness data, thus these regions remain poorly represented in models. In a recent white paper (distributed via email), they indicate that, "bed topography is relatively well known for about one third of the Antarctic Margin. However, 58% of the margin has no data within 5 km, and 28% has no data within 20 km"[24]. An illustrative figure from the RINGS white paper is shown in Figure 1.1.

As indicated in Figure 1.1, large portions lack data within five kilometers of the margin. Modeling of the responses of outlet glaciers and the ice sheet margins is highly sensitive to bedrock

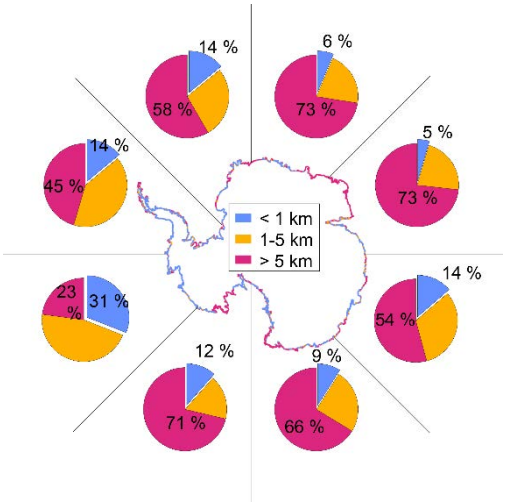

Figure 1.1: Radar Data Availability Near the Antarctic Ice Sheet Margin[24]

topography. This is especially true in the most critical regions of the ice sheets (e.g. near the grounding line) which remain poorly constrained due to the inherent difficulty of sounding these regions[15, 25, 26]. In order to successfully sound near the ice sheet margins will require lower frequency (e.g. HF) airborne systems. Spacecraft systems will not be able to sound these marginal areas but orbital sounding has the potential to collect data over large areas of the inland ice sheets.

Along with improving measurements near the margin, scientists have also emphasized that improved ice thickness and bed elevation measurements across entire ice sheets are critical to reducing model uncertainties[6]. Illustrated in Figure 1.2 and Figure 1.3 are detailed maps of sounding campaigns and interpolation methods used to generate the BedMachine Digital Elevation Model (DEM) of Antarctica and Greenland, respectively.

Figure 1.2 and Figure 1.3 show that ice thickness measurements from many different sounding campaigns over the last three decades have been used to develop the higher resolution elevation maps[16, 17, 27, 28]. However, there still remains large regions of the ice sheets that have never been sounded. Furthermore, ice thickness interpretation is affected by the fact that measurements are collected by disparate systems with varying operating parameters such as center frequency and bandwidth. As such, to address the need for larger spatial coverage across the remote landscapes with constant system parameters, a radar sounding platform capable of consistent and repeatable

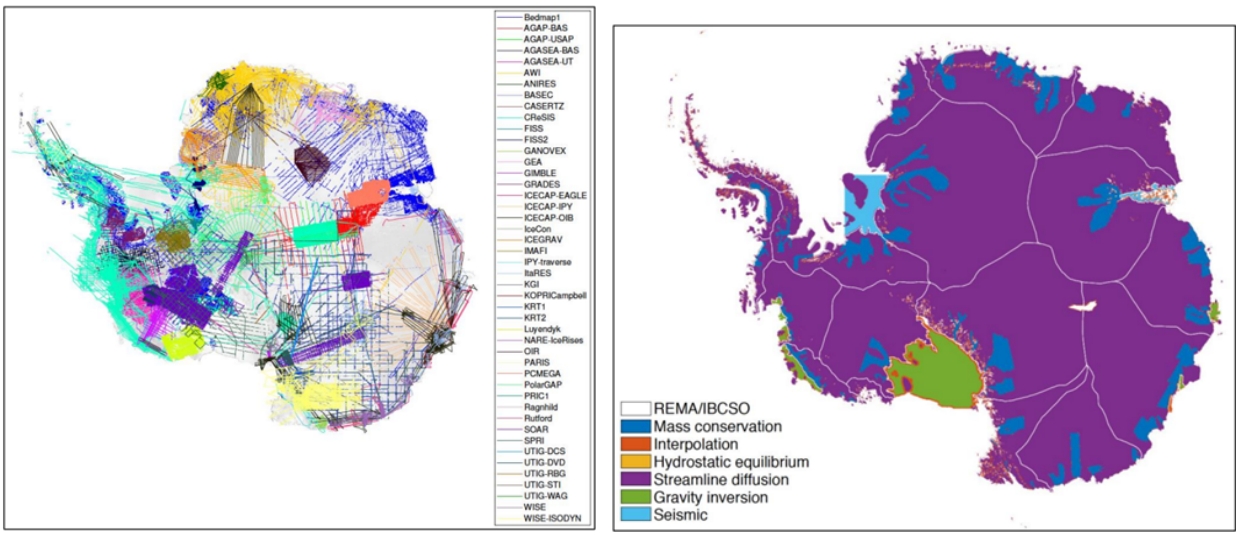

(a) Campaigns (b) Mapping Methods

Figure 1.2: Breakdown Images for Bed Machine Antarctica[27]

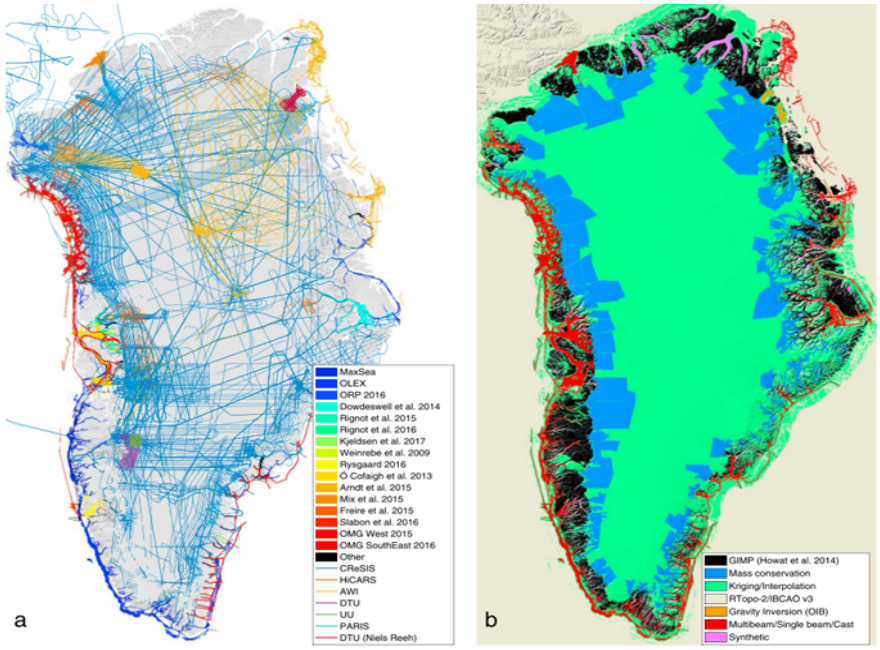

Figure 1.3: Campaign (a) and Mapping Method (b) Breakdown for Bed Machine Greenland[28]

measurements with broader coverage must be designed.

Airborne platforms have proven the operation of ice sounding radar architectures, but large-scale sounding campaigns remain limited by cost and personnel effort. These platforms are also constrained by the time of year as the winter months bring serious risks due to inclement weather and the perpetual darkness. Even the most experienced aircraft pilots will abstain from flying in

the polar regions during the winter months. For these and other reasons the solution for addressing the large coverage gaps must look beyond sub-orbital solutions.

The natural progression suggests that orbital platforms could be the key tool to filling gaps in ice sheet thickness datasets. In addition to several technical challenges that must be addressed, orbital sounding platforms have been prohibitively expensive and resource intensive. However, recent developments in nanosatellite missions have heavily reduced the cost and development time of orbital missions[29]. As such, these smaller and more versatile satellite platforms, such as CubeSats, can serve as a test platform for future large scale orbital depth sounding missions. Nanosatellites allow for rapid development and deployment necessary to increase the Technology Readiness Level (TRL) of critical payload hardware. In addition to proving the necessary technologies, researchers have proposed using a constellation of nanosatellites to execute orbital ice depth sounding[30].

By focusing on Commercial Off The Shelf (COTS) hardware, there are advantages in cost and development time for nanosatellite mission. At the time of writing, no COTS propulsion systems for nanosatellites are available. Therefore no position control will be considered. Detailed in this document is the architecture and analysis of an uncontrolled constellation of nanosatellites for radar ice depth sounding. Each nanosatellite within the constellation will have the ability to receive radar signals forming a phased antenna array. Radar signals will be transmitted by a single nanosatellite within the constellation. These satellites will not be equipped with station-keeping or propulsion technologies and thereby this mission will be referred to as an uncontrolled constellation[31]. Previous proposed orbital sounding designs have investigated satellite based solutions using a single, large spacecraft ($\geq$ 50 kg) with deployable antenna arrays; however, development of these designs led to potential cost overruns as well as intensive development of unique hardware systems to deploy the array on-orbit[32, 33]. A key advantage of nanosatellite platforms is the availability of COTS hardware.

COTS satellite hardware makes up the majority of nanosatellite designs with the aim of limiting development time for standard satellite subsystems[29]. The exclusion of a propulsion system was due to the lack of COTS hardware available at the time of writing as well as additional complexities

in design, implementation, and launch. Traditional nanosatellites are also inherently less expensive to launch as the mass is almost always less than 15kg making them an ideal secondary payload on nearly any launch vehicle. Launch opportunities are driven by desired orbital elements, mission complexity, and funding. Nanosatellites are a common secondary payload on most launch vehicles; secondary payloads launch at heavily reduced costs with limited adverse tradeoffs. However, an uncontrolled constellation of nanosatellites requires special considerations before and during jettison from the launch vehicle.

While several researchers have proposed similar orbital ice sounding concepts, none have investigated the feasibility from a vehicle standpoint. The main contribution of this work is a feasibility and performance assessment of the constellation mission detailed within. A detailed vehicle design will be outlined for this mission, which marks another unique contribution of this work. The study that follows will investigate the design and analysis of the spacecraft and constellation architecture necessary for this mission with considerations made to improve the ice-bed detection capabilities of the constellation. Once the ideal constellation configuration is established, a primary outcome of this work is determining the necessary accuracy required for a single launch orbital insertion of these uncontrolled spacecraft. Feasibility of this mission hinges on the achievable positions of the constellation and as such requires the thorough investigation detailed in this work.

This multi-disciplinary work combines and extends research in the areas of satellite design and ice sounding radars. This document begins with a literature review of 1) previously fielded airborne radar systems, 2) published orbital radar sounding concepts, 3) relevant nanosatellite/constellation missions, 4) launch vehicle jettison and collision risk mitigation, and 5) advanced signal processing techniques that improve the ability to detect the bedrock below the ice sheets. Conclusions drawn from this literature review are then used to define the a mission architecture.

Following the literature review, a system architecture of an uncontrolled constellation of nanosatellites for radar ice depth sounding is presented as the initial outcome of the iterative design process. This architecture focuses on the operational parameters of the radar with accom-

panying analysis and also presents the nanosatellite hardware needed to support the radar payload. Note that an in-depth assessment and design of the radar hardware is outside the scope of this work. Rather, this work will simply assume to support a future radar system. Note that the current TRL of radar hardware was considered during the design process. Following the definition of the system architecture, simulation tools are presented that analyze the mission from a satellite operational perspective.

Satellite simulations utilize an orbit propagator, which includes perturbations from J2 and drag, along with scripts for modeling satellite functionality while on-orbit with the goal of tracking power and data of nanosatellites within the constellation. The satellite functionality will be assessed for the proposed mission architecture to provide confidence in the detailed design. Following this functional assessment of the satellite, a separate in-depth assessment of the constellation orbital mechanics is conducted.

Utilizing the orbit propagator, the ideal orbital elements of each constellation constituent can be defined. The ideal orbits will be selected such that the array spacing while over the main ice sheet targets of Antarctica and Greenland is sufficient for radar operation. Simultaneously, the ideal orbital elements must be defined to minimize the chance of collision during close approaches between constellation constituents. The ideal constellation configuration is then evaluated by the metrics of data collected and Useful Mission Lifetime (UML). UML is a mission duration where the constellation can continuously collect significant datasets without any chance of collision. Notably, this ideal configuration cannot be attained without some amount of error in the orbital insertion process. As such, a Monte-Carlo simulation was done to evaluate the effects of errors in orbital insertion on data collection, UML, and chance of collision.

Following this in-depth assessment of the constellation, conclusions will be drawn as to the potential of an uncontrolled constellation of nanosatellites for radar ice depth sounding. This assessment is the first evaluation of an uncontrolled multi-satellite proximity constellation for an ice-sounding mission and as such is a significant contribution of this work. Another significant contribution is the detailed vehicle design for this mission type. Goals of this work include a

detailed vehicle and mission architecture to conduct orbital ice-depth sounding, an ideal constellation configuration that can collect significant amounts of data over the Antarctic and Greenland ice sheets, and a Monte-Carlo study to determine the required orbital insertion accuracy of the constellation.

Chapter 2

Background

Before presenting the constellation mission concept proposed in this report, it is relevant to review the available literature. The mission concept proposed is an uncontrolled constellation of nanosatellites for radar ice depth sounding. To provide context for the selected radar parameters used in the mission design, a survey of fielded airborne ice-sounding radar systems is conducted and presented. Theoretical concepts of orbital platforms for radar ice depth sounding have been published in the past, but all have remained theoretical and have not assessed designs to the level presented in this work. Even so, it is critical to review these theoretical systems to fully understand the mission requirements and build on the operational attributes presented for fielded radar systems.

In designing an uncontrolled constellation of nanosatellites, it is necessary to review other uncontrolled constellations to draw similarities and provide context to the types of mission designs that have been flown. As this mission is uncontrolled, a review of jettison operations for nanosatellites and necessary considerations for constellations is also presented. Jettison from the launch vehicle, also referred to as orbital insertion, is the main error source in this mission concept and thereby drives the potential mission success.

Mission success also hinges on the ability to post-process the collected radar data with advanced signal processing techniques. A review of these techniques is also presented in this chapter along with considerations for the limits of the processing capabilities. Limits gathered from this review are used to define the acceptable constellation configurations. Properly implemented, these techniques will improve the ability to detect faint signals from the ice-bedrock interface and as such are necessary in establishing the expected link budgets of the constellation.

2.1 Fielded Airborne Ice-Sounding Radar Systems

A survey of fielded ice-sounding radar systems is presented in this section. The purpose of this survey is to inform the selection of radar operating parameters for the proposed constellation mission. The main parameters of interest are: transmit power, center frequency, bandwidth, and pulse width. For this survey, there is a focus on radar ice depth sounders, specifically those operated from airborne platforms. The four main systems investigated are Multichannel Coherent Radar Depth Sounder (MCoRDS)[7, 8], Warm Ice Sounding Explorer (WISE) [9, 10], High Capability Radar Sounder (HiCARS)[11], and a system from the Alfred Wegner Institute (AWI)[34]. These systems were selected because they contributed most significantly to the spatial extent of measurements while also capturing the range of operating parameters common among ice-sounding radars. The operating attributes of these radar systems are presented in Table 2.1.

Table 2.1: Sounding Radar Comparison

System	Center Frequency (MHz)	Bandwidth (MHz)	Pulse Width (μs)	Transmit Power (W)	Antenna Elements (#)	Operator	Citation
MCoRDS	195	30	1 - 30	1200	16	CReSIS	[7]
WISE	2 - 5	1 - 3	1 - 5	<100	1	JPL	[10]
HiCARS	60	15	1	8000	2	UTIG	[11]
AWI	150	20	0.06 - 0.6	1600	2	AWI	[34]

The MCoRDS radar system was developed by the Center for Remote Sensing of Ice Sheets (CReSIS) group at the University of Kansas (KU). This system was optimized to sound fast-flowing glaciers and ice sheet margins with the capability of sounding ice sheets that are more than three kilometers thick[7]. Nine unique configurations of MCoRDS have been flown on six types of aircraft over the last 25 years[35]. Range resolution of this radar is between 6-20 meters depending on the configuration and signal processing techniques applied. Up to 15 antenna elements have been utilized to form a phased array which contributes to cross-track clutter reduction. The large antenna array is unique to the MCoRDS as seen from Table 2.1. Several iterations between 1993 and 2018 were flown over both the Antarctic and Greenland ice sheets. These campaigns serve as

a major contributor to current ice sheet thickness datasets, with 337,650 line kilometers used for recent Greenland bed elevation datasets[16].

WISE was developed as a proof-of-concept system for ice-penetrating radars to explore extraterrestrial ice sheets such as the icy moons of Jupiter[10]. NASA's Jet Propulsion Laboratory (JPL) operated this radar over the Greenland ice sheets utilizing a Twin Otter airborne platform[16]. Unlike MCoRDS, the WISE system only utilizes a single antenna element. Coupled with the relatively low center frequency, WISE is best utilized on the temperate and polytemperate glaciers with a vertical resolution of 20 meters[10]. Between 2008 to 2010, the WISE instrument collected 13,180 line kilometers of data that was utilized by Greenland bedmap datasets[16].

Like WISE, the HiCARS radar system was developed as an Earth-based test platform for orbital radar sounders. Development of HiCARS was a multi-institution effort led by the University of Texas Institute for Geophysics (UTIG) with contributions from JPL and KU. Multiple campaigns in both Antarctica and Greenland utilized the HiCARS system on a Twin Otter aircraft[11]. By applying signal processing algorithms such as pulse compression and unfocused Synthetic Aperture Radar (SAR), the HiCARS system is capable of achieving 10 meter range resolution[11]. From a 2011 Greenland campaign, the HiCARS instrument contributed 5,270 line kilometers of collected bed map data[16].

The airborne radar system fielded by AWI was developed for mapping ice thickness as well as internal layering of glaciers up to four kilometers thick. Vertical resolution of this system ranges from five to 50 meters depending on the pulse duration[34]. A Dornier 228-100 aircraft was the main platform used to field this radar system in both Antarctica and Greenland. Between 1996 and 2010, this radar contributed 58,350 line kilometers of ice thickness data used for Greenland bed maps[16].

Radar systems presented in this section provide context to the current capabilities and operating parameters for measuring ice sheet thickness using radar sounding techniques. These systems have contributed over 414,000 line kilometers of ice thickness data to the Greenland bedmap datasets[16]. As noted, this data has been collected over the course of 20 years. All of this data

provided interpolation points necessary to generate a full map of the Antarctic and Greenland ice sheets. Although it is a massive dataset, the large temporal baselines and dissimilarity between systems can cause large errors in the interpolation process. New sounding mission concepts, such as nanosatellite constellations, must be developed which can collect large amounts of thickness data over short temporal baselines and with consistent operating parameters. The next section reviews orbital concepts that have been presented for ice-sounding from space.

2.2 Orbital Mission Concepts

Due to advantages in spatial and temporal coverage as well as recently achievable mission costs, several researchers have recognized that one of the next steps in improving ice thickness datasets is developing orbital radar sounding platforms. The various conceptual missions presented in this section were developed to sound terrestrial ice sheets from Low Earth Orbit (LEO). Discussed in this section are the following concepts: Glacier and Ice Sheet Mapping Oribter (GISMO)[32], POLARIS[33], and Polar Inclined CubeSats (PICS)[30]. The operational parameters for each of these concepts is presented in Table 2.2.

Table 2.2: Orbital Sounding Concept Comparison

System	Center Frequency (MHz)	Bandwidth (MHz)	Pulse Width (μs)	Transmit Power (W)	Antenna Elements (#)	Citation
GISMO	130 or 435	6	20	5000	2	[32]
POLARIS	435	85	50	100	4	[33]
PICS	150	10	N/A	50	50	[30]

GISMO is proposed to serve as a spaceborne interferometric sounder. With a suggested polar orbit of 600 kilometers altitude, this single satellite concept utilizes two 12.5 meter mesh reflector antennas that can operate at both 130 and 435 MHz. Requirements of GISMO focused on measuring ice thickness ranging from 100 meters to five kilometers with an accuracy of 20 meters. From the published work, the researchers suggest that the entirety of Antarctica and Greenland could be mapped six times over with an Signal-to-Noise Ratio (SNR) of 35.3 dB for the bedrock return and

2.9 dB for the ice surface return based on a noise power of -132 dBW[32]. Note that this SNR value includes gain from post-processing techniques such as SAR (+37.3 dB of SAR gain) which emphasizes the necessity for advanced signal processing techniques. However, this design lacks clarity on the link budget as well as details on the supporting satellite platform. Both items are critical for assessing the ability to execute this mission profile.

Denmark Technical University (DTU) developed and subsequently fielded the POLARIS radar from an airborne platform with the intention of proving the capability of P-Band orbital radars. Similar to GISMO, POLARIS utilizes a 435 MHz center frequency (P-Band). The goal of this radar was to sound ice sheets up to four kilometers thick. As mentioned, this radar has been fielded on a Twin Otter platform to prove the operational concepts[36]. Though the sub-orbital system was successful, follow-on studies asserted that this P-Band radar could not operate from an orbital platform as clutter would obscure the basal return[33]. These follow-on studies are analyzed further in Section 3.1. Like GISMO, the conceptual orbital design of POLARIS neglects to discuss the actual satellite platform required to field this mission.

Unlike the other two concepts, the PICS concept would utilize multiple nanosatellites in a constellation to form a large cross-track array. 50 satellites would be launched into a polar orbit with an altitude of 400 kilometers, spaced 50 meters in the along track and one meter in the cross track direction. Each satellite would be capable of transmitting and receiving radar signals centered at 150 MHz. With a reported SNR of 10.7 dB, this concept was designed to sound ice sheets up to five kilometers thick. Notably, this concept also featured a Ka-Band radar on each satellite for inter-satellite communication necessary for ranging, downlink, and transmitter phase-lock of the VHF sounding radar[30]. It was expected that this radar could achieve 20 meters of range resolution. The PICS design includes some details about the satellite design requirements but falls short on selecting high TRL hardware. The authors reference spacecraft modules that are being developed by universities, but modules from these providers would require a significant amount of implementation and development time as it may not meet nanosatellite industry standards. Although the authors provide analytical evidence to indicate expected mission success based solely

on the link budget presented, the lack of analysis on the spacecraft design or constellation feasibility serves as a large gap that must be filled for orbital ice sounding mission concepts.

The concepts discussed above all indicate that orbital radar ice-sounding is potentially viable from a radar operation standpoint especially when using multiple antenna elements and utilizing advanced signal processing techniques. However, none of these concepts discuss the ability of the spacecraft to conduct the mission. Importantly, the multi-satellite mission concept PICS does not address the constellation configuration at all beyond defining offsets during operation. Spacecraft constellations will naturally have varying positions based on orbital mechanics and many spatial criteria are relevant to mission success. This report aims to fill this gap in knowledge, specifically with respect to uncontrolled constellations. Not only does this report conduct analysis and simulations similar to the above works, but it extends current work by assessing the satellite and mission design.

Each of these published designs note certain obstacles that must be overcome for orbital depth sounding. Most notably is clutter reduction. Synthetic Aperture Radar (SAR) is mentioned multiple times as a key tool for reducing along-track clutter. All of the works noted that utilizing multiple receive channels and combining the data with techniques such as Minimum Variance Distortionless Response (MVDR) can reduce cross-track clutter. As these techniques are expected to be vital to mission success, they must be reviewed in the context of orbital sounding missions.

2.3 Advanced Signal Processing

Modern radar systems are designed such that signal processing algorithms can provide the most benefit to Signal-to-Noise Ratio (SNR). Signal processing focuses mainly on reducing clutter sources and isolating data from the targets of interest, which are the air-ice and ice-bedrock interfaces for radar ice depth sounding. Clutter is defined as undesirable signals that can mask the signal of interest, especially the low power signals from the ice-bedrock interface. Canceling or heavily reducing these clutter signals with advanced signal processing increases the SNR, no matter the platform.

Presented in this section are three common signal processing techniques used by CReSIS to improve the detection of the ice-bed interface. These include SAR, multi-channel, and multi-pass algorithms. Included in this section is a discussion of the sensitivity of signal processing to position offsets (known and unknown) of antenna elements in the array. Position offsets from an ideal phased array will reduce the ability to sound ice sheets and an uncontrolled constellation must be designed as to maintain reasonable offsets during the lifetime of the mission.

Most CReSIS radar utilize multiple channels[37] and as such CReSIS has developed many algorithms specifically for processing and combining multiple phase centers[8]. The first step in post-processing is the application of a SAR algorithm. In this step, each element in the array is treated separately. For each, the position is tracked and compensated to align the measurements from each element. After which, the signals along a given aperture length are coherently summed to reduce along-track clutter. To achieve the best results with this algorithm, the attitude and position of the antenna elements need to be well known[8]. This knowledge is also required for other post-processing algorithms such as array processing (also known as multi-channel).

Minimum Variance Distortionless Response (MVDR) is a well-known and often used array processing technique that combines the data collected by multiple elements within an array to minimize interference and noise signals while preserving the desired signal. Given a look direction, MVDR utilizes the correlation between the data collected by each antenna element to find and subsequently null the return power at look angles of interference signals, also referred to as clutter. Different implementations are able to automatically place nulls or place nulls at prescribed look angles. Similar to SAR, this method is heavily reliant on position knowledge of each antenna element and compensating for motion of each element.

An investigation into the effects of position error on multichannel algorithms such as MVDR was done by the author in previous work[38]. Satellite constellations will suffer from these positional errors for a number of reasons; namely, orbital jettison accuracy and orbital drift over time. The previous study by this author focused on the beamforming sensitivity of MVDR by introducing known and unknown positional errors for the elements of an antenna array[38]. Known positional

errors are defined as measured offsets from the ideal antenna element position while unknown positional errors can be thought of as the accuracy of that measurement. To determine the effects of these offsets, a set of Monte Carlo simulations were executed which randomly varied the known and unknown position of antenna elements within an array and then measured the SNR after applying MVDR with only the known position available to the algorithm. This study concluded that if the unknown positional errors are smaller than 25% of the wavelength, that all known positional offsets up to 200% of the wavelength can still be compensated. The study also found that increasing the number of elements in the array increases the ability to compensate for measured offsets. The study analyzed arrays with three and eight antenna elements to compare the results. It is expected that increasing the number of elements would have diminishing returns when compensating for measured offsets. As such, the number of elements for an orbital radar sounding array should be greater than three but less than or equal to eight so as to keep a small array size while maintaining the benefits of signal processing techniques such as MVDR.

Previous work by the author also focused on developing and analyzing algorithms for multi-pass measurements[39]. Multi-pass, or repeat pass, measurements are defined as radar sounding data collected over a particular scene along the same or very similar trajectory but offset in time. As CReSIS has been operating and collecting data for over 30 years, there is a plethora of datasets over similar geographic locations and with very similar flight trajectories. Over the years, there are several flightlines that have been flown and reflown with minimal position offset for the purpose of later being leveraged for multi-pass algorithms. It was shown that the algorithm, presented in [39], could compensate for positional offsets and combine separate channels across a temporal baseline. The combined data forms an interferogram which can be used to interpret the vertical displacement of the ice sheet between the datasets. This algorithm was the first successful implementation of interferometric SAR techniques on multi-channel airborne ice-sounding data. Applying this algorithm to orbital systems yields a new technique that could indicate changes in the ice sheet over time, given a sufficiently large temporal baseline ($\geq$ one year), or improve depth measurements, only for short temporal baselines ($\leq$ one month).

While these techniques can improve the detection capability of a phased array radar system, the spacing of antenna elements is critical to mission success. Before moving on to simulation and analysis of the constellation concept, it is first relevant to review other nanosatellite constellation missions.

2.4 Flown Nanosatellite Constellations

The design of any mission concept benefits from reviewing previously executed missions of a similar type. The proposed mission is defined as an uncontrolled constellation of nanosatellites. Multi-satellite missions normally fall under two broad designations: constellation, and formation flying[31]. Formation flying defines missions in which constituents must track their state based on the relative state to a leader satellite and adjust position based on this relative control law. Formation flying missions must have some sort of station-keeping or propulsion technology to adjust the orbital position. Constellations can also utilize propulsion, but the satellite constituents of a constellation adjust their position based only on their individual position rather than a lead satellite as in formation flying. When a constellation mission utilizes propulsion to maintain or adjust orbital position, this is designated as a controlled constellation. Without propulsion or station-keeping technology, the multi-satellite mission is referred to as an uncontrolled constellation[31]. Erego, the mission concept investigated in this report is deemed an uncontrolled constellation.

In 2016, Chung et. al published a review of 39 constellation and formation flying nanosatellite missions. Of these 39 missions, 19 were qualified as uncontrolled constellations. Three of the successfully launched missions were selected and detailed in Table 2.3. These three were selected as the missions have been launched and information was available through published literature. The other uncontrolled constellations either have not flown yet or have no information available beyond the aforementioned review.

The DICE mission was a two spacecraft constellation launched in 2011 into an eccentric polar orbit with an apogee altitude of 800 kilometers. The two 1.5U nanosatellites were jettisoned with the same dispenser but with slightly different jettison velocities to allow the satellites to gradually

Table 2.3: Flown Uncontrolled Constellation Missions

Mission	Institution	Orbit Type	Payload	Sources
DICE	Utah State University	Polar	Earth Science	[40]
FIREBIRD	Montana State University	Polar	Earth Science	[41]
Prometheus	Los Alamos National Lab	Equatorial	Technology Demonstration	[42]

separate over time[40]. The objective of this mission was to study space weather events and their effects on Earth's atmosphere. Successful measurements were made by the team but there is no indication of the current status of this constellation.

There are two primary FIREBIRD missions: FIREBIRD-I and FIREBIRD-II. These missions were launched into polar orbits in 2013 and 2015 respectively. Each mission had two complementary 1.5U nanosatellites that would study high energy particles in Earth's radiation belts with a focus on microbursts[41]. FIREBIRD-I was not able to make simultaneous measurements from both satellites as they were not able to communicate with one satellite for several months after launch, and the second satellite did not operate for longer than two months after launch. By the time communication was established with the FIREBIRD-II satellites an hour after launch vehicle jettison, their separation was nearly ten kilometers. FIREBIRD-II was much more successful as the team was able to collect data from both satellites simultaneously for four years.

Prometheus is the most comparable mission to the concept proposed in this document. This mission launched eight satellites in 2013 to a circular orbit of 500 kilometers in altitude and 40.5 degrees inclination. The objective of this mission was to demonstrate the ease-of-use, reduced cost, and reduced development time for nanosatellite platforms[42]. This includes improving communication and control capabilities following the previous success of the Perseus mission conducted by the same institution. It was indicated that this mission was a success and would be followed by other constellation missions.

All of the uncontrolled constellations reviewed in this document and other literature sources lack significant details on the achieved orbital spacing between constellation constituents. This relative spacing is highly relevant to the study presented in this document but makes sense as all of these uncontrolled missions specified satellite separation of much greater than one kilometer. However,

several controlled and formation flying multi-satellite missions did work to achieve proximity operations with nanosatellites.

CanX-4&5 mission is particularly relevant as this was the first and most well-known nanosatellite mission to operate nanosatellites in proximity to each other and maintain specific spacing throughout the lifetime using propulsive methods[43]. The formation flying mission of CanX-4&5 was launched in June 2014 with the express intent of demonstrating formation flight for multiple nanosatellites. The two spacecraft were launched from the Polar Satellite Launch Vehicle (PSLV) and injected separately to LEO with an inclination of roughly 52 deg. Three days after launch, the spacecraft were at a distance of 200 km. After the spacecraft were determined to be fully operational, in late July, the spacecraft were at the maximum distance of 2300 km apart and the researchers determined it was time to conduct the main mission of reducing this distance to 50 m. By September, the team had achieved their goal with only 2.032 m/s of delta-V expended out of the total 18 m/s that was allowed by their propulsion system[43]. The two satellites did several formation flying maneuvers with different spacing requirements over the next year. The researchers note that all nominal mission objectives were completed in the first year with a significant fraction of delta-V remaining and that the satellites were still operational in 2016.

Although the benefits of propulsion/station-keeping technologies are recognized, they will not be considered for this work. In the chapters that follow, a driving motivation is to reduce development time and cost by implementing COTS hardware. To date, there are no commercially available propulsion systems for nanosatellites. There are several propulsion concepts that have a high TRL, such as NANOPS for the CanX-2 mission and CNAPS for the CanX-4&5 mission[44], but these are one-off systems that were not made for general commercial needs. The estimated material cost for these systems was less than 20,000 Canadian dollars. It is reasonable to expect that commercially available systems, with all costs accounted for, would be as expensive as 40,000 dollars.

Other station-keeping (or cluster-keeping) techniques that do not involve propulsion have also been proposed. Specifically in the realm of differential drag. An original concept from the Israel

Institute of Technology proposed a three-satellite formation that would be used for geo-location of target signals on Earth, known as SAMSON. It is not clear what the current status of this mission is but some research regarding SAMSON was first published in 2013. The 2013 publication looked at the theoretical concept of using actuated solar panels to control the amount of differential drag for each satellite to maintain the formation[45]. Results showed that station-keeping with differential drag was theoretically possible up to 600 kilometers of altitude. However, more recent publications of the project from 2019 indicate that a cold-gas propulsion system will be used for station-keeping[46]. Even so, the original 2013 analysis provides an interesting result that could be considered in future iterations of this design concept. A differential drag technique would require complicated actuation of a large panel to control the drag. Actuated solar panels do exist[47], but these are not intended to change angle during flight. Purchasing a deployable 6U solar panel would cost 45,000 dollars, which is three times the cost of a standard 6U solar panel[47]. A properly actuated 6U solar panel would certainly be more expensive than both and require significant further development.

In the effort to minimize development time and mission cost, the uncontrolled constellation concept is worth investigating. It is known that the main source of deviation in the designed orbital mission will occur in the launch vehicle jettison phase. Concepts with a propulsion system would be able to compensate for these deviations, but the uncontrolled constellation that is investigated in this document can not. As such, the relevant concepts and details given in the literature regarding orbital insertion of nanosatellites is reviewed in the following section.

2.5 Launch Vehicle Jettison and Collision Avoidance

Every orbital mission begins with a launch that takes the satellite from Earth's surface to the specified orbit. However, the orbit that is achieved may vary from the desired mission orbit. From the publicly available SpaceX Falcon 9 User Manual, they indicate that the achieved orbit can vary by ±15 kilometers in apogee or perigee and can vary by ± 0.1 degrees in inclination[48]. Notably, SpaceX indicates that integration to the launch vehicle is the responsibility of the customer. Most

nanosatellite missions utilize the PPOD dispenser concept[49]. These dispensers can hold multiple nanosatellites and are able to eject a four kilogram satellite at two meters per second but without an accuracy indicated[49]. For missions with multiple satellites SpaceX indicates that each satellite can be placed in a different orbit as the launch vehicle has restart capability. This capability is highly desirable for the uncontrolled constellation concept as the satellites cannot adjust their orbit once jettisoned from the launch vehicle. However, the accuracy of these separate insertions is not detailed in the user manual or in any other available resource. This is a critical unknown as the success of the proposed mission concept is driven by precision placement in the desired orbital planes. Some researchers, reviewed below, have noted that timing and position of individual satellites is a flexible process if the mission is the primary payload. Even so, the accuracy of the timing, position, and velocity of these operations are not publicly available. As such, this report will need to work backwards to define the accuracy required for orbital insertion operations. Any deviations from the desired orbits will impact mission success and can lead to collision between constellation constituents.

Multi-satellite missions from a single launch vehicle have been studied in the literature to determine the best strategies for orbit injection while avoiding collision and maintaining spacing criterion. However, all studies to this point have looked at controlled maneuvers after injection to correct the constellation. Ergo, only satellites with propulsion systems have been studied. It is clear that propulsion gives an advantage in this phase of flight, especially when the constellation is the secondary payload on a launch vehicle. Secondary payloads have less influence on the initial orbits that are achieved as well as timing and positioning of the individual satellites at orbital injection. Even though these studies do not cover the exact scenario of interest in this paper, an uncontrolled constellation of nanosatellites, it is still worth reviewing their findings.

Earlier, relevant multi-nanosatellite mission concepts were presented in Section 2.4. Each mission in that section was classified as either a constellation or formation flight. When a formation flight mission has to operate under minimum and maximum distance constraints, it can also be referred to as a cluster flight. Importantly, these cluster missions must have some method of

adjusting position on orbit (i.e. propulsion, differential drag) so that distances can be maintained during the mission. Several authors have investigated this type of mission from an orbit injection stand point and devised jettison schemes worth mentioning in this literature review.

Wen et al. investigated the orbit injection strategy of the SAMSON mission by investigating the orbital injection scenarios of this mission as a secondary payload on the PSLV and Dnepr launch vehicles[50]. To conduct this study, they derive the dynamics and controls equations necessary for this controlled mission. Then, they conduct an investigation to find the ideal injection scenario for the SAMSON mission. The SAMSON mission required a cross-track distance of less than 50 km with much larger distances allowed in along-track (up to 200 km). At outset, the injection would offset the satellites in Right Ascension to achieve the necessary cross-track offset for the mission but found that this may not be possible for the PSLV or the Dnepr launch vehicles because they indicate that these vehicles cannot release the nanosatellites into multiple orbital planes. In lieu of this disadvantage, they devised an injection scenario that required the launch vehicle has the ability to change its orbital velocity and position between satellite jettisons to meet the requirements for the subsequent satellite jettison. The SAMSON mission consists of three 6U nanosatellites with propulsion systems, therefore slight deviations in the orbit injection process can be handled. By way of a Monte Carlo study of injection timing, position, and velocity, the researchers found the acceptable injection scenario. The next step for them was to understand the cluster-keeping (or station-keeping) requirements of each satellite to understand the propellant requirements to maintain the specified mission spacing. From the cluster-keeping results, they found that 113 grams of fuel would need to be expended for these 7.98 kilogram satellites to maintain position for one year[50]. Based on the propulsion system for SAMSON, this relates to roughly 5 m/s of delta-V out the total 20 m/s prescribed[46]. They conclude the study by indicating that a large amount of fuel had to be expended because the launch vehicles were not maneuverable after proper jettison. This indicates that if a launch vehicle is properly maneuverable, it may be possible to expend little or no fuel to reach the initial configuration and maintain it for a significant period of time.

A similar study by Yoon et al. starts by recognizing that most nanosatellite missions will not

have propulsion systems or means of control after orbit injection[51]. Part of their study investigates the effects of differential drag control to aide in orbit correction. Reignition or maneuverability of the launch vehicle between satellite jettisons is not allowed by their analysis as they indicate most secondary launches will not have this flexibility. After presenting the relevant equations for orbit propagation, they present an investigation of the deployment of multiple nanosatellites where the injection order and injection direction are the mission setup variables. This mission had allowable relative offsets on the order of 10's of kilometers. Using this result, they also conduct a drift analysis of this same mission. Interestingly, they include the perturbations of J2 in their orbit propagation but point out that atmospheric drag is not considered at the orbital altitude of 580 km. They then go on to investigate differential drag for the same constellation. The main results of their study are that 90% of collision probability occurs within the first 10 minutes after flight and after the first orbit the collision risk approaches zero[51]. It is worth noting that the spacing requirements of this mission were to keep the satellites within a relative distance of 400 kilometers which is significantly larger than the offsets required for the mission highlighted in the following work.

The above studies serve as a good reference to the key investigation criterion going forward. It is clear that collision risk within the first few orbits must be investigated and after which point the relative drift of constituents should drive the investigation. However, the mission investigation that follows is unlike the above as the relative positions of the satellites are on the order of meters rather than kilometers. As such, the following work is unique to this design space. Special care must be taken to avoid collision throughout the entire mission duration as the satellites will operate in much closer proximity compared to the above investigations. As the following mission will necessarily be the primary payload of the launch vehicle, maneuverability of the upper stage will be allowed to properly orient and distance the spacecraft at orbit injection.

Chapter 3

Initial System Architecture

Designing a system for orbital radar ice depth sounding is an iterative process that considers the expected performance of the radar system as well as performance of the satellites within the constellation. A constellation is considered for this mission to reduce cost and complexity in satellite development. Tools required to simulate mission performance are developed and discussed in following chapters. To enter the design loop an initial set of system parameters must be established. The following sections detail the initial architecture for the uncontrolled constellation of nanosatellites for radar ice depth sounding, hereto referred as Kansas' Remote Ice Sounding Platform (KRISP).

This chapter covers the selection of relevant parameters for the radar payload, which include radar geometry and operational parameters. Given a radar definition, an initial analysis of the expected performance is conducted via link budget.

After establishing the payload, the mission requirements are detailed based on the background information, payload requirements, and spacecraft design practices. Once the requirements are detailed, a Concept of Operations (ConOps) is identified to support the radar sounding mission. Finally, a satellite design is defined to satisfy all requirements outlined in this chapter.

Before beginning the design process, conclusions from the published works presented in the previous chapter should be considered. Design considerations drive certain mission parameters that influence the design process. To start the iterative design process, driving orbital elements of the constellation need to be defined. Establishing these allows for proper analysis and discussion of expected mission performance. After orbit selection, the radar operations will be defined based on fielded radar systems and other proposed orbital radar concepts covered in Chapter 2. A link

budget analysis will also be done to understand the expected performance of the radar. Lastly, this chapter will define the subsystem hardware properties of the satellites in the constellation followed by an analysis to verify the design.

3.1 Design Considerations

The purpose of the previous chapter was to provide background information relevant to the design of an orbital ice sounding radar mission. In order to properly design this mission, all of the concepts presented in Chapter 2 will need to be brought together for the first time. Certain design considerations should be gleaned from these published works to narrow the optimal design space.

Orbital sounding concepts presented in Section 2.2 have several similarities in their concepts of radar operations. Two of these designs rely on a P-Band (or UHF) radar to sound ice sheets. Other works by Culberg et. al. and Dall et. al. have conducted feasibility studies of these UHF designs to elaborate on previous analyses[33, 52]. Culberg et. al. showed that orbital UHF radar systems (specifically above 200 MHz) would increasingly suffer from firn layer clutter as the frequency increases. This result was established by electromagnetic modeling of the first 100 meters of an ice sheet column and investigating the effects of volume scattering due to air inclusions as well as the effects of firn scattering.[52]. The conclusion drawn by Culberg et. al. states that VHF systems with center frequencies less than 200 MHz are the more ideal choice for orbital radar ice depth sounding. Dall et. al. found similar conclusions when conducting a feasibility study for the POLARIS orbital mission concept. They indicate that firn clutter would obscure the radar return from the bedrock below the ice sheet for P-Band systems[33]. To do this, they set up electromagnetic simulations of common ice sheet scenarios based on data collected with the POLARIS radar on an aircraft platform. These scenarios covered a sweep of ice thickness, glacial flow velocity, and attenuation attributes available in literature and previous airborne radar sounding campaigns[33]. For two-thirds of the simulated scenarios, the authors found that clutter and/or thermal noise would obscure the radar return from the bedrock bottom for a P-Band (or UHF) orbital sounder[33]. The results of these feasibility studies suggest limiting the selection of orbital radar operating frequency

to be less than 200 MHz to minimize clutter sources from obscuring the radar return from the bedrock below ice sheets.

Considering both the airborne and orbital concepts reviewed in the previous chapter, it is necessary to address common features that improve the ability to effectively map ice sheet thickness. As mentioned above, orbital sounding is most likely to be effective when executed at VHF frequencies, specifically those below 200 MHz[52]. Considering the frequency allocations from the Federal Communications Commission (FCC) at VHF frequencies, there are several bands that could be suitable for radar operations. A portion of the frequency allocations between 128 and 150 MHz are shown in Figure 3.1[53].

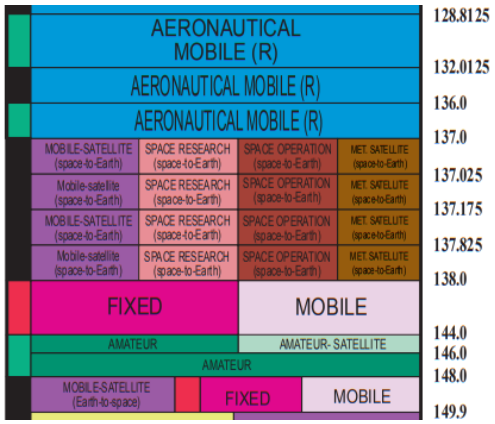

Figure 3.1: Portion of FCC Frequency Allocation Table between 128 and 150 MHz[53]

From Figure 3.1, two major bands appear that could be utilized for this mission concept. The first band is from 137 to 138 MHz which is designated for space research needs, like those indicated in this project. The second is much wider and less defined, this band being allocated for amateur operations between 144 and 148 MHz. It may be possible to span both bands (137-148 MHz) with the proper licensing but that requires significant coordination with the FCC. The larger bandwidth would relate to an improved range resolution which is desirable for this mission. This second band of 144-148 MHz will be selected going forward as the available bandwidth is larger and at least one iteration of the MCoRDS operated around this frequency band[35]. Like the MCoRDS, this mission design should implement multiple antenna elements to form an array.

The configuration of the antenna elements within the proposed nanosatellite constellation

should form a uniform linear array. However, it is known from previous works that offsets from the ideal array configuration (or position) can be compensated for if these offsets are measured with sufficient accuracy[38]. The sufficient accuracy (or unknown offsets) must be within 25 percent of the wavelength. Therefore, position measurements of each antenna element operating near 146 MHz would need to be accurate within 50 centimeters. Note that this result was gathered based on an eight element array. But if the position measurements are accurate to 50 centimeters, then the element positions can be offset from the ideal configuration by more than five meters when the MVDR technique is applied[38]. Note that five meters is not taken as a limiting upper bound for known offset as Miller et. al. conducted simulations up to 200% of the wavelength but no further and saw little to no reduction in performance up to 200%[38].

To make a meaningful impact with the data collected, the radar must be tuned so that it can successfully sound a significant portion of the ice sheets. From the Bedmap2 DEM of Antarctica, it is believed that some of the thickest ice sheets approach and possibly exceed five kilometers[17]. However, the mean value of ice sheet thickness slightly exceeds two kilometers. The ability to sound deeper than the mean thickness is highly desirable to capture large portions of the icesheets. Differing conditions of the ice sheets also plays a role in the ability to sound as the radar signal will attenuate at different rates. Signal attenuation of the radar pulse as it propagates through thick ice is important for quantifying the effectiveness of this radar mission. Attenuation through the ice sheet medium is affected by liquid water content, temperature, and other related factors[54]. It is expected that the system outlined in this chapter will not be able to sound the ice sheet margins due to higher surface temperatures, higher liquid water content, and thereby higher attenuation compared to thicker, colder ice that is farther inland. A conservative estimate of medium attenuation is recommended at this stage in the design. Other orbital radar sounding concepts reviewed in this document gave one-way ice sheet medium attenuation rates on the order of -9 dB/km[32] (e.g. -18 dB for 2 km thick ice). This estimate corresponds with detailed attenuation studies, like work done by Macgregor et al.[54], therefore it is considered a reasonable and conservative attenuation rate for the radar link budget presented in this chapter.

By combining all the considerations outlined in this section, a reasonable design of a nanosatellite constellation for radar ice depth sounding can be defined.

3.2 Orbit Selection

Selection of orbital parameters, at this stage in the design process, allows for an initial glimpse at the mission performance. The basis of the KRISP mission is to sound the largest ice sheets on Earth's surface. These ice sheets lie in the polar regions of both Northern and Southern hemispheres. To maximize sounding opportunities, the orbit must be highly inclined (also known as a polar orbit). With this mission focused on implementing nanosatellites, and future mission goals of replacing or upgrading portions of the constellation, it is desirable for the orbit to have a lower altitude, classified as LEO.

Presented in Table 3.1 are the driving orbital elements for the KRISP mission. The orbit selected is known as a Sun synchronous orbit, meaning that the orbital elements are calculated to maximize exposure to solar illumination.

Table 3.1: Initial Orbital Elements

Periapsis Altitude (km)	Eccentricity (~)	Inclination (deg)	Right Ascension (deg)	Argument of Per. (deg)	Period (min)
555.00	1.00E-03	97.61	90.00	0	90.50

Key orbital elements that clearly satisfy the sounding goals given are the inclination and the altitude of periapsis. Inclination of this orbit is near to 90 degrees indicating that the satellite will see most of Earth's latitude lines on both hemispheres, thus maximizing coverage of the ice sheets. The altitude at periapsis of 555 km indicates the constellation will be in LEO which allows for reasonable satellite lifetimes and future upgrades to the constellation. The eccentricity of 0.001 indicates that the orbit is fairly circular, meaning the altitude above Earth will be confined to a tight range.

Future iterations beyond this work could perform an optimization study to determine orbital parameters to optimize coverage. Based on preliminary analysis of the orbital parameters presented,

the current coverage encompasses nearly the entire Antarctic and Greenland ice sheets, given a long enough operation time. As such, changes to the orbital parameters are expected to have a limited effect to extend coverage. With the initial orbit defined, the radar payload can be determined and analyzed.

3.3 Radar Parameters

Based on the review of fielded radar systems and orbital radar concepts, the radar operating parameters are established. This section will discuss the key details for operating a VHF pulsed coherent radar which define: the sounding configuration (geometry) and operational parameters (e.g. frequency, power, and, bandwidth). Once defined, an analysis of the selected system can be done to calculate performance parameters. Note that the radar payload detailed in this section is heavily based on systems presented in Section 2.1. A fully designed radar system for orbital depth sounding is beyond the scope of this work and the details of which should be pursued by others. The design presented here serves as a realistic placeholder for a properly designed radar payload.

3.3.1 Geometry

Considering the operation of an orbital radar depth sounder, a critical decision is the radar sounding geometry or configuration. Radar geometry typically has two main configurations. The simplest is the monostatic case where a radar transmits a pulse and subsequently receives the pulse on the same platform, making the position of the transmitter and the receiver the same. If the transmitter and receiver positions are decoupled, this refers to the bistatic case. In a bistatic case, the radar transmits from one platform and the pulse is then received by a separate platform. The constellation designed for this mission is intended to utilize both sets of geometry as there will be a single satellite capable of both transmit and receive operations (monostatic) while all other satellites in the constellation can only receive (bistatic). An illustration of the constellation radar geometry is given in Figure 3.2.

From Figure 3.2, there is a monostatic geometry for a single lead satellite (in green and labeled

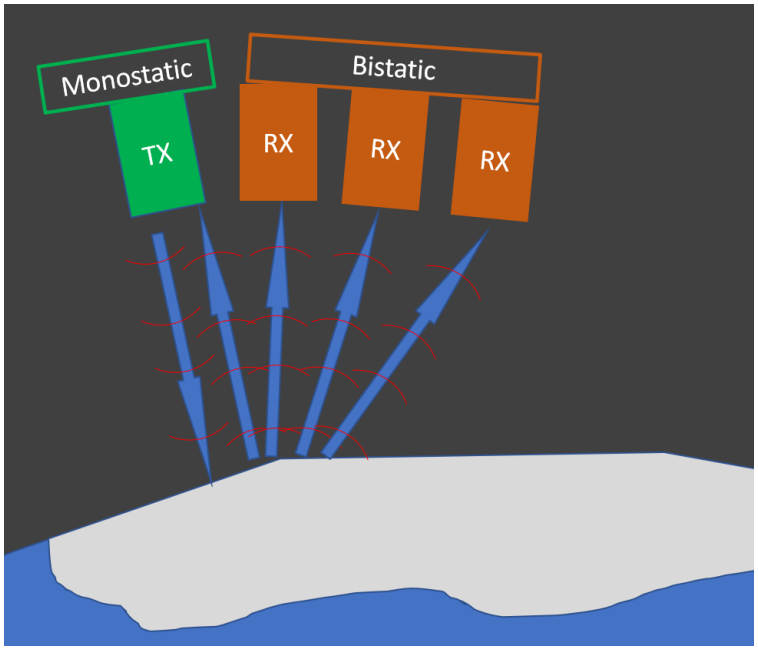

Figure 3.2: Radar Geometry

TX) which is designed for transmitting all of the radar pulses but is also capable of receiving. Note that although this satellite is capable of both transmitting (TX) and receiving (RX) it has only been labeled as TX for the sake of brevity. No other satellites generate a radar pulse, but rather serve as receive-only satellites. Therefore, the receive-only satellites (in orange and labeled RX) have to be treated as the bistatic case while the transmit satellite is treated as the monostatic case.

Following the definition of radar geometry, operational parameters of the constellation must be defined. Operation will focus on the transmit portion of the radar payload. Certain aspects of the receive operation will be noted and used to calculate system gains within the link budget.

3.3.2 Radar Operation

To best penetrate the ice and be able to detect echoes from the bedrock below, a particular set of operational parameters have to be defined. Note these values are based on the legacy radar systems discussed in Section 2.1 and do not represent an existing system currently under development, but rather represent goals for radar development. The TRL for the identified system is at or below a six (indicating system demonstration in a relevant environment) and as such may not currently be

flight ready; therefore margins must be present in the analysis.

The KRISP radar will use a pulsed Linear Frequency Modulated (LFM) operation mode. Pulsed radars have short intervals of transmitting, defined as the pulse duration, followed by long intervals of receiving, defined as the echo duration. The interval between consecutive pulses defines the Pulse Repetition Frequency (PRF). The PRF is calculated based on a number of factors, including pulse duration, range to the target, and the distance from the closest target (air-ice interface) and the farthest target (ice-bedrock interface), in the time domain.

Table 3.2 gives the expected operational parameters of the KRISP radar. Note these do not represent optimum values but rather a starting place for mission analysis.

Table 3.2: Initial Radar Parameters

Transmit Power (W)	Frequency (MHz)	Bandwidth (MHz)	Sample Rate (MHz)	PRF (kHz)	Pulse Dur. (μs)	Echo Dur. (μs)
100	146	4	50	10.1	21.0	77.7

Transmit power of this radar was selected based on the radar system comparisons given in Section 2.1. This value has been evaluated with satellite designs to ensure 100W of transmit power is achievable and sustainable.

It is known from the background sections that having a VHF system is highly desirable to reduce clutter sources and increase SNR. After investigating nanosatellite antenna systems in this band, operating at a center frequency of 146 MHz is desirable with an achievable bandwidth of roughly 20 MHz. However, the previous review of FCC allocated frequencies showed that only a four MHz bandwidth could be easily obtained. It is possible that a nine MHz band exists for the purpose of this mission but four MHz was selected for this analysis. The antenna is expected to be a half-wave length dipole, therefore the single aperture length is approximately one meter. Each satellite in the constellation will only have a single antenna element for radar operation.

Based on the orbital parameters selected, the Earth's surface is assumed to be an average of 555 km from the radar. As such, signal sampling will begin at 552.5 km and end at 557.5 km totaling five kilometers of possible depth sounding. For reference, Bedmap2 of Antarctica indicates the

deepest ice sheets are just over 2.8 kilometers below sea level[17]. These deepest ice sheets would be just out of reach of the selected sampling range. Defining the sampling distances bounds the required PRF and the number of pulses in the air[55]. The PRF and the number of pulses can then back out the unambiguous range and echo duration. Echo duration refers to the time between consecutive pulses where the radar is receiving the radar signal from a single known pulse.

The selected sample rate is based on experience with radar systems. It is also known that the sampling rate must be at least twice the bandwidth to satisfy Nyquist conditions[55].

With these basic operating parameters set for the radar system, an initial analysis can be done to evaluate expected performance.

3.3.3 Initial Radar Analysis

Radar analysis focuses on the achievable performance of the selected operational parameters given in the previous section. In this case, "performance" is defined as the expected probability of ice bed detection which is dependent on SNR, and how well a target can be resolved.

All of these performance metrics are highly dependent on the radar hardware. As no internal hardware will be selected for this project, these results are representative; however, current radar hardware capabilities were kept in mind when determining the necessary performance.

Radar analysis begins by estimating the expected receive power, noise power, and the resulting Signal-to-Noise Ratio (SNR). Equation 3.1 defines the noise power relationship. In this equation, k is the Boltzmann constant, T_0 is the absolute temperature in Kelvin, B is the receiver bandwidth in Hz, and F is the receiver noise figure which is unitless. All constants can be found in Table B.1 of Appendix B. T_0 is selected as 290 K as this is standard practice. An assumed noise figure of 2.5[55] was also selected. The noise power relation is based solely on the receiver bandwidth, thus the noise power will not change significantly as the mission progresses. Noise power for the selected radar parameters is calculated to be -133 dB.

$$P_N = k\ T_0\ B\ F \tag{3.1}$$

The estimated receive power is calculated by using the radar range equation, given in Equation 3.2. Inputs to this equation are transmit power P_t (100 W), transmit antenna gain G_t, receive antenna gain G_r, speed of light c, frequency f (146 MHz), and range to the target R (555 km). Antenna gain is assumed to be 2.2 dBi, which is the gain of a standard half-wave dipole which is present on all constellation satellites. The radar range equation is also dependent on radar cross section σ of the target which can be evaluated using Equation 3.3. For a square flat plate with a length r of 500 meters, σ is calculated as 2×10^{11} m^2. Note that this Thus the received power for the given radar parameters is calculated as -119 dB.

$$P_R = \frac{P_t \, G_t \, G_r \, c^2 \, \sigma}{(4 \, \pi)^3 \;\; f^2 \, R^4} \tag{3.2}$$

$$\sigma = \frac{4 \, \pi \, r^4 \;\; f^2}{c^2} \tag{3.3}$$

By breaking out the gains and losses from the radar range equation and other contributions from ice depth sounding, a link budget is assembled and shown in Table 3.3. By solely considering the receive power and noise power equations given above, the resulting SNR is 14.4 dB which is encouraging. However, this does not account for all signal losses or processing gains. The first source of loss, is the -3 dB estimate of system losses. This is a common estimate for link budgets and provides a conservative estimate of SNR[32]. Another major source of signal losses is the medium attenuation through the thick ice sheets. For thick, dry ice sheets, the one-way attenuation is on the order of -9 dB/km[32] which results in -54 dB of attenuation for 3 kilometer thick ice (which is greater than the mean ice sheet thickness[54]). This reduces the SNR to -42.6 dB. But the use of advanced radar techniques such as coherent integration, pulse compression, and array processing can increase the SNR to acceptable levels (i.e. above 0 dB).

Coherent integration, also known as presumming, is the technique of summing or averaging multiple sequential signals together to improve the SNR. Equation 3.4 shows the simple relationship of how coherent integration can increase the SNR of the received radar signal, where N_{coh} is the

Table 3.3: KRISP Link Budget

Parameter	Equation	Units	Value
Spreading Loss	R^{-4}	dBm^{-4}	-229.93
Wavelength Effect	$\frac{c^2}{(4\,\pi)^3\ f^2}$	dBm^2	-26.73
Peak Power	P_t	dBW	20.00
Transmit Gain	G_t	dB	2.20
Receive Gain	G_r	dB	2.20
RCS	σ	dBm^2	112.70
System Losses		dB	-3.00
Medium Attenuation	-9 dB/km One-Way[32]	dB	-54.00
Coherent Integration	Equation 3.4	dB	16.43
Pulse Compression	Equation 3.5	dB	19.24
Advanced Processing	SAR=5dB, MVDR=5dB	dB	10.00
Total Signal Power	Sum of Above	dB	-130.88
Total Noise Power	Equation 3.1	dB	-133.98
SNR		dB	3.10

number of signals that are coherently integrated[55]. For 44 coherent integrations, a gain of 16.4 dB will increase SNR to -26.1 dB. But there are other operating techniques that can increase the SNR further such as pulse compression.

$$SNR = SNR\ N_{coh} \tag{3.4}$$

Pulse compression is another operating technique that limits transmit power but increases pulse duration with the added benefit of increasing SNR. Shown in Equation 3.5, is the contribution of pulse compression by applying the time-bandwidth product where τ is the pulse duration[55]. With a pulse duration of 21 microseconds (based on MCoRDS), the gain from pulse compression is 22.8 dB which increases our SNR to -6.9 dB. At this point, there are limited operating gains that can increase SNR but post processing techniques (e.g. SAR, MVDR, etc.) can further increase the SNR.

$$SNR = SNR\ \tau\ B \tag{3.5}$$

Approximating the gains from advanced signal processing is difficult as their main function is to increase SNR as much as possible and as such there is no explicit relationship between radar operating parameters and SNR gains for advanced processing techniques. However, work done by this author (specifically with MVDR) has shown that if the phased array has sufficient position knowledge (less than 25% of the wavelength), then the SNR can be increased by as much as 20 dB[38]. This 20 dB gain only considers the contribution from MVDR and not other techniques like SAR which would also considerably increase SNR. Therefore, it is expected that advanced signal processing techniques could increase SNR by 20 dB (± 10 dB for conservative estimates). Even at the lowest contribution from these techniques (10 dB), the resulting SNR is 3 dB which is sufficient for radar sounding. As long as the SNR is above zero, it is expected that a target can be resolved. Note that this link budget is the same for each satellite in the constellation as each will have the same receive hardware. The last relevant calculation is to determine the resolution of these measurements.

Range resolution, ΔR, indicates the minimum distance between two targets that can be separately resolved. Equation 3.6 defines the range resolution relationship for an LFM radar system[55]. The evaluated resolution of 37.5 meters is coarser than most VHF systems, but is still in-line with other legacy airborne systems. Any increase to the available sounding bandwidth would improve this resolution (a bandwidth of 9 MHz would have a resolution of 16.6 meters).

$$\Delta R = \frac{c}{2\ B} \tag{3.6}$$

Assumptions made in this analysis are believed to be reasonable as they are based on hardware of legacy systems and high TRL hardware. It is expected that hardware required to execute this mission could be achieved within five years.

3.4 Satellite Parameters

With the radar payload architecture outlined in the previous section, the satellite architecture is defined. Details of this section cover satellite design requirements, satellite concept of operations (ConOps), and satellite hardware.

The KRISP mission focuses on a constellation of satellites for radar ice depth sounding. Each satellite within the constellation will act as radar receive channel and a single satellite will also act as the radar transmitter. The total number of satellites within the constellation is expected to range between four to eight satellites in total. Finding the optimum number requires a significant amount of follow-on work which is beyond the scope of this project. As such, a reasonable assumption is that the constellation will hold eight satellites. This number of satellites will be relevant later on in the analysis.

As outlined, the payload will have two unique hardware sets for transmit and receive operations. One single satellite in the constellation will have both sets of hardware so that is capable of transmitting and receiving. This satellite will have the designation of TX going forward. The receive hardware will appear on all other satellites within the constellation. Satellites with only receive hardware are designated as RX.

To begin the satellite design process a set of design requirements must be established. After which, a concept of operations is established to define the key operational modes needed to maintain control of the satellite on orbit while executing the ice sounding mission. Designs for the RX and TX satellites are then presented by defining the required hardware and the hardware configuration within each satellite. Lastly, the satellite designs are analyzed to verify the proposed designs.

3.4.1 Satellite Design Requirements

Each satellite within the constellation must meet design requirements driven by the payload, satellite design practices, or mission objectives. The payload operation has been described in Subsection 3.3.2 and several requirements have been noted. Satellite design practices come from

technical manuals, such as CubeSat 101 provided by NASA[56] or the Cubesat Design Specification (CDS) from California Polytechnic University[57], from well-recognized references such as Space Mission Analysis and Design (SMAD)[58] or Elements of Spacecraft Design[59], and from personal experience with spacecraft design, such as designing the KUbeSat1 mission.

An initial set of mission requirements is given in Table 3.4. Note that this is not an extensive list but rather marks key design criteria that must be met in this early stage of development. As the design approaches completion, more necessary requirements will have to be considered and met to accomplish the mission.

Table 3.4: Mission Requirements

#	Description	Based on
1	All hardware must mount internal or external to satellite while maintaining outer mold line	CDS[57]
2	Satellite mass must not exceed limits of 6,000 grams for 3U and 12,000 grams for 6U frames	CDS[57]
3	Must fit into a standard dispenser (such as a P-POD)	CubeSat 101[56]
4	Hardware must have a TRL higher than 7 (Except payload)	Derived
5	All hardware must have compatible connections for command and power	Derived
6	Must be able to telemeter data to ground stations	Derived
7	Must be able to maintain control of the satellite through all phases of operation	Derived
8	Must be able to command all flight hardware	Derived
9	Hardware must have common power and data/command connections	Derived
10	Must be able to point the satellite with 0.01 degrees of accuracy	Payload
11	Must be able to measure position with an accuracy of ± 0.5 meters	Payload

Cubesat design practices focus on repeatable frameworks that limit development and integration time. The first requirement defines that all of the hardware must fit within a satellite or be mounted externally without effecting the outer mold line. This directly ties to the third requirement of fitting in a standard dispenser. If the satellites cannot fit in a common dispenser, launch costs and integration time will grow rapidly. Similarly, if the satellites have too much mass, there will be project overruns. For small satellite design, project schedule and budget are often design drivers. Therefore further requirements were derived to achieve that goal, as denoted by the "Derived" entries in Table 3.4.

Requiring that all hardware is above a TRL of seven, drives the use of COTS hardware. COTS hardware works off standard practices across the industry, to include module footprint and connection types. Most hardware modules connect through a PC104 header which holds all the necessary command and power connections across the satellite. Maintaining control of the satellite is based on having the correct subsystem configuration for the Attitude Determination and Control System (ADCS) and properly allocating power. The control and allocation comes from satellite commands which are driven by the Command, Data, and Handling (CD&H) subsystem. All derived requirements come from the objectives of simplifying design and reducing mission risks. The last requirements focus on achieving the goals of the payload, as denoted by the "Payload" entries in Table 3.4.

Requirements based on the payload (10 and 11) are set to improve the ability to sound ice sheets. As has been shown in the background sections, positional knowledge is crucial for successful post-processing of radar data.

With the mission requirements specified, satellite Concept of Operations (ConOps) can be developed. The details of the ConOps is discussed in the next section.

3.4.2 ConOps

Over the lifetime of a satellite, there are certain operational modes that must be entered depending on external stimuli or internal state of the satellite. Each operational mode indicates which mission tasks can be performed based on a given state. Tasks are discussed with respect to each operational mode below but several examples are: payload operation, telemetering data, and orienting the satellite. Note that these mission tasks are present in different operational modes but represent the same satellite function unless specified otherwise.

This section details the expected operational modes of the satellites within the KRISP constellation. These modes have a hierarchy, or priority, dictating which mode overrides another. This priority is critical as the satellite state information could match multiple operational modes but the priority helps maintain control.

Table 3.5 gives the expected operational modes for the KRISP mission. Note a lower priority number is more critical. Also, an estimation of percentage used per orbit is given for each mode. These percentages serve as a reference for how frequently a mode may be used over the course of the mission.

Table 3.5: ConOps Breakdown

Mode	Main Objective	Priority	% of Orbit
Detumble	Gain control after launch vehicle jettison	0	0.01
Nominal	Operate payload	5	60
Low Power	Charge batteries	2	35
Data Purge	Telemeter Data	3	4.9
Momentum Dump	Release built-up momentum	1	0.07
Critical	Maintain control and await instruction	0	0.02

Starting with jettison from the launch vehicle, the first step is to gain control of the satellite. Control generally means that subsystems can be properly commanded and the satellite is functional. This mode is referred to as Detumble as the satellite will have some amount of spin after being ejected from the dispenser while on orbit. This spin must be corrected so the spacecraft stops tumbling and can enter nominal operation. It is expected that this mode will only be used once but it could be used in dire circumstances to regain control of the satellite. The only mission tasks available in this mode are orienting the satellite and satellite telemetry.

Most of the time, KRISP satellites will be in a Nominal operational mode. This is the only mode in which the payload operation task is available. The payload will operate over defined geographic windows and collect sounding data. All mission tasks are available in this mode, to include: payload operations, telemetry, and satellite orientation.

After a period of time in Nominal mode, the satellite will deplete its power storage. In this case, Low Power mode is entered. This mode specifically orients the spacecraft to optimize solar power generation. As noted, the payload will not be used in this mode so that power can accumulate quicker. Telemetry of data is also a key part of Low Power mode. At this time, all mission tasks are available to this mode except for the payload operation task.

In certain circumstances, the onboard data storage limit will be reached. If this occurs, Data

Purge mode is entered to prioritize data telemetry and reducing onboard data. This mode is very similar to Low Power mode but has different triggering conditions. Again, all mission tasks are available except for payload operations.

It is required that the ADCS subsystem maintain control through all phases of flight. In doing so, it will saturate the reaction wheels, which are its main orienting device. In the case that reaction wheels are near saturation, a Momentum Dump mode is entered where the magnetorquers are enabled to cancel the despinning reaction wheels. This operational mode is expected to be used after long periods of time, on the order of months. The only mission task executed in this mode is orienting the satellite.

As a last resort, a Critical mode is available to the satellites. Critical mode would only be entered if some part of the satellite no longer operated as expected. This could be a wide range of things, but it would be identified by the CD&H subsystem. In this worse case scenario, the satellite enters a mode where only the vital tasks are done and the satellite awaits a connection with our groundstations for the next steps. It is not expected that this mode will ever be entered, but it must be listed as a precaution.

With operational details set, the initial satellite design can be defined.

3.4.3 Satellite Design

Design of any satellite is dependent on the mission payload, requirements, and ConOps. The ConOps is also dependent on the satellite and is included as part of the design iteration loop.

Presented in this section are two unique satellite designs to serve the KRISP mission. As previously mentioned, one satellite design (TX) is capable of operating both transmit and receive operations, the other design (RX) is only capable of receive operation.

Notional block diagrams for the RX and TX satellites are illustrated in Figure 3.3a and Figure 3.3b, respectively.

These diagrams serve as a guide for the interconnections between subsystems of the satellite. Each satellite has six basic subsystems that will be discussed in detail: Structures, Communications

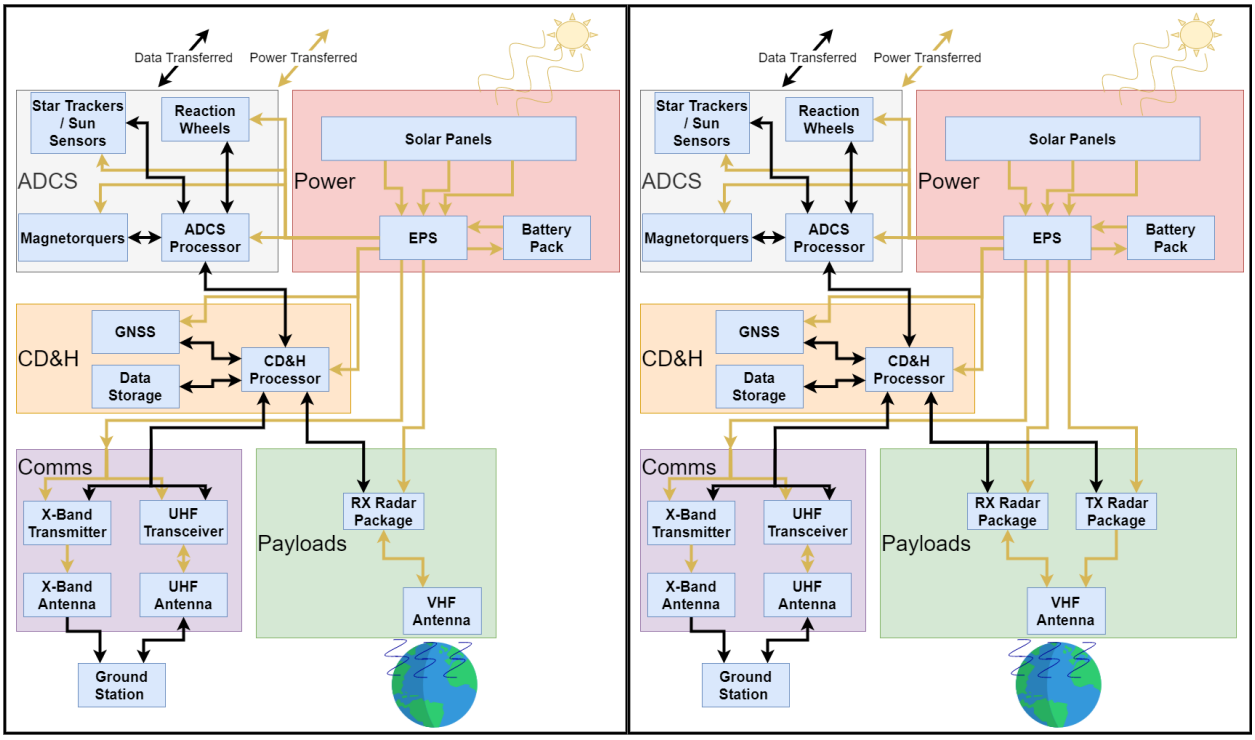

(a) RX Satellite (b) TX Satellite

Figure 3.3: Satellite Block Diagrams

(Comms), Power, Attitude Determination and Control System (ADCS), Command, Data, and Handling (CD&H), and Payloads. All subsystems, except Structures, are represented in these graphics. Note that the RX satellites will be housed in a 3U Cubesat frame while the TX satellite will be housed in a 6U frame.

Inspecting the two block diagrams, they are markedly similar in this initial design phase. This is intentional as both satellite designs must fit all of the same design requirements and similar hardware reduces development time. The main difference between the two diagrams is the presence of the TX Radar Package in the TX satellite.

Keeping similarity in the satellite designs limits complexity. Also, by selecting COTS modules from the same companies can reduce complexity and subsequent development time. Efforts are taken to focus on as few hardware providers as possible to maintain compatibility and special care is taken to ensure all modules can properly connect together. Note that most modules will be connected through PC104 stack header, common practice for nanosatellites[56], and other unique

connections will be noted.

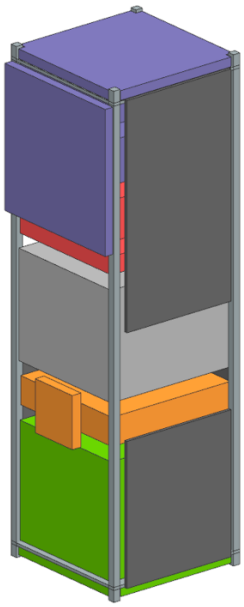

(a) RX Satellite CAD

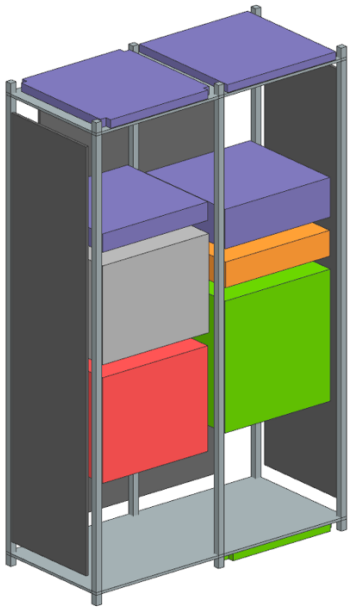

(b) TX Satellite CAD

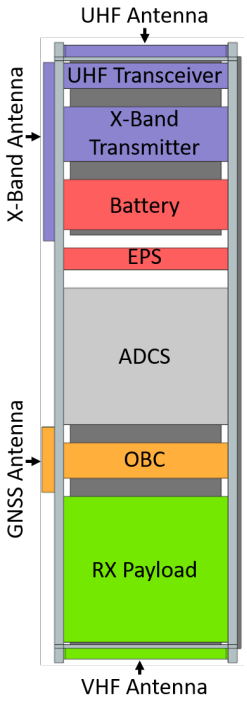

(c) RX Overview

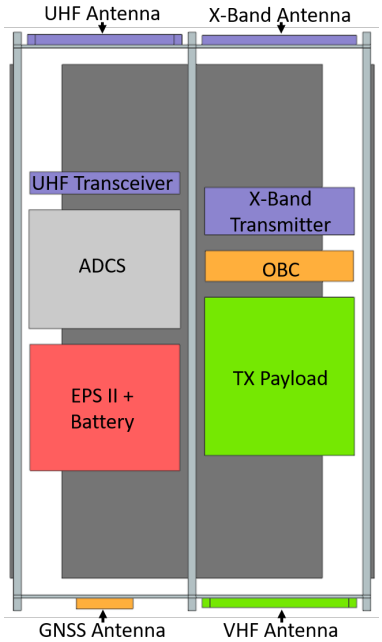

(d) TX Overview

Figure 3.4: Satellite CAD and Overview

A CAD model was developed for both the RX and TX satellites, as shown in Figure 3.4, to help visualize the satellite layout and subsystem sizes. An isometric view of the RX and TX satellites

are given in Figure 3.4a and Figure 3.4b, respectively. Also illustrated is a side view to indicate the hardware present in the RX and TX designs which are shown in Figure 3.4c and Figure 3.4d, respectively.

Note that the colors in Figure 3.4 match the subsystem colors used in the notional block diagrams presented in Figure 3.3, where payload hardware is green, communications hardware is purple, power hardware is red, ADCS hardware is grey, and CD&H hardware is orange. The solar panels are also included in these CAD models and are indicated by the thin dark blocks on the sides of the satellites.

The following sections will discuss the selected hardware in more detail for each of the subsystems. All hardware selected for the RX and TX satellites are given in Appendix A in Table A.1 and Table A.2, respectively. These tables contain cost details, as available, along with the size, mass, and power of each selected module. Further relevant details are given in the following subsections, starting with the most variable piece of hardware: the payload.

3.4.3.1 Payloads

Payload hardware for the KRISP mission is broken into two categories: receive-only (RX), and transmit+receive (TX). As previously mentioned, the two unique satellite designs are based on the presence of either set of hardware. In the constellation, a single TX satellite will be able to transmit and receive while an undetermined number of RX satellites will only be able to receive. Operational details of the radar have already been discussed in Section 3.3. The purpose of this section is to define the size, mass, and power properties of these payloads. A list of these details for the payloads subsystem are given in Table 3.6.

Table 3.6: Payload Hardware

Name	Manufacturer	Size [XYZ] (mm)	Mass (g)	Max Power (W)	Data Rate (kb/s)	On Sat.
RX Radar	CReSIS	[89, 95, 80]	1500	15	43000	RX
TX Radar	CReSIS	[89, 95, 100]	1800	115	44000	TX
VHF Antenna	ISISpace[60]	[98, 98, 6]	89	N/A	N/A	RX, TX

The RX radar and TX radar module properties are based on a nonexistent set of hardware, therefore some conservative approximations are needed. As a reference, an HF Micro radar system developed by CReSIS which is to be flown on a Vapor UAS has a measured volume of 740000 mm^3 and a mass of 900 grams. For comparison, the RX radar module has a volume of 676000 mm^3, just less than 1U of volume, and the TX radar module has a volume of 846000 mm^3. Note that the RX radar module has less volume compared to the HF Micro because the HF Micro can both transmit and receive radar signals, much like the larger TX radar module. These volumes were selected for the radar modules to serve as the expected maximum size for both sets of hardware. The mass of the modules is much greater than the HF Micro so as to account for more robust space hardware. Mass selected for these modules is also expected to be a maximum for the flight modules.

Power of the TX module is based on the radar transmit power defined in previous sections with an arbitrary amount of additional power to account for receive operations. Listed is the maximum power of this module but with a pulse duration of 21 microseconds (max power) and an echo duration of 77.7 microseconds (RX power), the average power during radar operations would be 36.3 W. This power result comes from the application of the roughly 20% duty cycle of the transmit operation multiplied by the 100 W transmit power and then added to the 15 W power of the receive operation which has an assumed 100% duty cycle. Power of the RX module only accounts for receive operations. These power values serve as maximums for the expected power of flight hardware. Data rate for the RX module is based on preliminary radar analysis. The TX module has a slightly increased data rate value to account for any data collected for transmit operations. Both data rates serve as the expected maximum but these are highly variable and as such the satellite design should be robust to these changes. As noted in the "On Sat." column, the TX module is only present on the TX satellite and the RX module is only present on RX satellites.

As the RX and TX radar hardware is not yet realized, the values presented for size, mass, and power can fluctuate, especially at the early design stages. The values assumed for this mission provide a reasonable goal for radar designers but also indicate a significant engineering challenge in terms of satellite configuration and design.

Apart from the radar modules internal to the satellite, each satellite design also requires a VHF antenna to either transmit or receive the radar signal. As mentioned in the requirements section, using COTS hardware ensures high TRL and limits development time. For these reasons, a customizable COTS antenna from ISISpace[60] is selected as the radar antenna. An image of the module is provided in Figure 3.5

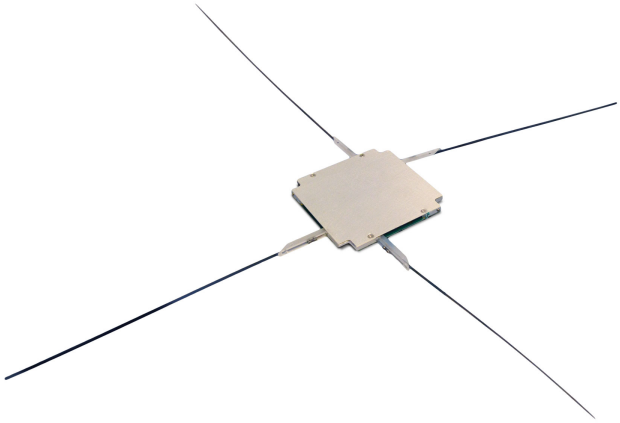

Figure 3.5: ISISpace VHF Antenna Module[60]

Configurable frequencies for this module are between 100 and 500 MHz[60]. Although it may be possible to configure two dipole elements with one antenna module, it is only considered to be a single half-wave dipole element. This antenna module will mount externally on the frame and deploy a dipole designed for the VHF band. This antenna module will be present on both RX and TX satellites.

Connections between the radar payload and the VHF antenna will consist of a common RF connection, such as SMA or MMCMX. Payloads will connect to the power subsystem through the proper voltage bus that will be dependent on the payload development. A USB-C connection from the payload to the CD&H is expected in order to transfer data and command the payload operations. Both the power and the CD&H connections are unknown at this point, but the selected modules for these subsystems have a wide variety of connection types which will certainly satisfy the payload needs.

With the payload hardware defined for both satellite designs, a structure must be selected to house all of the flight hardware.

3.4.3.2 Structure

Structure subsystems for nanosatellites typically cover the frame, mounting, and wiring hardware. As this design is in early stages, mounting and wiring hardware are outside of the scope of this initial architecture. Common practice is to approximate mounting and wiring mass based on the satellite's total mass. The satellites' frames must be selected at this early stage for both the RX and TX designs. The frames selected are detailed in Table 3.7.

Table 3.7: Structures Hardware

Name	Manufacturer	Size [XYZ] (mm)	Mass (g)	On Sat.
6U Frame	Endurosat[47]	[100, 226.3, 366]	850	TX
3U Frame	Endurosat[47]	[100, 100, 340.5]	290	RX

For the KRISP mission, there is a single TX satellite which will have a 6U Cubesat Structure from Endurosat[47]. The 6U frame was selected simply for the size. The TX satellite requires more internal volume (~2U of volume) for the radar payloads and the available volume of a 6U frame gives a wide margin for the payload as development continues. 6U satellite frames also offer a larger solar collection surface which is vital for the power hungry TX payload.

The RX satellites for this mission will utilize 3U Cubesat Structures from Endurosat[47]. RX satellites are the best place to seek optimization in the KRISP constellation as a larger number will be deployed. As the number increases, the launch vehicle opportunities become more sparse and more expensive. For this reason, the RX satellites have been constrained to a 3U structure.

Modules internal to the satellite will be mounted along a rail system. There is a rail at each corner of the 3U structure for mounting a single stack of satellite modules. The 6U structure is more configurable but it is assumed to have two rail sets that mimic the 3U rails, therefore two stacks of satellite modules can be mounted in the 6U. A single stack has a height of approximately 320 mm[47], meaning that modules utilizing the rail systems must not stack higher than 320mm.

Analysis will show that the structures selected have more than enough internal volume to safely house all of the components along the described rail systems. The external mounts of the satellites are also capable of fixing the numerous antennas on each craft, for payloads and communications purposes.

3.4.3.3 Communications

Operating a satellite requires communications with ground stations. Space communications revolve around data transmitted from the satellite and commands received from the ground. With such high data loads on every satellite in the constellation, different radio bands will have to be utilized. The components needed for the communications subsystem are listed in Table 3.8.

Table 3.8: Communications Hardware

Name	Manufacturer	Size [XYZ] (mm)	Mass (g)	Power (W)	Data Rate (kb/s)	On Sat.	Function
UHF Antenna	Endurosat[47]	[98, 98, 6.5]	85	N/A	N/A	RX, TX	General Comms
UHF Transceiver	Endurosat[47]	[89, 95, 14]	90	1.4	15	RX, TX	General Comms
X-Band Antenna	Endurosat[47]	[98, 98, 6]	89	N/A	N/A	RX, TX	Payload Data
X-Band Transceiver	Endurosat[47]	[89, 95, 30]	270	2	150000	RX, TX	Payload Data

X-Band communications, or other high data rate alternatives, are vital for a mission of this type. The receive hardware for each satellite has a data collection rate of 43 MB per second. S-Band transmission has a data rate of roughly 20 MB per second and X-Band has 150 MB per second. Clearly X-Band would be a preferred selection when the number of ground stations are limited. Thankfully ground stations at the University of Kansas are working towards both S-Band and X-Band reception.

Operations at the UHF band will be focused on receiving commands from ground stations and providing redundancy for the X-Band setup. Both bands of transmission require an antenna, which is mounted externally, and a radio module, internal, which acts as the transmitter and/or receiver.

For this mission, the X-Band will only be utilized for payload data transmission. Adding X-Band receive capabilities is expensive and unnecessary.

Both the UHF transceiver and the X-Band transmitter will be stacked internal to the satellite. The main internal connections are through the PC104 stack which provides power and command of modules in the satellite. Both UHF and X-Band antennas will connect to the respective radio module through an MMCMX connection.

The UHF antenna will be mounted at one end of the satellite, opposite to the VHF antenna for the payload. The X-Band antenna has more flexible mounting possibilities as there are several antenna modules available for purchase through Endurosat[47]. Endurosat has a single X-Band patch antenna, a 2x2 patch antenna array, and a 4x4 antenna array. These three modules are shown in Figure 3.6 to help visualize the size differences.

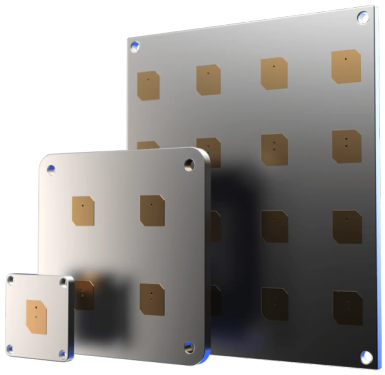

Figure 3.6: Endurosat X-Band Antenna Modules[47]

The size selected for this design is the 4x4 patch antenna array which has the same dimensions as the UHF antenna from Endurosat, based on available images. Note that it is currently understood that any of these antennas would work for this mission but the largest was selected to consider the largest size and mass. For the TX satellite, the X-Band antenna will mount adjacent to the UHF antenna. The RX satellite will have the X-Band antenna mounted on the side with no solar panels. Note that the mounting solution for the RX satellite still satisfies the mission requirements given in Table 3.4.

Both the payloads and communications subsystems make up almost 80 percent of the power draw for a normal satellite. Care must be taken to ensure the craft can generate and store enough power.

3.4.3.4 Power

Key to the life of any satellite is the power subsystem. Power on the satellite is generated by solar panels, stored in the batteries, and distributed by an Electrical Power System (EPS). These selected components for the KRISP mission are shown in Table 3.9.

Table 3.9: Power Hardware

Name	Manufacturer	Size [XYZ] (mm)	Mass (g)	On Sat.
Starbuck-Nano EPS	Clyde Space[61]	[90, 96, 12.4]	88	RX
40Whr CubeSat Battery	Clyde Space[61]	[90, 96, 27.4]	351	RX
EPS II + 80Whr Battery	Endurosat[47]	[89, 95, 80]	1280	TX
1U Solar Panel	Endurosat[47]	[82.6, 98, 2.2]	44	RX
1.5U Solar Panel	Endurosat[47]	[82.6, 154.7, 2.2]	65	RX
3U Solar Panel	Endurosat[47]	[82.6, 325, 2.2]	127	RX, TX
6U Solar Panel	Endurosat[47]	[165, 325, 2.2]	254	TX

External to each satellite will be a set of solar panels. For the TX satellite, there will be one main 6U solar panel which can achieve 19.2W of power generation in LEO[47] and two 3U solar panels on the 3U sides which can individually generate 8.4W in LEO[47]. The RX satellite will have a single 3U solar panel for the main power generation and two other satellite sides will have a 1U and 1.5U solar panel, totaling five solar panels. These solar panels will connect directly to the respective EPS through a unique solar panel connection. Note that Endurosat and Clyde Space power hardware are compatible.

The RX satellite has an EPS and battery set from Clyde Space[61] while the TX satellite has an EPS and battery combo module from Endurosat[47]. Although the Endurosat module provides 84Whr of battery storage, this is too much for the RX satellite and the module is not configurable for less storage. Therefore an alternative module set from Clyde Space was selected which provides

40Whr of storage and the same EPS capabilities. Note the ideal depth of discharge of these modules will differ between manufacturers, but the EPS is capable of regulating the battery state as necessary.

The size of Clyde Space modules are available on the webpage but the Endurosat EPS+Battery Pack does not have a publicly available size. Similar to the payload modules, the size for the EPS+Battery Pack is assumed to be just less of 1U. This estimate is informed by available photos and size comparisons of similar modules.

Connections in the TX satellite are the common PC104 stack for the EPS+Battery Pack, which will have 3V, 5V, and one configurable power rail. The RX satellite will also utilize the PC104 stack for connection of the EPS to the 40Whr battery and the other satellite modules with the same available power rails.

Unique to the battery modules of each satellite design, are built-in heaters which help maintain the thermal state of the spacecraft. Detailed thermal analysis is a part of the future steps of this project, but the heaters will act independent of the satellite ConOps. These heaters automatically turn on at certain temperature thresholds, typically during eclipse when no solar radiation is impacting the satellite. Both battery packs are equipped with one Watt heaters.

Power is maintained and distributed to each of the other subsystems on the satellite. To ensure the best power generation opportunities, the satellite must be able to point and orient itself on-orbit. This attitude control is maintained and measured by the ADCS subsystem.

3.4.3.5 ADCS

Maintaining the orientation of the spacecraft is vital for the different pointing scenarios of the KRISP mission. The satellite must be able to point during radar operations to optimize VHF antenna performance and similarly must be able to point during telemetry opportunities. The main pointing capability will be from a set of reactions wheels in the ADCS. These reactions can saturate and require momentum dumping operations to maintain usability. The momentum dump operations can be canceled out by a set of magnetorquers.

The ADCS subsystem also measures the orientation of the satellite. This is done with several

sensors with varying levels of accuracy. The highest accuracy measurements are made with star-trackers. Lower accuracy measurements are made by sun sensors, Earth-horizon sensors, and Micro Electro Mechanical System (MEMS) gyroscopes.

All of the above mentioned submodules are included in the turn-key ADCS solution provided by CubeSpace[62]. The details are listed in Table 3.10

Table 3.10: ADCS Hardware

Name	Manufacturer	Size [XYZ] (mm)	Mass (g)	Power (W)	On Sat.
ADCS 3-Axis	CubeSpace[62]	[90, 96, 75]	554	2.3	RX, TX

The all-in-one ADCS solution selected is capable of pointing the satellite the required 0.01 degrees and measuring the orientation with that accuracy. Parts of the ADCS module will be mounted separate of the PC104 stack but still internal to the satellite, to include the star trackers and possibly the reaction wheels. This modular subsystem will be used on both the RX and TX satellites.

With all the hardware selected to achieve the given mission requirements, the remaining CD&H system will act as central command and conduct operations of the satellite on-orbit.

3.4.3.6 CD&H

All satellite operations are directed by the CD&H subsystem. CD&H systems handle the commands for every subsystem on the craft, store payload data ready for telemetry, and monitors the satellite to execute the ConOps. The CD&H subsystem requires an On Board Computer (OBC), a Global Navigation Satellite System (GNSS) transceiver, and an external GNSS antenna. Note that use of GNSS architecture is equivalent but separate to Global Positioning System (GPS).The hardware selected for this subsystem is detailed in Table 3.11

The Endurosat OBC module will serve the largest role for the CD&H subsystem. Data stored in the OBC can be up to 32GB, satisfying the data storage requirement. The GNSS receiver is actually mounted internal to the OBC. As such, it does not increase the overall OBC size but does

Table 3.11: CD&H Hardware

Name	Manufacturer	Size [XYZ] (mm)	Mass (g)	Power (W)	On Sat.
OBC	Endurosat[47]	[89, 94, 19.5]	130	2.3	RX, TX
GNSS Receiver	Novatel[63]	[46, 71, 11]	31	1.8	RX, TX
GNSS Antenna	Taoglas[64]	[35, 35, 6.9]	20	N/A	RX, TX

increase mass to a total of 150 grams. The Novatel GNSS receiver is capable of measuring satellite position to within 2.5 centimeters (with additional subscription costs) or within 40 centimeters with post processing such as differential GPS[63]. The accuracy satisfies the requirement to measure position within 50 centimeters.

The OBC module will be mounted internal to the spacecraft along the PC104 stack. Connection between the GNSS receiver and antenna is covered by the coaxial cable to IPEX MHF1 from the antenna and attached to the OBC. The GNSS antenna has flexible mounting options due to its small size. The RX satellite will have the GNSS antenna on the same side as the X-Band antenna while the TX satellite will have the the GNSS antenna mounted next to the VHF antenna of the payload.

This completes the hardware selected for the KRISP mission. As mentioned, all hardware are compatible through the PC104 stack or other connections as detailed above. All of the hardware is able to mount either internal or external of the structure without affecting the outer mold line. These requirements are met based on the initial analysis of the spacecraft designs, detailed in the following section.

3.4.4 Initial Satellite Analysis

With satellite hardware selected, an analysis is done to confirm that these selections meet the given requirements. Analysis in this section includes: confirming ample internal volume for all hardware, estimating total mass, estimating total cost, and estimating power draw by subsystem.

Using the tables given in Appendix A, estimates of the maximum power draw, mass, cost, and stack height of each subsystem are listed below in Table 3.12 for both the RX and TX satellite designs. Note that stack height assumes the modules are oriented so that the X and Y sizes match the

rail system of either structure. As such the stack height represents the total Z size of the subsystem stack internal to the satellite. Recall, that the maximum total stack height is 320 mm for the 3U structure (RX) and 640 mm for the 6U structure (TX).

Table 3.12: Satellite Analysis

Subsystem	Cost ($)	Mass (g)	Max Power (W)	Stack Height (mm)
TX Satellite				
Payload	10000	1889	115.0	100.0
Structure	6400	850.0	N/A	N/A
Comms	41300	498.0	7.4	44.0
Power	59100	1788	1.0	80.0
ADCS	37400	554.0	5.6	75.0
CD&H	6000	161.0	2.6	19.5
Total	160200	5740		318.5
RX Satellite				
Payload	10000	1589	15.0	80.0
Structure	3300	290.0	N/A	N/A
Comms	41300	448.0	7.4	44.0
Power	25500	784.0	1.0	39.8
ADCS	37400	554.0	5.6	75.0
CD&H	6000	161.0	2.6	19.5
Total	123500	3826		258.3

Total cost of a single TX satellite is approximately $160,200 in hardware costs and the total cost of a single RX satellite is approximately $123,500. Note that the radar payloads do not have a cost attributed to them because it is highly variable and based on the hardware development process which is not covered in this project. All other cost values were given by the manufacturer or derived from previous purchasing experience while working on satellite development projects such as KUbeSat1.

Mass of both satellite designs meets the given requirements. The RX satellite can gain 2,000 grams while the TX satellite can gain over 5,000 grams. This margin allows for significant growth in the payload mass which is ideal as these systems are not yet a reality.

Recall that a single internal 3U stack is 320 mm. The table shows that all of the internal

components of the RX satellite design will fit within a 3U structure with a reasonable margin, of roughly 60 mm. A 6U frame can hold two 320 mm stacks, as such the TX satellite components will have a margin of almost 320 mm. Stack height margin is highly desirable, as payload components may grow and some modules may be changed out. The CAD figures presented at the beginning of this chapter implement a 10 mm space between each internal module to ensure conservative sizing. With a 10mm space between each internal module, the stack height of the RX satellite increases to 318 mm which is perfect for the 3U stack while the TX satellite would have an increased stack height of 368 mm which would exceed a 3U stack.

Volume, mass, and cost analysis provide an initial value based on the hardware selected and confirm that all requirements are met. Power analysis requires more in depth analysis that is best suited for a day in the life simulator, much like the simulation tool presented in the following chapter.

Chapter 4

Satellite Simulator

Every orbital mission, no matter the payload, requires analysis tools that provide confidence in the selected mission parameters. For the KRISP mission, a satellite simulator was developed to approximate the data coverage achieved and evaluate the proposed ConOps. As a reference, a flowchart of the developed simulator is given in Figure 4.1.

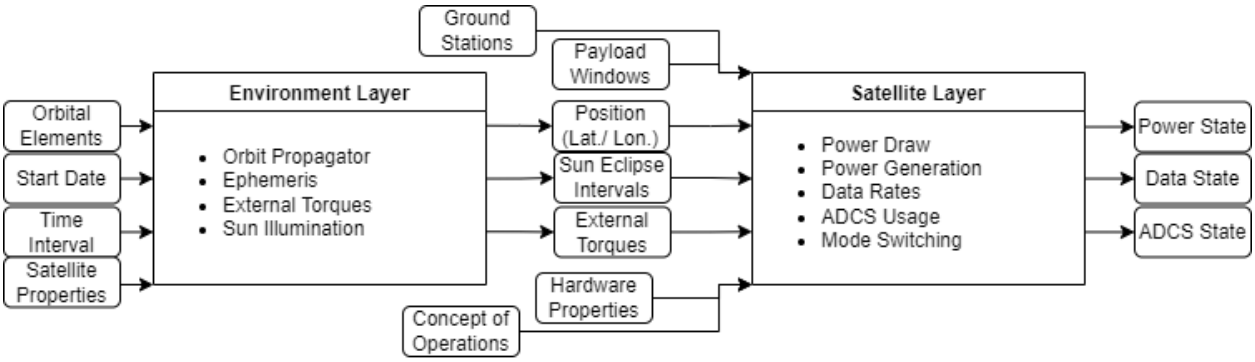

Figure 4.1: Flowchart of Satellite Simulator

A tool for simulating a satellite mission can be broken into two layers: 1) Environment and 2) Satellite. The Environment layer takes the inputs of initial orbital elements, a starting date, a time interval, and basic satellite properties to simulate everything external to the satellite. The Environment is driven by the orbit propagator which outputs the satellite position over the simulated time frame and uses this position to output eclipse intervals which inform incident solar power and external torques on the satellite. The Satellite layer requires the Environment layer position, eclipse intervals, and external torques as well as ground station information, payload windows, satellite hardware properties, and the ConOps to simulate the operational modes (e.g. Nominal, Low-Power, etc.) of the satellite as if on-orbit. Different operational modes will have ranging effects on the

satellite which will dictate states of power, data, and activation of different subsystems such as the ADCS.

This chapter details the satellite simulator tool development, and provides specific details of the Environment and Satellite layers. After defining the tool, some initial results are provided and discussed. Note that any results shown do not indicate an optimum design, but rather illustrate the capabilities of the analysis tool.

4.1 Environment Layer

The mathematical relationships needed to simulate the environment for spacecraft in LEO are encompassed in classical orbital mechanics[65] and spacecraft design[58, 59]. The Environment simulation can be described as integrating the equations of motions using a Runge-Kutta solver[66]. By solving the equations of motion, the position and velocity of the satellite can be found given an initial state and a sufficiently small time step. The environment layer handles classical orbital elements, Earth Centered Earth Fixed (ECEF) positions and velocities, latitudes and longitudes, and position vectors between different objects in the solar system. A representation of the coordinate system is illustrated in Figure 4.2. Note that the XYZ axes used in this report are equivalent to the

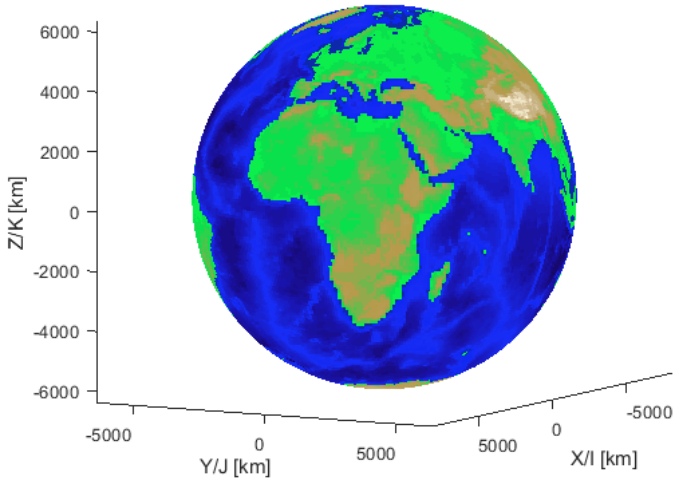

Figure 4.2: Orbital Coordinate Frame

IJK frame.

Inputs to the environment layer include a start date and time interval, initial orbital elements, and physical properties of the spacecraft. Initial time and orbital elements are converted to a position and velocity state vector $\left(\vec{X}\right)$ as shown in Equation 4.1, where x represents the position and $\dot{x}$ represents the velocity. A second representation is given for components in the IJK frame where r is a radius component and v is a velocity component.

$$\vec{X} = \begin{bmatrix} x \\ y \\ z \\ \dot{x} \\ \dot{y} \\ \dot{z} \end{bmatrix} = \begin{bmatrix} r_i \\ r_j \\ r_k \\ v_i \\ v_j \\ v_k \end{bmatrix} \tag{4.1}$$

The initial state vector is passed to the Runge-Kutta solver to propagate the orbit to some time in to the future. Propagating the orbit within this tool involves integrating the equations of motion for a satellite. The equations of motion output the velocity and acceleration values related to the change of the state vector as shown in Equation 4.2.

$$\dot{\vec{X}} = \begin{bmatrix} \dot{x} \\ \dot{y} \\ \dot{z} \\ \ddot{x} \\ \ddot{y} \\ \ddot{z} \end{bmatrix} = \begin{bmatrix} v_i \\ v_j \\ v_k \\ a_i \\ a_j \\ a_k \end{bmatrix} \tag{4.2}$$

Derivation of the equations of motion for LEO spacecraft begins with simple two-body motion

as shown in Equation 4.3[65]. In this equation μ is the standard gravitational parameter for Earth, r is the orbital radius, and $\hat{r}$ is the unit vector from the Earth's center in the direction of the satellite. Note that all constants used are given in Table B.1 of Appendix B.

$$\vec{a_{2-Body}} = -\frac{\mu}{r^2}\hat{r} \tag{4.3}$$

Like most orbital mechanics problems, it is necessary to include the effects of J_2. This effect is captured in Equation 4.4. R_{Earth} is the mean equatorial radius of Earth. J_2 is a well known perturbation used in orbit propagation[65].

$$\vec{a_{J_2}} = \frac{15\mu {R_{Earth}}^2 J_2 r_k^2}{2r^6}\hat{r} - \frac{3\mu {R_{Earth}}^2 J_2}{2r^5} * \begin{bmatrix} r_i \\ r_j \\ 3r_k \end{bmatrix} \tag{4.4}$$

The last contribution to the equations of motion is from perturbations due to drag. The equation for drag is shown in Equation 4.5. The relative velocity (V_A) is defined in Equation 4.6. $\dot{\theta}$ represents the rotation rate of Earth.

$$\vec{a_{drag}} = -\frac{1}{2}\rho\frac{C_D A}{m}|V_A|\vec{V_A} \tag{4.5}$$

$$\vec{V_A} = \begin{bmatrix} \dot{x} + \dot{\theta}y \\ \dot{y} - \dot{\theta}x \\ \dot{z} \end{bmatrix} \tag{4.6}$$

The drag calculation requires several spacecraft attributes such as the coefficient of drag (C_D), cross-sectional area (A), and mass (m). Drag also requires an approximate atmospheric density (ρ) which is given by the NRLMSISE-00 atmospheric model which implemented with the atmosnrlm-

sise00 function that is built into Matlab[67]. NRLMSISE-00 is a standard atmospheric model that relates density with several environmental factors such as solar conditions and geomagnetic indices[68]. Inputs to the Matlab function are altitude, latitude, longitude, year, day of the year, seconds, the 81 day average of F10.7 flux, the F10.7 flux of the previous day, and a vector of geomagnetic indices. The position and time variables can be calculated directly within the propagation functions using algorithms described in this work and simple addition of time since start to the specified propagation start date. The start date-time for all simulations is 1/1/2022 at 00:00:00. Time is tracked within the environment layer and is ticked forward for each time step. For the the inputs of flux and geomagnetic indices, these were set as constants for the simplicity in simulation and replication of this work. The F10.7 81 day average was set to 78.71, the F10.7 of the previous day was set to 78, and the geomagnetic vector was set to [3 3 3 2 3 3 4]. These values indicate a quiescent solar environment and limited geomagnetic activity. Given the correct inputs, the output of the Matlab function is atmospheric density at the satellite's location under the given environment.

All contributions of acceleration are then summed to get the total acceleration of the system.

$$\vec{a} = a_{2-\vec{Body}} + \vec{a_{J_2}} + a_{\vec{drag}} \tag{4.7}$$

Once the acceleration relationships have been established, the integration of the equations of motion can be executed. The method of choice for this project was Runge-Kutta[66]. This method is fourth-order accurate and widely used in the engineering community to solve problems related to differential equations or optimization. Execution of a Runge-Kutta solver requires a derivative function (given by accelerations in Equation 4.7), change in the independent variable (time), and the dependent variable (the state vector). This technique allows for the propagation of an orbit to any future time. The remaining Environment outputs depend on this propagated position.

Latitude and longitude on the surface of the Earth can be found with a given date-time and position. The method used takes ECEF position and time since simulation start to determine the rotation of the Earth and the resulting latitude and longitude of the spacecraft. Algorithms for this conversion came from Vallado[65] and adapted to include the Earth's rotation.

Determining when the spacecraft is illuminated by the Sun requires a position vector between the Earth and Sun. Highly precise estimates of celestial positions are typically found using ephemerides which are calculated using planetary orbital elements and propagating the orbit by solving the Kepler equation. However, developing a full set of ephemerides brings unnecessary precision and complexity that is beyond the initial scope of this project. For a LEO mission, position of the Sun relative to Earth and the satellite are only necessary for determining solar illumination. A simple method for determining this position within one arc minute of accuracy[65], is presented in Algorithm 29 of the Vallado text[65]. Input to this algorithm is the time in Julian date format and the output is the position vector from Earth to the Sun.

To determine if the satellite is illuminated by the Sun, the vector between Earth and the Sun ($r\vec{_{Sun}}$) is compared with the vector between Earth and the satellite ($r\vec{_{Sat}}$). The presented method determines if line of sight is possible between the satellite and the Sun using Algorithm 35 from Vallado[65]. First, Equation 4.8 finds the dot product between the two position vectors. Next, Equation 4.9 solves for an intermediate value (τ_{min}) which dictates the eclipse check.

$$RdR = -\left(r\vec{_{Sun}} \cdot r\vec{_{Sat}}\right) \tag{4.8}$$

$$\tau_{min} = \frac{|r\vec{_{Sat}}|^2 + RdR}{|r\vec{_{Sat}}|^2 + |r\vec{_{Sun}}|^2 + 2RdR} \tag{4.9}$$

If τ_{min} is less than zero or greater than one, the satellite has line of sight to the Sun. If not, a second check must be done by evaluating the inequality given in Equation 4.10. If it is true, then there is line of sight between the satellite and the Sun. For all other cases, the Earth eclipses the satellite.

$$(1 - \tau_{min})|r\vec{_{Sat}}|^2 - RdR\ \tau_{min} \geq R_{Earth}^2 \tag{4.10}$$

Lastly, the external torques experienced by the satellite can be calculated. Incident torques and rotational values can be represented in several different ways, the most common being quaternions.

However, for the first iterations in satellite design it is reasonably conservative to calculate the torque magnitude rather than individual components and expect that torque to be nulled by a single reaction wheel. This process of tracking and nulling external torques provides insight to the momentum buildup within the ADCS. As explained in the Subsection 3.4.2, a momentum dump must be executed before a reaction wheel has fully saturated.

Within this simulator, the contributing torques on the satellite are from: gravity gradient, drag, Earth's magnetic field, and solar radiation pressure. Calculation of these values requires knowledge of position, physical satellite properties, and sun illumination state. All algorithms used are from equations given in Chapter 5 of Brown's Spacecraft Design[59].

Outputs of the environment layer cover the true position and velocity of the satellite with time, the ground track (or latitude and longitude) of the spacecraft, sun illumination intervals, and total external torques on the satellite. All of this information is passed to the Satellite layer and additional errors are not considered in the Environment layer. Rather, error is introduced in the Satellite layer as the precision and accuracy of the satellite's environmental knowledge is dictated by the hardware. To ensure the environment layer is as accurate as possible certain validation and verification steps were taken during the development process.

4.1.1 Validation

In modeling any physical system, it is relevant to validate the model against existing sources. Commonly, text books are useful in validating models as they provide example problems with input and output values as well as intermediate values with full transparency in solving the example. A review of existing literature (not only textbooks, but published journal and conference papers as well) did not reveal any published example with which to validate the propagation model. Other validation sources include industry standard computer programs used for a similar task. A major shortcoming of using proprietary programs for validating models is the lack of transparency. Some refer to these programs as "black boxes" as the user gives it input data and receives output data with little to no knowledge of the work done to get that output. It is relevant to keep the "black box"

nature of these programs in mind when considering the validity of the developed model.

The model developed for the Environment layer, as presented above, was built using methods published by Vallado[65] unless otherwise stated. All of the algorithms, to include 2-Body propagation, were confirmed against the relevant examples provided in the Vallado textbook. Propagation is extended by the derivation of the J2 terms and the use of perturbations due to drag. These are not explicitly developed by Vallado and as such do not have an associated example. These methods were developed as a part of coursework at the University of Kansas and were verified against the work of other students as well as work done by the instructor. This verification matched the results of other independently developed propagators to the nanometer (1e-9). Note this verification was done in three separate stages: 2-Body only, 2-Body+J2, and 2-Body+J2+drag. The drag model used in coursework was an exponential drag model while the model used in this work is the NRLMSISE-00 model built-in to Matlab. NRLMSISE-00 is a modern and commonly used drag model that provides realistic density values based on the input solar and geomagnetic conditions.

As a part of this work, a further validation step was taken to verify the propagation model used by comparing results against the Systems Toolkit (STK) from AGI[69]. Through the university an educational license of the base package was obtained. To verify the propagator against this program a start date, time step, and starting state vector are required. The program is able to propagate under different perturbations and as such a two-step verification can take place: 2-Body only and J2+Drag. For both cases, a Sun synchronous orbit at 555 km altitude was used (see Table 3.1) using the same propagation date as the Environment layer (noted above). Note that this program gives little to no details about the propagation techniques and the constants used. It was found during the verification process that some constants in STK, such as gravitational parameter μ, were different from values defined by Vallado (which were used by the author). Not only were some constants different, the density values for each propagation step is not available to the user. Matching these underlying values is critical to correctly validating any orbital propagator. Even so, it is worthwhile to see how well the propagator developed above matches the industry standard orbital propagation

program.

Using the High-Precision Orbit Propagator (HPOP) within STK, two orbits of a single satellite in a Sun synchronous orbit were calculated. When using 260 time steps for the propagation, the maximum offset in the 2-Body case was 3.96 meters after two orbits. For J2+drag, 206 time steps for propagation yielded a 396 meter maximum offset after two orbits. Note that the NRLMSISE-00 model was designated for the STK simulation, but it is unclear what solar conditions were used. Given that some critical information is missing, the agreement of the two solutions is within the uncertainty of the model.

To provide published orbit propagation verification source, a validation dataset has been generated. In Appendix C, there are two sets of validation data that can be used by other researchers to validate their code against. The code used for this project has also been posted to Github for future researchers to reference[70].

4.2 Satellite Layer

Given the external stimuli or inputs from the Environment layer, the Satellite layer interprets and reacts based on the ConOps. This layer keeps track of the satellite state, which includes: battery storage, data storage, and reaction wheel momentum buildup. Success of a mission depends on balancing these, as such it is important to accurately simulate them.

In order to simulate the operation of a satellite, hardware properties and the ConOps must be first determined. Hardware dictates the power and data rates for each subsystem. Trade studies have been conducted to determine an initial satellite configuration with details found in Subsection 3.4.3.

As hardware was selected, the ConOps for the mission was formed simultaneously. The ConOps dictates when and how the selected hardware will run given external stimuli and current satellite state. These operational switches revolve around the operation of the payload, telemetry of the data, charging of the batteries, and overall subsystem maintenance. The nature of the payload drives all mission decisions and operations. Within the ConOps it is also necessary to rank the execution of any particular mode so that the overriding priorities can be established.

With all of these key pieces of information, the Satellite layer acts as the on-board computer by dictating and tracking the operation of each subsystem. Namely the power, data rate, and orientation of the satellite. Simulated over time, these values describe all of the key details for a mission of any kind.

Algorithms developed to simulate the satellite layer requires hardware properties, ConOps, ground station locations and bands, payload windows, and outputs of the Environment layer. By iterating over the given time interval, the Satellite layer dictates the operational mode for the satellite at each time step. The mode selection is dictated by the orbital position, battery storage, data storage, and other satellite state values defined by the ConOps. If two modes are valid for that time step, the priority defines which will override and become the mode for that time step. Once the mode is determined, the power and data states across the satellite are recorded.

Apart from operational mode, location of the satellite relative to ground stations and payload opportunities is also relevant. Considering a ground station flyover, the satellite layer determines if the current location is within the beamwidth of the ground station and which frequency bands can be used. The frequency band dictates the hardware used during the flyover which effects the downlink speed as well as the power use. Note that multiple bands can be used in a single flyover. Payload opportunities are much simpler. The satellite layer checks that it is within the defined geographic window and operates the payload at full capacity. Telemetry opportunities override payload opportunities within the algorithm but these are selected so that there is no overlap.

Outputs of the Satellite layer over time include power draw by subsystem, battery storage, data storage, satellite torques, and operational modes. This simulation can rapidly produce the necessary results required for iterating to optimize satellite designs.

4.3 Initial Simulation Results

Executing the full satellite simulation gives information on the satellite state and position with time. Results displayed from the Environment layer pertain only to forces external to the satellite. All other results portray the expected state internal to the satellite based on the details given in

Section 4.2.

A three dimensional representation of the orbit has been plotted in Figure 4.3. This illustrates the general path of the satellite in 3D space for the orbit defined in Table 3.1, and gives a visual for the orbit relative to the Earth.

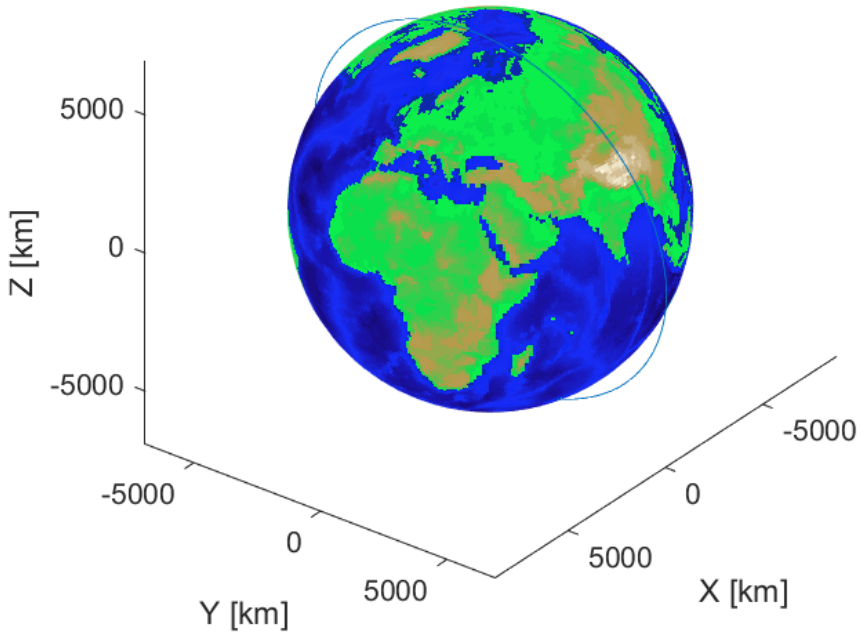

Figure 4.3: 3D Representation of a Single Orbit

4.3.1 Coverage

Using the orbit propagator outlined in the previous section, the coverage over the polar ice sheets can be determined. Radar windows are defined by a central point and a radial distance from that point. The radar windows used for this simulation are defined in Table 4.1.

Table 4.1: Radar Sounding Windows

Target	Lat (deg. N)	Lon (deg. E)	Radius (km)
Greenland Ice Sheet	71.00	-43.00	1300
Antarctic Ice Sheet	-87.00	90.00	2500

By projecting the satellite's position onto the Earth's surface, a ground track of the orbit can be determined. To illustrate the potential data coverage, the Environment layer was used to propagate

100 and 500 orbits into the future. Figure 4.4 illustrates simulations of 100 and 500 orbits over the Antarctic continent. For reference, 100 orbits is approximately seven days and 500 orbits is roughly one month. Note that the lines displayed in these plots represent flyover opportunities given raw position data from the Environment layer. These lines do not represent data collected within the Satellite layer.

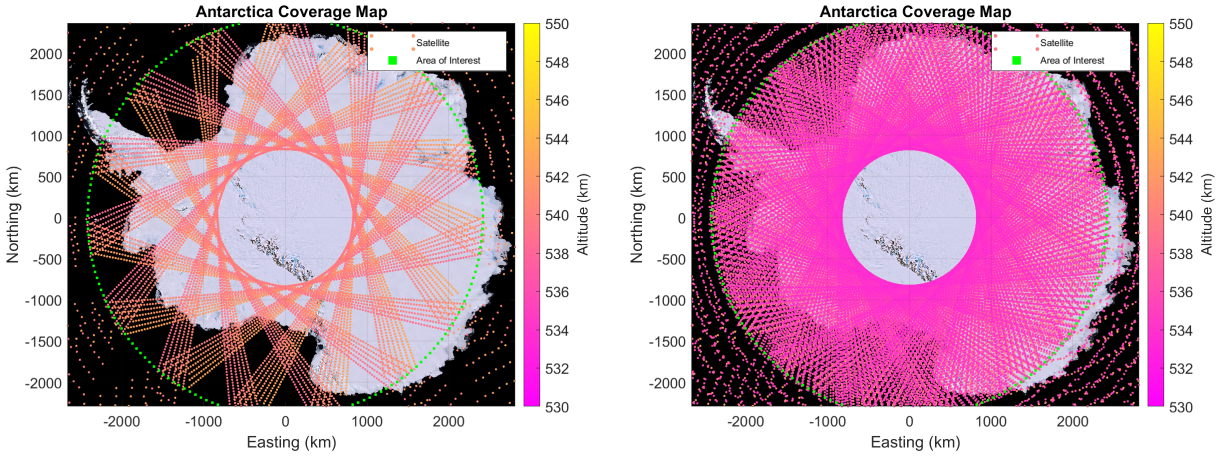

(a) Simulation of 100 Orbits

(b) Simulation of 500 Orbits

Figure 4.4: Simulated Coverage over Antarctica

Over Antarctica, the satellite is able to cover major portions of the ice sheet but there is a coverage gap near the center of the continent. The circle center can be moved by altering the initial orbital elements, but it is expected to be present for short time simulations (<one year). For simulations of greater than one year, the Earth's axis will precess and naturally allow for coverage within the circle. However, due to the lifespan limitations of nanosatellites, portions of this coverage gap will still exist without follow on missions.

Figure 4.5 illustrates the data coverage achieved over Greenland for a simulation of 100 and 500 orbits, respectively.

Coverage over Greenland is sparser as compared to Antarctica.This is expected due to the lower latitudes of this continent resulting in fewer fly over opportunities. Regardless, it is expected that comparable coverage of the Greenland ice sheets could be achieved within the nanosatellite lifetime. Repeat pass measurements could also be possible after significant time intervals (≥one

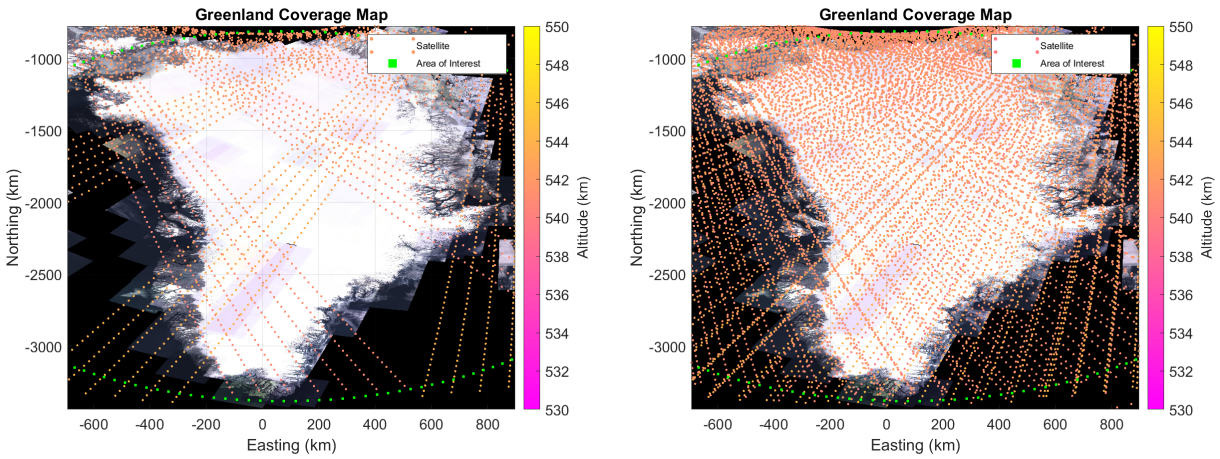

(a) Simulation of 100 Orbits

(b) Simulation of 500 Orbits

Figure 4.5: Coverage over Greenland from Orbital Simulations

year). Recall that the total line kilometers of data used to make recent Greenland bed elevation maps using airborne radar data was 414,000 line-km collected over 20 years[16]. These simulated coverage maps indicate that the proposed nanosatellite constellation would be able to collect 144,500 and 717,700 line-km of sounding data from Greenland for 100 and 500 orbits, respectively. Within less than a month from launch, the nanosatellite constellation will have eclipsed the data collected from all airborne platforms used for Greenland bed elevation maps.

4.3.2 Day in the Life

Next, the typical daily operations of the vehicle can be assessed. Aside from satellite inputs given in Table 3.5 and Table A.2, it is also necessary to define the available ground stations to determine regular operations. The details of various available ground stations are given in Table 4.2.

Table 4.2: Telemetry Windows

Ground Station	Lat (deg. N)	Lon (deg. E)	Beamwidth (deg.)	RX Bands
Hawksnest	38.97	-95.24	131.00	UHF, S, X
North Pole	64.80	-147.65	131.00	S, X
South Point	19.00	-155.67	131.00	S, X
Punta Arenas	-52.93	-70.85	131.00	S, X

The Hawksnest ground station (Lawrence, KS) was developed and deployed by the KUbeSat

organization based out of the University of Kansas. Currently, only UHF operations are supported, but future efforts are underway to expand capabilities to S- and X-band transmissions. The remaining stations are a subset of a list of X-band ground stations available through the Swedish Space Corporation [71]. Using these additional ground station requires contracting with the Swedish Space Corporation for the KRISP mission. Use of ground station networks (private or public) is common practice for nanosatellite missions to provide more telemetry opportunities. Note that this analysis is only based on a single satellite and as such only one communication connection between satellite and ground station is considered. For the full constellation, multiple connections will be necessary to downlink all of the radar data. To ensure multiple connections are possible, further details will be needed from the selected ground station network (specifically the number of concurrent satellite connections) and decisions will need to be made as to the number of ground stations necessary to perform this mission with limited interruption. In the case that all satellites can concurrently telemeter data, the single satellite analysis shown below is an analogous result. Notably, radar operations will not be possible for the entire satellite lifetime as it is limited by relative spacing over the targets. Therefore, any excess data can be fully downlinked after the end of the UML period and before satellite decommission.

To visualize the payload and telemetry opportunities, a ground track over five orbits was generated. The result is shown in Figure 4.6. The red lines represent the telemetry windows defined by Table 4.2 and the pink lines represent the payload windows defined by Table 4.1. As the figure illustrates, groundstations are not in sight every orbit, but there is a payload opportunity every orbit. This disparity is the driver for including a Data Purge mode within the ConOps.

Over the course of operation, the total power of the satellite (generated and drawn) is calculated. Figure 4.7 shows the power values over two orbits. Interestingly, the average power generated is greater than the average power used by two Watts. This means the battery will remain near full charge over the mission lifetime and quickly charge, especially when the satellite is not operating in Nominal mode. Power generation occurs over roughly 60 percent of each orbit. It is also noticeable that the power generation is not a constant value, this is expected because the satellite

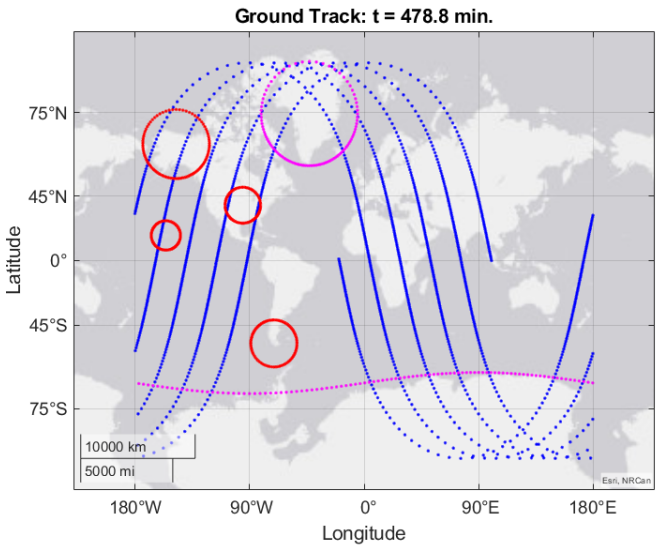

Figure 4.6: Ground Track over Five Orbits

is set to hold orientation relative to Earth's surface allowing for rotation about only one axis. This limited control scenario does not allow for full illumination of all solar panels. Therefore each power generation value represents the maximum possible per the orientation settings. This is a preliminary assessment that yields conservative values for achievable solar power generation.

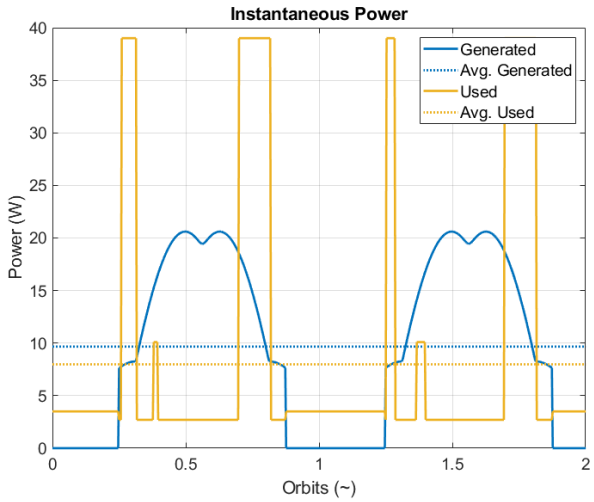

Figure 4.7: Satellite Power Draw and Generation vs. Time

Lengthening the time interval to four orbits, the power draw from each subsystem is plotted in Figure 4.8. Figure 4.8a illustrates power draw for all of the satellite subsystems. Figure 4.8b illustrates power draw for the same simulation but limits the y-axis to provide a better visual of the

subsystem power draw by excluding the payload.

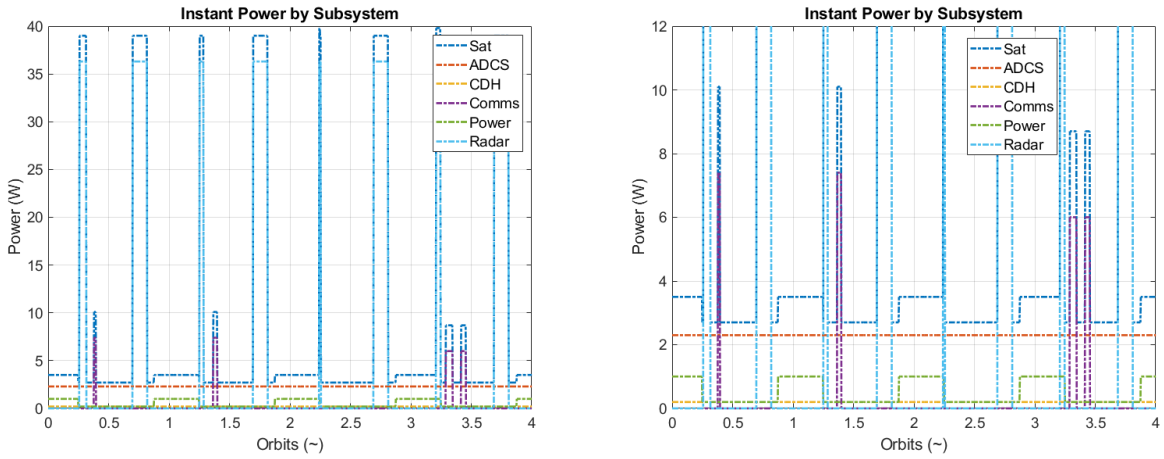

(a) All Subsystems

(b) Subsystems minus Payload

Figure 4.8: Subsystem Power vs. Time

As illustrated in the Figure 4.8a, there is a large power usage when the payload is operated (a 36W difference from baseline) or communicating with the ground station (almost 8W difference from baseline). Another feature is the slight increase in the power subsystem usage while eclipsed by the Earth which happens first at 0.8 orbits and repeats every orbit. This bump represents the battery heater turning on. This operation is not noted in the ConOps as this is a built-in functionality to the battery which can not be altered. Therefore a conservative estimate is to run the battery heater for the entire eclipse duration.

Further simulating the satellite platform to 150 orbits, long-term cycles can be established for power cycles, momentum build-up, battery storage, and data state. These trends are plotted in Figure 4.9. First presented is the operational mode chart given in Figure 4.9a. Although all modes noted in Table 3.5 are available to the simulation, only the Nominal and Data Purge modes are entered in this configuration. Low Power mode is not entered (therefore not displayed) as the threshold to enter Low Power was set at 25 Whr which is less than the amount of instant battery power stored on the satellite for this simulation interval. This is mainly due to the nature of Data Purge as no other operations take place on the satellite so the power draw is relatively low when not collecting data, allowing the batteries to fully recharge. Momentum Buildup is displayed but is

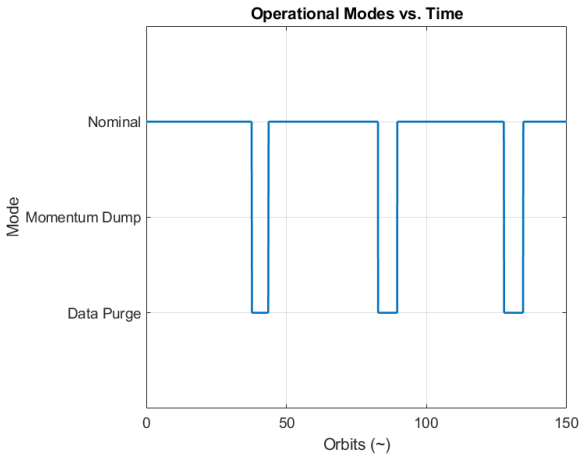

(a) Operational Mode vs. Time

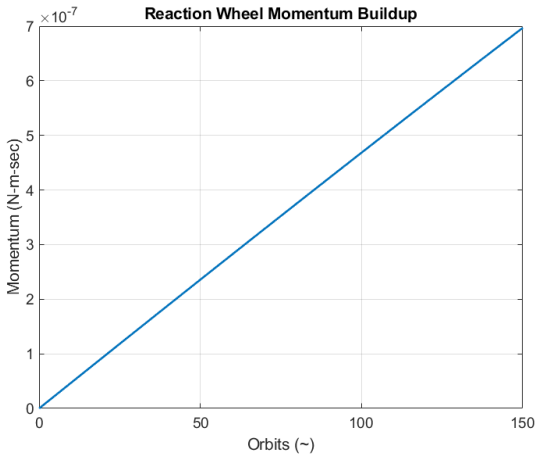

(b) Momentum Buildup vs. Time

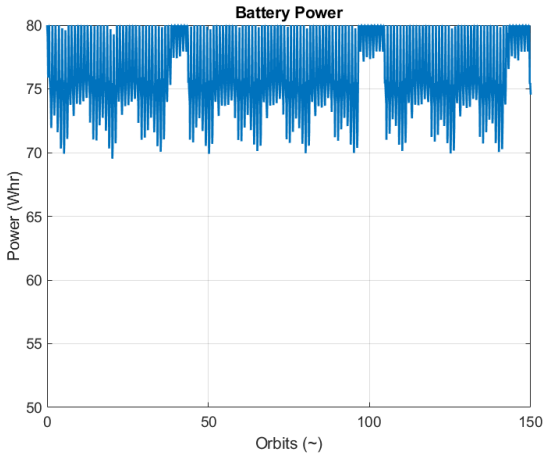

(c) Battery Storage vs. Time

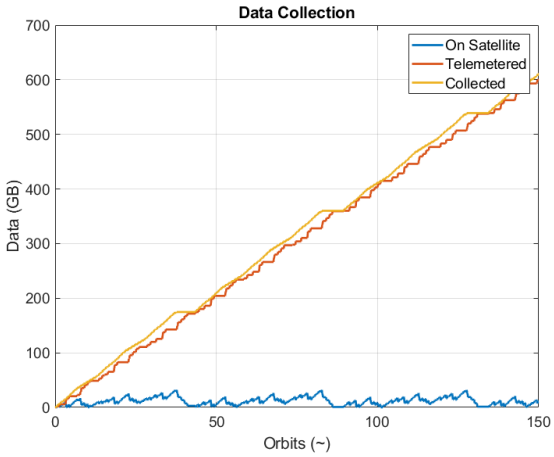

(d) Data vs. Time

Figure 4.9: Satellite Results from 150 Orbit Simulation

never entered as the reaction wheel momentum buildup threshold is 0.01 N-m-sec which is much greater than the momentum up to this point in the simulation timeline. This simulation simply maintains satellite orientation and as such does not put much stress on the ADCS as compared to missions with many attitude maneuvers. Data purge is the only mode that is entered (when data exceeds 32 GB "On Satellite") to make sure all data products are sent soon after collection. This could be adapted to better match the mission cycle as the total data storage on a single satellite can also be expanded. The operational cycle takes roughly 47 orbits to repeat with 40 orbits in Nominal and 6.7 orbits in Data Purge mode.

Figure 4.9b is the momentum buildup in the ADCS over 150 orbits. Note that the reaction

wheel saturation value for the selected ADCS is 10E-3 N-m-sec. The plot given in Figure 4.9b shows the minimal accumulation of external torques up to 7E-7 N-m-sec, indicating an extremely long time until saturation. Although the momentum buildup relationships used in this simulator are low fidelity, this result implies that even significantly larger torques could be easily handled by the selected ADCS.

The last two plots in Figure 4.9 show the battery storage (Figure 4.9c) and data state (Figure 4.9d) with time. Cycles in these plots follow the trends noted in all other previous plots. Note in the data plot, the "On Satellite" line represents the state of stored data with each time step, the "Telemetered" line represents the data received by ground stations, and the "Collected" line represents the total accumulation of data collected by the payload. Note that the "On Satellite" state will actively change as the satellite collects and subsequently telemeters data. Over 150 orbits, there is 604 GB collected by an individual satellite and up to 600 GB received by the ground stations.

Based on the results that have been presented for the KRISP mission, there is confidence that an individual satellite meets the necessary requirements with a reasonable amount of margin in the areas of reaction wheel saturation, power state, and data state. It is recognized that the analysis presented above is only for a single TX satellite. Even so, the results for RX satellites will be similar. Considerations will need to be made with regards to the ground stations needed for the mission. Satellites in the constellation will either need concurrent connections with each ground station or the total number of ground stations will need to be increased to maximize the telemetry opportunities. Recall that this constellation mission is only expected to effectively collect radar data for a portion of the total mission lifetime (defined by UML) and no data collection is expected after this interval. Even so, data collection only happens when the constellation is within in the ideal configuration which will not always occur thereby limiting the amount of data on each individual satellite further than the analysis above shows (as that was for a single satellite that always operated when above the target). Therefore, telemetry of all data is a non-issue but still worth considering further along in the mission development process.

The previous analysis demonstrated that a single satellite could operate within the necessary

bounds of the mission; however, the multi-satellite configuration will impose further operating restrictions. To properly conduct this mission, spacing between satellites is critical to effectively operate the radar and avoid a collision. The following chapter will utilize the Environment layer of the satellite simulator to propagate the orbits of multiple satellites and track their relative positions. This chapter will culminate in a Monte Carlo analysis of the accuracy required during launch vehicle jettison, which is a major contribution of this work, and indicate the likelihood of success for this uncontrolled constellation.

Chapter 5

Constellation Investigation

After establishing the design of the individual constituents of the nanosatellite constellation in Chapter 4, the main investigation of the uncontrolled constellation is presented. This chapter aims to answer several driving questions related to this mission concept. The first question is: What is the ideal constellation configuration in terms of orbital element offsets? Using the answer from this question, the following question becomes: What is the acceptable error during the orbit injection process which will result in limited collision risk for the first two orbits? Note that only two orbits are investigated as published works have established that this time interval has the highest collision risk and this interval indicates the time after jettison required to confirm connection with each satellite in the constellation, thereby moving the mission to the Nominal operation mode. Lastly, the over arching question of this entire document can be answered: Is the uncontrolled constellation well suited for radar ice sounding from orbit? These three questions and their subsequent answers mark the major contributions of this work. As noted previously, the jettison analysis of controlled constellations (or clusters) has been presented in the literature. The unique contribution of this work comes from not only investigating the uncontrolled constellation (which is not discussed in literature) but also investigating a constellation of satellites operating in such close proximity (on the order of meters when the bulk of available literature focuses on kilometers).

Key to this mission is the collection of large amounts of data as well as a long mission lifetime. In answering the above questions, the metrics of interest are: the amount of data collected in line-km and the Useful Mission Lifetime (UML). UML is defined as the end of life for the mission with regards to either data collection or substantial collision risk. Collision risk will be informed by the relative offset between satellite constituents. Whenever any two satellites come within 0.25

meters of each other, a failure is registered thereby ending the mission and setting UML. Although the maximum physical dimension of each satellite is driven by the extended VHF antenna elements (~0.6 meters from satellite center), these elements are not rigid and attitude maneuvers could be done to reduce the chance of contact between adjacent satellite antennas. Still, a reasonable minimum distance must be defined to indicate excessive collision risk. As such, the 0.25 meter limit is set as a mission ending collision is assured when the relative distance between two satellites are within this threshold. If the satellites never fall below this collision threshold, the UML will be defined by the last data collection point. As the satellites naturally drift apart, there will be a point at which ideal array spacing necessary for data collection can not be maintained. Note that each simulation will propagate the satellite orbits the entire indicated duration and will not be ended before that. Recall that for data collection, previous studies showed that the cross-track spacing should be between a quarter-wavelength and not much greater than two full wavelengths, as discussed in Section 3.1.

Data collection indicated in this chapter is the total possible accumulation of sounding data. In this assessment, the unit used to described data collected is "line-km." This data characterization does not consider whether the bed is actually detected, and rather is equivalent to the coverage over the ice sheet. While the author recognizes the limits in this assessment of data collected, without the development of a robust, high-fidelity clutter simulator for orbital ice depth sounding, a more relevant assessment of ice bottom line-kms is not possible. The development and inclusion of a high-fidelity clutter simulator for data quantification is left for future study. As detection of the ice-bedrock interface is not guaranteed for each data collection point, only a subset of the data collected could be used for the respective DEMs.

Naturally, the first step of this chapter was to explore the configuration design space by first determining the variables that have the most effect and then narrowing the scope to select an ideal constellation configuration point. The point selected cannot be considered optimal as no optimization methods were used; however, the ideal point identified is likely near the optimal point such that any formal optimization analysis would not significantly improve the data collected

and UML. The ideal point was selected based on a brute force sweep through combinations of the four orbital elements of interest: Argument of Perigee, Inclination, Right Ascension of the Ascending Node, and True Anomaly. The first sweep analyzed a large design space to find areas of interest. These smaller areas of interest were then examined further using smaller steps sizes to find the ideal constellation configuration, thereby answering the first question of this investigation. The goal of this investigation is to define ideal orbital element offsets based on the driving orbit defined in Section 3.2. The UML, data collected, and collision risk are then discussed for the ideal constellation configuration.

Using the ideal configuration from the previous step, a Monte Carlo study was done to determine how errors in the launch vehicle jettison process will affect mission success. During orbit injection the ideal position and velocities will not be achieved as orbit injection is not a perfect process and therefore has associated errors that must be analyzed. Propulsed mission concepts would be able to overcome the minor deviations during orbit injection, but the proposed mission will not have this capability. Deviations present at jettison will propagate through the lifetime of the uncontrolled mission. The goal of this study is to determine the range of acceptable errors in the jettison process, and asses how that affects the UML. Using the metrics of UML and data collected, conclusions were made regarding the acceptable level of deviation allowed in the orbit injection phase, thereby answering the second major question.

Finally, by bringing together all of the results of these two studies, conclusions were drawn as to whether this unpropulsed mission concept would be successful. Previous chapters have already shown that a single nanosatellite would perform well in maintaining control for this mission type. The ultimate goal of this chapter is to determine if the uncontrolled constellation is viable for the defined mission.

5.1 Ideal Configuration Selection

To select the ideal constellation configuration, a broad sweep of the independent variables and their combinations was implemented in the constellation orbit propagator. The variables of interest are

orbital element offsets in: Argument of Perigee (w), Inclination (i), True Anomaly (ν), and Right Ascension (Ω). By offsetting the position of constellation constituents by small amounts, the orbits of the eight satellites are propagated forward to determine the amount of data collected, the UML, and the chance of collision.

Finding the ideal constellation configuration is a computationally expensive process. To simulate 206 time steps per orbit for 120 orbits of eight satellites and performing the relevant post-calculations takes approximately nine minutes on a single CPU core. Even with the parallel processing capabilities of Matlab, with up to 16 cores available, a single configuration sweep of 40 points can take upwards of two hours. To properly conduct this search for an ideal point, over 1000 points were simulated. After propagating each point, post-calculations must be done to quantify the results. Post-calculations focus on determining the relative position between satellites to evaluate the amount of data collected, the collision risk, and the UML.

During propagation, the position of each satellite is considered from the ECEF frame. For post-calculations of the constellation, the satellite positions are rotated in to the RSW frame which is better suited for relative position analysis. The rotation algorithm used was developed by Vallado[65]. Similar to other Environment layer algorithms, this rotation was verified against available Vallado examples. Once rotated, the components of satellite position become elevation, cross-track, and along-track. These components are more familiar when considering radar antenna array performance and are critical to the analysis that follows. Using the relative positions between satellites, it is determined whether the constellation can collect data while over the target, and it is determined if the collision risk is too high thereby ending the mission.

To collect data, the cross-track spacing between satellites must be greater than a quarter-wavelength (~50 centimeters) but less than two and a half wavelengths (~five meters). These limits were selected based on the MVDR study done by the author[38] and experience with array processing. The lower limit could be closer to zero but a quarter-wavelength is conservative to ensure post-processing is possible. The upper limit of two and half wavelengths is not much larger than the upper limit of the MVDR study, which was two wavelengths, but as indicated, MVDR

was able to fully compensate for two wavelengths of known offsets. Therefore it is expected that increasing the upper limit by a half wavelength will not greatly affect the post-processing capability of MVDR. When the satellite constituents fall within these relative cross-track limits while over the targets of Antarctica or Greenland, data collection occurs. Checks for data collection occur at each time step of the simulation. Data is only accumulated when data collection is registered for two sequential time steps. Data collection focuses on the cross-track offsets of the satellites while collision risk considers the absolute offsets between satellites.

As the satellites go through an orbit, the constellation will contract and shift based on the equations of orbital mechanics. At certain points, the satellites will come together very closely. These close approaches should be carefully considered as these are the instances of the highest collision risk. For the simulations presented, when any two satellites have a relative offset of 25 centimeters or below, a failure is registered as the collision risk quickly approaches 100%. By failing in this way, the UML is set.

The last metric of interest is the UML. This metric gives an estimate of the mission lifetime based on either the ability to collect data or the failure of the constellation due to collision, whichever is shorter. The goal in finding the ideal constellation configuration is to reduce the risk of collision, maximize data collected, and maximize UML. First, a broad sweep of the large design space must be investigated.

5.1.1 Broad Sweep

The first simulations to determine the ideal constellation configuration require a broad sweep of the four independent orbital elements. For each element, its value defines the relative offset between satellites within the constellation. An Inclination value of 2e-6 radians relates to a zero radian offset for the first satellite, a 2e-6 radian offset for the second satellite, a 4e-6 radian offset for the third satellite, and so on. These offsets are applied directly to the driving orbit, given in Table 3.1. Note that the orbital elements of the first satellite are always defined as the driving orbit.

For the first results presented in this section, a broad sweep of offsets for each of the four orbital

elements of interest was conducted. It was known from the outset that Inclination offset would likely be the most significant parameter in this step, therefore the first plotted results show the effects of varying one of the three remaining orbital elements along with varying the Inclination. This provides a glimpse at the four dimensional design space. All offset combinations are simulated, but it is not possible to visualize these results. Offset combinations of three or more elements are discussed when relevant. The range of offsets for this first simulation are given in Table 5.1. Also given is the number points including and between the maximum and minimum values. The offset values were limited based on previous broader sweeps done by the author.

Table 5.1: Orbital Element Offset Ranges for Results in Figure 5.1

Orbital Element	Inclination (i)	Arg. of Perigee (w)	Right Ascen. (Ω)	True Anomaly (ν)
Min Offset (rad.)	5.0E-07	0.0E+00	0.0E+00	0.0E+00
Max Offset (rad.)	1.5E-05	2.0E-07	1.5E-06	3.0E-07
# of Points	10	5	5	5

The first sets of simulations were run for 120 orbits (~one week) as the mission UML was unknown at the outset. Within one to two orbits after launch vehicle jettison, ground station connections would be established with all satellites, and the mission would be considered in the Nominal operational mode. Simulations done in this section assume the constellation is always in the Nominal operational mode. The ideal configuration is selected such that Nominal operation and subsequent data collection is the most ideal. Although a long UML is desirable for a cost-effective mission, it is more important to find a configuration that collects high quality datasets in a reasonable amount of time rather than a configuration that collects sparse datasets over long periods of time. The motivation of desiring high quality data rather than mission lifetime is driven by the implications of this study beyond the uncontrolled constellation. If the ideal constellation configuration is found to have less than 120 orbits of UML, especially when limited by excessive collision risk, an uncontrolled constellation will not be considered viable as on-orbit collision will certainly lead to space debris which is an unacceptable outcome of this mission. In this case, it is recommended that the ideal configuration should be evaluated for a propulsed mission concept in follow-on work beyond this report.

Shown in Figure 5.1 are the results of the first broad simulation. The three subfigures of Figure 5.1 show the results of one element (top to bottom: Argument of Perigee, Right Ascension, and True Anomaly) combined with Inclination while all other offsets set to zero. For each subfigure, there are three subplots which, from left to right, indicate: the amount of data collected within the UML, the UML of the constellation, and the minimum distance between two satellites within the propagation time interval (120 orbits). Note that the minimum distance plotted is not necessarily the distance at which collision caused the UML to be set, but rather the absolute minimum distance between two satellites during the propagation interval. These plots provide a way to visualize the results for a combination of two orbital element offsets, but these do not represent the full set of simulations completed. As there could be up to four-nonzero orbital element offsets, these simulations were done concurrent with the results shown here and notable trends will be discussed as necessary.

The first apparent result is that the combination of Inclination and Right Ascension achieves the largest amount of data collected as seen by the far left plot of Figure 5.1b. Compared to the data results for the other two orbital elements combined with Inclination, shown in Figure 5.1a and Figure 5.1c, their offsets do not increase the amount of data collected. It is known that the UML of all cases is set by the collision risk as all of the far right plots in Figure 5.1 show that the minimum offset between any two satellites during propagation is less than 0.25 meters. The darkest blue areas on the left and middle plots shown indicate that failure happens quickly, within the first orbit, and little to no data is collected. The maximum data collected in that first orbit is on the order of 2,000 line-km, which relates to a single pass over Greenland.

Recall that the amount of radar data used to generate the Greenland bed elevation maps was on the order of 414,000 line-km collected over 20 years[16]. Now, consider the two clear maximum data points shown in Figure 5.1b. At an Inclination offset of 3.722e-6 radians and a Right Ascension offset of 1.125e-6 radians, the data collected for this point exceeds 100,000 line-km with a UML of 20 orbits. With an Inclination offset of 1.017e-5 radians and a Right Ascension offset of 1.125e-6 radians, the constellation was able to collect slightly more data than the other maximum point (by

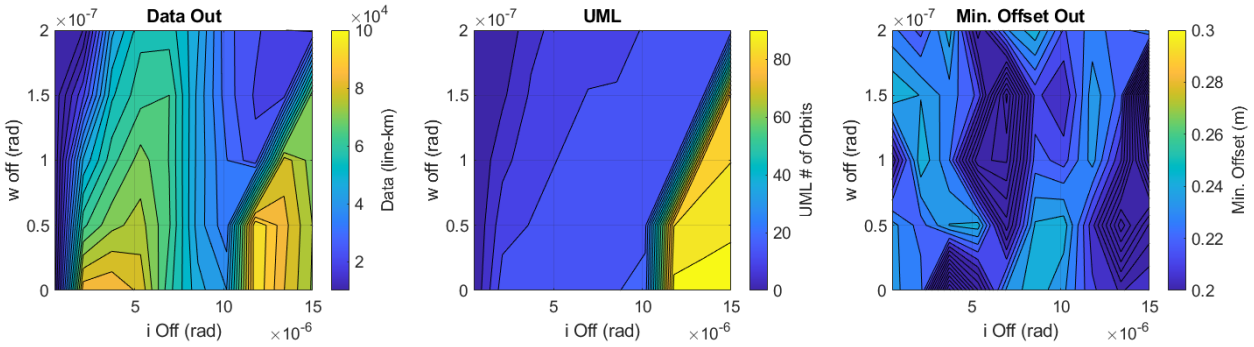

(a) Inclination with Argument of Perigee

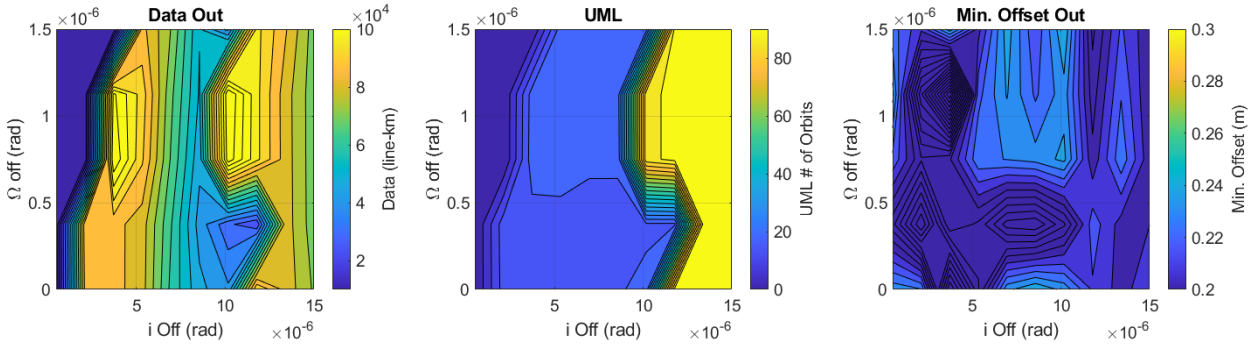

(b) Inclination with Right Ascension

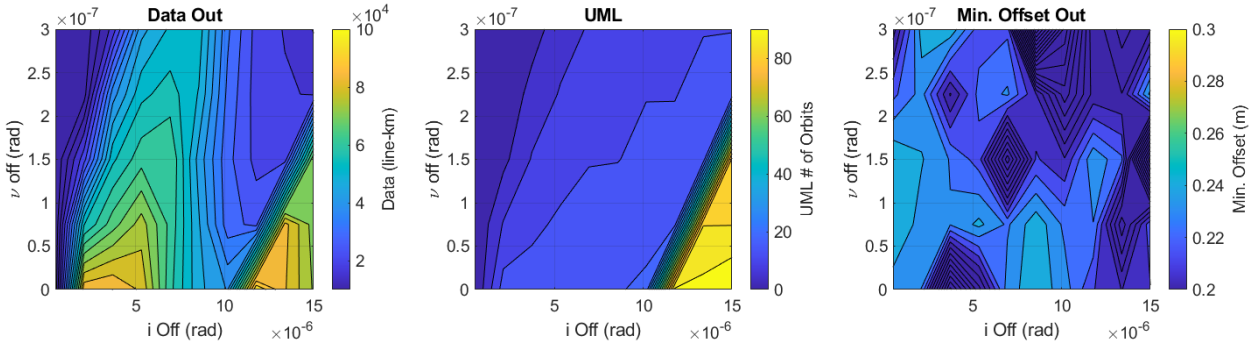

(c) Inclination with True Anomaly

Figure 5.1: Data Collected, UML, and Minimum Offset of Broad Sweep

10,000 line-km) with a UML of 87 orbits. Both of these maximum points have the UML set by collision risk as the minimum distances in the far right plot of Figure 5.1b are all less than 0.25 m. These two points are interesting as the UML is significantly different while the data collected is roughly the same. Note that the UML for both of these points is far shorter than desired, as it was indicated at the outset that 120 orbits is the minimum to consider the uncontrolled constellation as a viable concept for this mission. Understand that the amount of data collected and the UML of these results will also be slightly reduced by the one to two orbits due to the time required to confirm control of the satellite from the ground station shortly after launch vehicle jettison. With a UML of 87 orbits, the mission would last less than six days. Even though this is five times longer than the other maximum point noted, the quality of the data collected and the data coverage must be considered before selecting an ideal point.

As the Inclination increases for all cases, the UML will tend to increase. Importantly, while this may allow more data collection opportunities, the data coverage will be limited as the array spacing is not ideal. As the orbital element offsets become too large, the spacing between satellite constituents while over the targets of interest become too large for array processing for most of the data collection opportunities. Although the large offsets can collect small amounts of data each orbit, these data points are far sparser as compared to more ideal configurations. High quality data collection passes are considered to be long continuous lines of data collection. Additionally, when there are crossover points in the data collection lines, the quality also increases as the results of one pass can be directly compared to a second pass of data over the same point but with a different trajectory. To compare the quality of data collected, as well as overall coverage, Figure 5.2 is presented. Using the two maximum points in Figure 5.1b that are discussed above, the configurations were propagated for their respective UML to visually compare data collection points.

For the ground track plots of Figure 5.2, the pink markers indicate the target areas for data collection over Antarctica and Greenland (see Subsection 4.3.2 for details), light green points in this figure represent data collection points within the Greenland target area, and the light blue

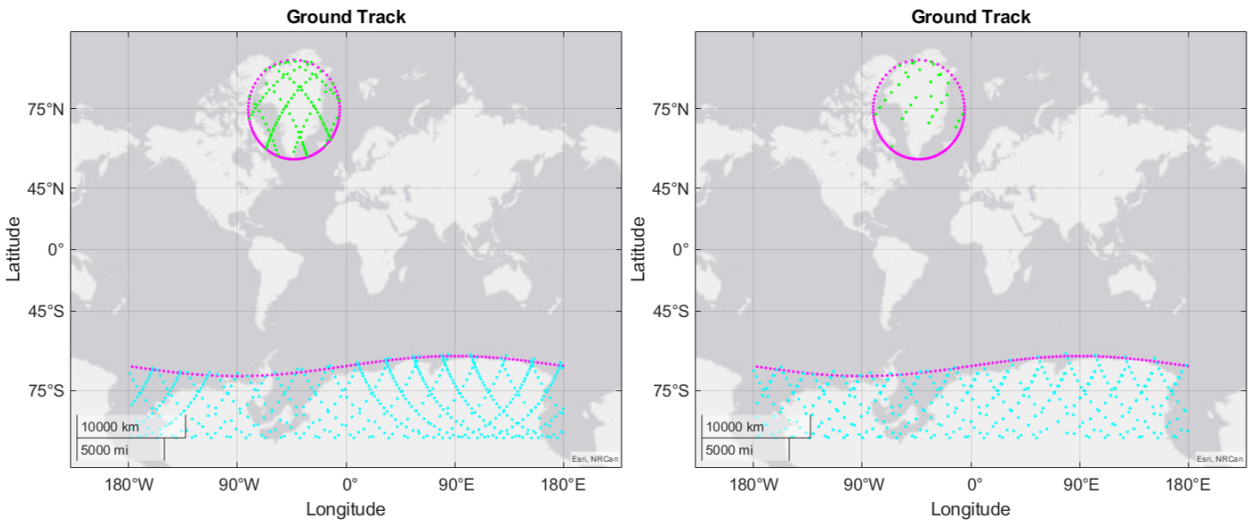

(a) Inclination Offset of 3.7e-6 radians and Right Ascension Offset of 1.1e-6 radians over 20 orbits

(b) Inclination Offset of 1.0e-5 radians and Right Ascension Offset of 1.1e-6 radians over 90 orbits

Figure 5.2: Data Coverage Comparison for Broad Sweep of Constellation Configurations

points indicate data collection points within the Antarctic target area. As indicated in the captions, Figure 5.2a is only propagated for 20 orbits while Figure 5.2b is propagated for 90 orbits. These limits are set by the results found in Figure 5.1.

In Figure 5.2a there are long lines of continuous data collection over both Antarctica and Greenland. This is the desired behavior of the ideal constellation configuration. Conversely, Figure 5.2b has much sparser coverage and typically only collects data for a few points in the middle of a target flyover, which is especially apparent for the Greenland data points. As the constellation contracts and the elements rotate position around the center satellite, per the equations of motion, some data collection can occur for short periods as the array spacing criterion is satisfied. This type of motion is expected for the ideal configuration as well, but the ideal configuration will contract and expand (in cross-track) at a more acceptable rate thereby allowing for more high quality data collection passes. Notably, the data collection shown in Figure 5.2a will collect lines of data that intersect at nearly perpendicular trajectories which is highly desirable when collecting ice thickness data. The ideal configuration is selected such that array spacing is satisfied as long as possible while over the targets, hence the results shown in Figure 5.2a are considered more ideal. This maximum

point is a good choice for the ideal configuration, but further investigation is required.

As mentioned previously, each combination of the offsets given in Table 5.1 are also simulated to find an ideal constellation configuration, but due to the interesting nature of four dimensional design spaces, it is hard to visually represent this data. It was found that the ideal configuration from this initial broad sweep is represented on the plots shown in Figure 5.1. However, other combinations did yield results worth investigating further. The combinations of interest utilize offsets from Inclination, Right Ascension, and True Anomaly.

The ideal configuration for this first set of simulations occurs with an offset in Inclination of 3.722e-6 radians and an offset in Right Ascension of 1.125e-6 radians. In this configuration, the UML is 20.1 orbits (one day and seven hours) before collision. In that time, the constellation was able to collect a total of 109,300 line-km of data over both the Antarctic and Greenland ice sheets.

While this point is described as the "ideal point", the UML is too low to suggest that this will be a successful mission. Higher UML solutions do not stay within the necessary offsets and therefore only collect sparse datasets. It is also understood that although there may be a slight increase in UML, the uncontrolled constellation is not viable as the operational time is well below a reasonable threshold (at least 120 orbits), and excessive collision risk at the end of the UML would almost certainly lead to space debris concerns. However, finding a configuration that can collect a large amount of high quality data sets is relevant to the recommended follow-on studies of the propulsed mission concept.

Based on the results given in this section, the ideal configuration will be near to the 20 orbit maximum point rather than the 87 orbit maximum point as the 20 orbit solution was shown to have the best chance of collecting large sets of high quality data. In order to select an ideal configuration, the areas around the 20 orbit solution are investigated using a finer resolution sweep. As the UML of the ideal configuration is not expected to exceed 30 orbits, based on the results of this section, the number of orbits propagated in the narrow sweep of configurations will be reduced to reduce computation time. It is also worth focusing on only three orbital variables at a time rather than the more computationally intensive four variable simulations.

5.1.2 Narrow Sweep

Results for the broad sweep presented in Subsection 5.1.1 indicate that the orbital element offsets that will yield an ideal constellation configuration are Inclination, Right Ascension, and True Anomaly. Thus the solution sweep for the finer resolution analysis around the ideal point will only include these three orbital elements. The combination of these three orbital elements were selected as they are the likely candidates for improving the data collection and lifespan of the uncontrolled constellation.

The offsets in Argument of Perigee, Inclination, and Right Ascension used for this simulation are given in Table 5.2. Note that the Inclination range is smaller while the ranges for Right Ascension and True Anomaly stayed the same. The number of points in each range were increased to analyze finer step sizes to find the best point possible.

Table 5.2: Orbital Element Offset Ranges for Results in Figure 5.3

Orbital Element	Inclination (i)	Arg. of Perigee (w)	Right Ascen. (Ω)	True Anomaly (ν)
Min Offset (rad.)	1.0E-06	0.0E+00	0.0E+00	0.0E+00
Max Offset (rad.)	1.5E-05	0.0E+00	1.0E-06	2.0E-07
# of Points	20	1	10	10

Presented in Figure 5.3 are the results of offsets in Right Ascension and True Anomaly combined with offsets in Inclination. Note that these results represent a 30 orbit propagation as compared to the previous section which propagated 120 orbits for each configuration. For these simulations, the UML for large Inclination offsets was set by the last data collection opportunity, not by collision risk which would occur after more propagation time. This is shown visually by bright yellow area of the far right plots of Figure 5.3 as the minimum offset is larger than 0.3 m indicating that failure by collision was not registered.

With a narrowed range of Inclination offsets, the same trends appear as in the previous subsection results. As in the previous section, the maximum data collection point (along an Inclination offset of 3.7e-6 radians in Figure 5.3b) does not coincide with the maximum UML. The previous section showed that the larger Inclination offsets lead to larger UML solutions but the data collected is

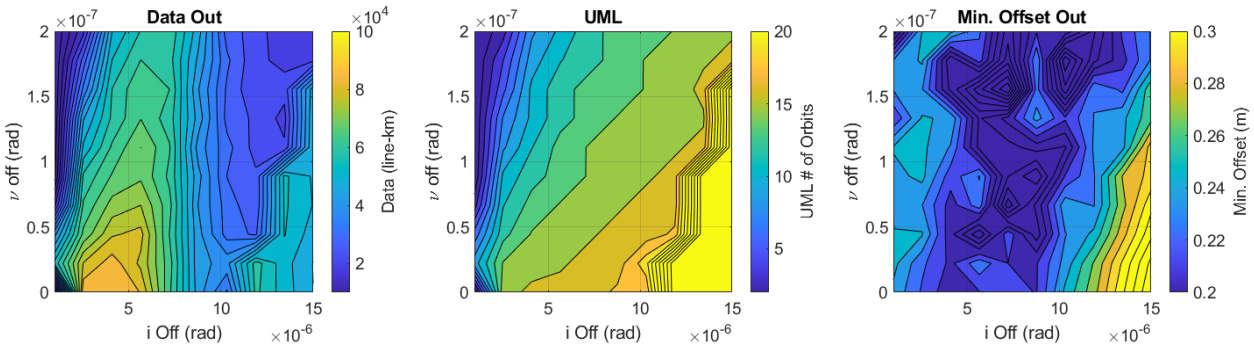

(a) Inclination with True Anomaly

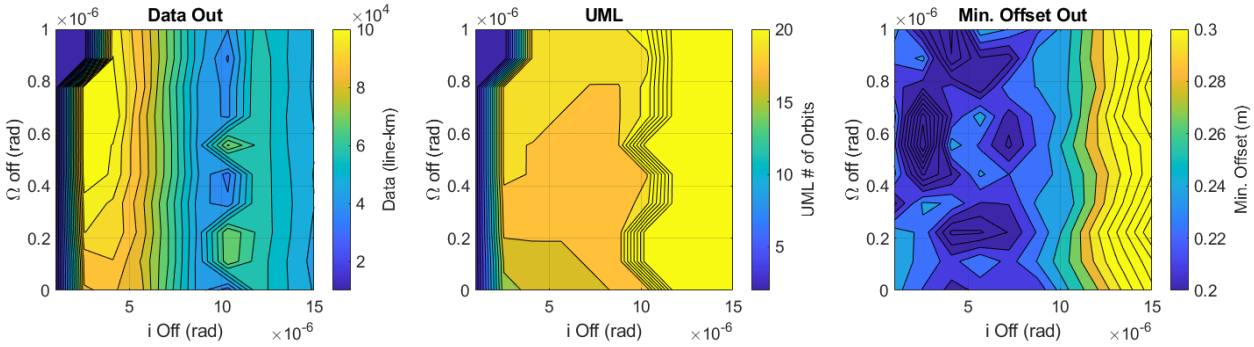

(b) Inclination with Right Ascension

Figure 5.3: Data Collected, UML, and Minimum Offset of Narrow Sweep

much sparser as array spacing was only satisfied for short time periods while over the targets. It is clear from this smaller subset that the point found in the previous subsection is near to the ideal. In analyzing the combinations of all three orbital elements, there is a point that increases data collection even further with no reduction to UML. This point will be taken as the ideal configuration point moving forward. The ideal orbital offsets for this point are given in Table 5.3.

Table 5.3: Constellation Orbital Element Offsets from Driving Orbit in Table 3.1

Orbital Element	Inclination (i)	Arg. of Perigee (w)	Right Ascen. (Ω)	True Anomaly (ν)
Ideal Offset (rad.)	2.556E-06	0	1.000E-06	2.222E-08

With the ideal offsets given in Table 5.3, the constellation would collect 121,500 line-km of data within 21.6 orbits before excessive collision risk would cause a failure. As noted above, 21.6 orbits is too short of a UML to consider the uncontrolled constellation as a viable option for the mission defined. Recall, that a short one to two orbit time interval after jettison is required to establish connection with all satellites in the constellation and move on to the Nominal operation

mode. Although the ideal configuration would collect a staggering amount of data in a short time period, the excessive collision risk after 20 orbits would certainly lead to mission failure. In the case that satellites do collide, space debris would certainly be created, which is an unacceptable outcome to the mission.

Selecting the ideal configuration is driven by longevity of an uncontrolled mission, but the final result presented here should indicate a configuration that is able to consistently collect large amounts of high quality data. It is clear that an uncontrolled constellation does not have the desired longevity. Even so, this result contributes a set of ideal orbital elements which can be used by a controlled constellation. Given the margins placed on the spacecraft designs, it could be possible to include a position control system (e.g. propulsion) that could have more than enough time after jettison to correct and maintain the orbital elements of the constellation. To better understand the effects of jettison and deviations from the ideal configuration, a Monte Carlo study was done and is presented in the following section.

5.2 Jettison Analysis

Understanding the effects of deviation from the ideal constellation configuration is of great interest in this project. Jettison is the major contributor of error for uncontrolled constellations, and it is necessary to evaluate how errors in this process will effect mission success. As the constellation defined cannot do controlled maneuvers to maintain or adjust relative position, the jettison process must be highly accurate to place the satellites into the ideal configuration. Although the previous analysis suggests that an uncontrolled constellation will not result in a meaningful lifespan for this mission, if the elements are inserted into the ideal configuration, there is enough time to perform maneuvers with a propulsion system before the collision risk becomes excessive. Thus the jettison analysis can still provide insight for this mission type regardless whether it is controlled or uncontrolled. For a controlled constellation, the results presented in this section indicate the accuracy required to form the ideal constellation configuration for significant time intervals.

Analysis of the jettison (or orbit injection) phase of the mission looks specifically at how errors

in initial position and velocity affect the mission lifetime. For this analysis, it is assumed that the launch vehicle is re-ignitable and maneuverable. Note this flexibility with the launch vehicle would require this mission to be the primary payload on that launch. The typical jettison velocity, relative to the launch vehicle, is assumed to be 2 m/s based on nanosatellite deployers like PPOD[49]. It is known that each of the eight satellites must be jettisoned individually with a wait time between to move the launch vehicle and jettison the next satellite. However, the timing is not considered in this analysis as it would cost more computational time without providing clearer detail on the accuracy required to achieve the ideal constellation configuration.

To analyze the effects of deviation from the ideal configuration, a Monte Carlo study was conducted. In this study a range of position and velocity errors are investigated to understand how deviation affects mission success. For each point of position and velocity error, a sphere of error is generated. A 2-D representation of this sphere is shown in Figure 5.4. In this image the large blue circle around each satellite represents the range of deviation defined by the error value investigated. The red circle indicates the ideal point for the satellite as defined by the ideal configuration from the previous section. A random deviation is applied for each satellite, as indicated by the yellow circle. Although only four satellites are represented in Figure 5.4, the full constellation that is simulated includes eight satellites. After the deviation is applied, the constellation of eight satellites are propagated forward for the Monte Carlo study. Note that this random deviation is three dimensional. An error sphere is generated for deviations in both position and velocity. Using the same metrics as the previous study in this chapter (data collected, UML, and collision risk) each error combination is inspected. To capture the random nature of the deviation, multiple runs are done for each point.

As with the previous study, it is relevant to start with a broad sweep. For the first result, a range of position errors up to 0.5 m and a range of velocity accuracy up to 0.025 m/s was used. These ranges were selected based on previous broader sweeps done by the author. For each range, there are 15 points. Each combination is ran five times resulting in a total of 375 simulations. Each run propagated forward two orbits as this is the most likely time period for collision risk. Two

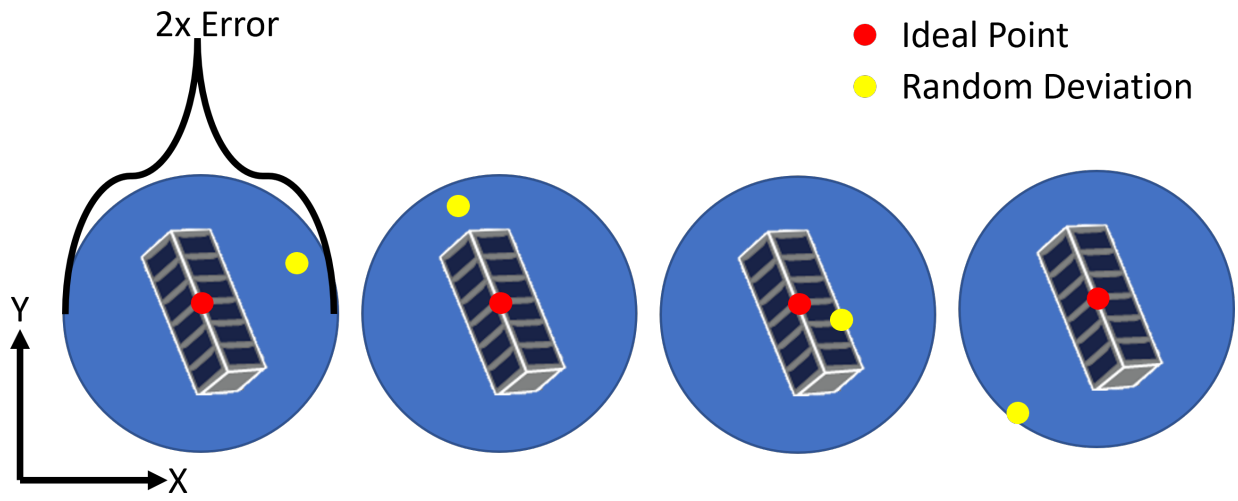

Figure 5.4: 2-D Representation of Random Error Sphere for Monte Carlo Analysis

orbits is also relevant, as noted in the previous section, because that is the expected amount of time after jettison needed to move the satellites into the Nominal operational mode. UML and collision failures are the most relevant metrics to assess the probability of success in jettisoning the satellites directly into the ideal configuration. Data collection will also be noted as this indicates how well the constellation formed the ideal configuration. All of the results presented also relate to effects of deviation on the propulsed mission concept when the satellites would maneuver into the ideal configuration. Results of the first Monte Carlo error simulations are given in Figure 5.5.

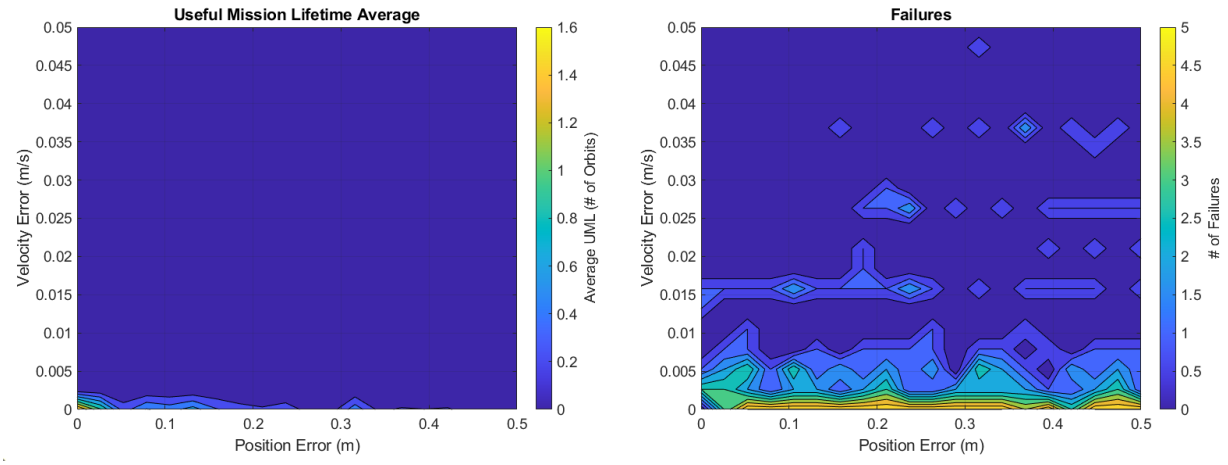

(a) UML

(b) Collision Failures

Figure 5.5: Broad Monte Carlo Analysis Results

Figure 5.5a is a plot of the UML when the error of position and velocity are varied. UML in this case is the average of all runs done for each point. It is clear from this result that the first simulations are still too broad, especially for velocity. Also note the features on the UML plot may not be to scale because the step sizes are too large. It was expected that some of the simulated constellations would work for a short period of time, but the errors are too large. At the origin of Figure 5.5a, the UML is noted as 1.6 orbits which is less than the two orbits propagated. This is because the last data collection point occurred at 1.6 orbits for this simulation interval. The 1.6 orbits indicated here does not represent the total lifetime of the ideal configuration, but rather it highlights how UML is calculated. The ideal configuration with no errors is not at risk of collision over this short time interval, as indicated by the zero failures registered at the origin in Figure 5.5b, rather this configuration would last 21.6 orbits before the risk of collision as indicated by the results of the previous section.

None of the simulated points with some velocity error were successful in collecting data; however, there were also very few collision failures when the velocity error is large, as shown in Figure 5.5b. This indicates that the satellites are drifting apart too quickly to have the chance to form the proper configuration. However, there still remains substantial collision risk throughout the solution domain. These plots suggest that velocity errors may be more adversely influential than position error. When there is some position error but no velocity error, the average UML could be as great as 0.6 orbits. As the position error decreases, the UML increases which does lead to increases in data collection, up to an average of 8,000 line-km when position error is 0.026 m. For reference, the origin point is able to collect 12,700 line-km of data. However, any amount of position error will cause substantial collision risk as indicated by the failures along the x-axis of Figure 5.5b. Interestingly, three failures occur at a position error of 0.026 m and zero velocity error compared to the five failures registered by almost all other points along the x-axis. To better understand the effects of deviations in position and velocity, a narrower range of error values was investigated.

The narrower jettison analysis focuses on values closer to the origin. The range of velocity error

was reduced to 0.01 m/s and the range of position error was reduced to 0.1 m. For each point, five runs were done. The results of this narrow simulation are shown in Figure 5.6.

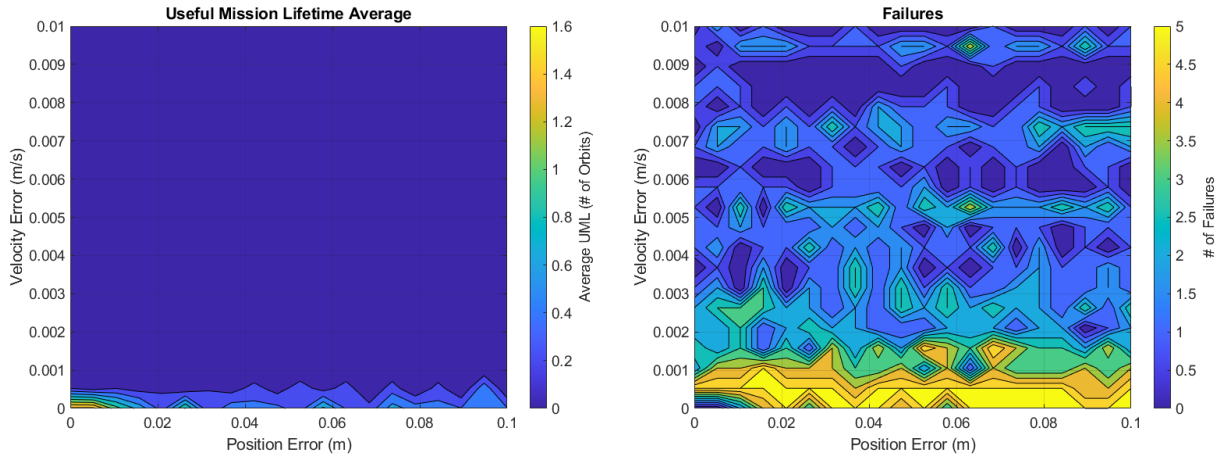

(a) UML (b) Collision Failures

Figure 5.6: Narrow Monte Carlo Analysis Results

It is apparent from Figure 5.6b that the probability of collision is substantial, even for these small errors. Similar to the broader sweep, any amount of velocity error causes the UML to be zero indicating the constellation drifts apart too quickly yet there also remains substantial collision risk. Interestingly, when the velocity error is zero and position error is 0.005 m, there are no failures and the constellation is able to collect the same amount of data as the origin point. However, the clear risk of collision indicates that jettisoning satellites directly into the ideal configuration is not recommended. As it pertains to the propulsed concept, these results indicate that orbital maneuvers must be incredibly accurate to properly form the ideal configuration.

From the above results, it is clear that the jettison accuracy required to successfully achieve an ideal constellation configuration is on the order of millimeter accuracy in position and sub-millimeter/second accuracy in velocity. Although the orbit injection accuracies achieved by flown nanosatellites are unknown, it is expected that the deviations are much greater than what is required for achieving the ideal constellation. Even if this level of accuracy is achievable, jettison of the satellites directly into the ideal configuration should not be considered as any small deviation leads to a high probability of collision. Without jettison directly into the ideal configuration, the

uncontrolled constellation cannot be considered a viable option for this mission concept. Using common nanosatellite jettison practices (satellites dispensed into the same orbital plane with significant wait times between), the propulsed mission could maneuver into the ideal configuration after the jettison phase. Even so, the accuracy required for these maneuvers (as indicated by the results of this section) is a substantial engineering challenge to overcome and would require additional hardware considerations.

The Monte Carlo studies presented in this section highlighted the order of accuracy required to achieve the ideal configuration. If the error of position and velocity during orbit injection is sub-millimeter, it may be possible to achieve the ideal constellation configuration; however, given the results from the previous section, even if the ideal configuration could be achieved, the resultant UML is only on the order of 20 orbits. This level of accuracy required to achieve the ideal configuration is not possible with current orbit injection techniques and as such it is not viable to jettison the satellites directly into the ideal configuration, especially if they are uncontrolled. Rather, it would be recommended to investigate potential success for a propulsed mission concept. The propulsed mission should jettison satellites in a more traditional way (with along-track separation on the same orbit plane), maneuver into the ideal configuration, and then maintain this configuration with the propulsion system. The propulsed concept still requires that the maneuvers be at the accuracy discussed above but a propulsion system could mitigate some of the collision risk. Follow-on research for such a controlled constellation concept should build up on the conclusions of this work.

5.3 Constellation Conclusions

Investigated in this chapter were the vehicle dynamics of an uncontrolled constellation of nanosatellites. The first investigation of the chapter aimed to find an ideal constellation configuration which minimized collision risk while maximizing UML and the data collected. Once selected, the ideal configuration was investigated further in the second part of this chapter to determine how errors in the jettison process would affect mission success. In both investigations, it was found that the

uncontrolled constellation would not be well suited for the mission of radar ice depth sounding.

In searching for the ideal constellation configuration, four independent variables were selected. These variables are satellite orbital elements offsets, specifically: Argument of Perigee, Inclination, Right Ascension, and True Anomaly. It was shown that Inclination offsets gave the most desirable configurations. The initial results showed that offsets in Argument of Perigee would not benefit the configuration, therefore the next set of simulations only considered offsets in Inclination, Right Ascension, and True Anomaly. Final results of this section indicated that small offsets in Inclination, Right Ascension, and True Anomaly between satellites form the ideal constellation configuration. The ideal offsets are given in Table 5.3. The ideal configuration of the uncontrolled constellation would be able to collect over 120,000 line-km of data with a UML of 21.6 orbits before excessive collision risk would lead to mission end. This configuration gave the best quality data collection points and achieved significant coverage in a short amount of time. Although this is a substantial amount of data, the UML is far too short to conduct a cost effective uncontrolled constellation mission. With this UML being set by excessive collision risk, the likely collision would create space debris, which is an unacceptable outcome of this mission. It is also worth noting that, although there is a substantial amount of data collected, only a small subset of the sounding data will be used to build the respective bed maps due to the inherent difficulty of detecting the ice-bedrock interface especially along the ice sheet margins. Still, this result is of great interest when considering a controlled mission concept as the satellites would have a significant amount of time to do station-keeping maneuvers required to maintain the ideal configuration and mitigate collision risk. With this in mind, it was useful to further investigate this ideal configuration to determine the acceptable level of errors in the initial configuration through a jettison analysis of the uncontrolled constellation. As it may take two orbits after jettison to gain operational control of the satellites, the error analysis assesses the viability of jettisoning directly into the ideal configuration.

The final investigation of this chapter utilized a Monte Carlo study to determine the required level of jettison accuracy for the ideal constellation configuration. By varying the amount of position and velocity error at the instant of orbit injection, the orbits of each satellite were propagated forward a

short time interval to understand the effects related to the metrics of collision risk, data collected, and UML. It was shown that collision risk quickly increases with any amount of position error. Velocity error had a major affect on the ability to form the constellation at all as constituents would quickly drift apart. The result of the investigation was that sub-millimeter accuracy was required for both position and velocity. Though there is no public information on jettison accuracy, it is expected that this level of accuracy is unachievable by modern launch vehicles. This result suggests that satellites should not be jettisoned directly into the ideal configuration. Once again, these results demonstrate that an uncontrolled constellation is not viable for this mission concept. These results also have implications for controlled mission planning as well.

Based on the error analysis done, if the vehicles are equipped with propulsion systems, the satellites should be jettisoned with substantial waiting time and relative spacing between constituents. After control of each satellite is confirmed, a maneuver would be done to enter the ideal configuration. The error analysis highlights that the maneuver into the ideal configuration must be highly accurate to reduce the chance of collision and ensure high quality data collection opportunities. For the controlled satellites, a technique must be implemented to properly measure the inter-satellite spacing and use this information in a control loop to correctly position the satellites into the ideal configuration. Without the addition of a propulsion system and a sufficiently accurate inter-satellite ranging system, the mission concept would likely not be successful.

These investigations proved that an uncontrolled constellation for radar ice depth sounding is not viable. The results found in the first section indicate that the ideal configuration, with no deviations in position or velocity, would only be able to operate for just over a day before collision between satellites is imminent. Jettison analysis indicates that even with sub-millimeter accuracy in position and velocity, the uncontrolled constellation would have excessive collision risk within the first two orbits.

Even with the disheartening results found in this chapter, a silver lining remains. If the same set of satellites implemented a propulsion system or other station-keeping technologies, the mission has a higher likelihood of success, though more analysis is certainly required. With a propulsion

system, jettison accuracy is still of interest but no longer becomes the major error source. However, the jettison analysis highlights that a more traditional jettison scheme should be considered as it is not suggested to jettison directly into the ideal configuration. Rather, subsequent optimization should search for an ideal point at which collision risk is minimized during all phases of the mission while also minimizing the delta-V required to achieve and maintain the ideal configuration. In achieving the ideal configuration, the controlled system must have a highly accurate method of inter-satellite ranging as indicated by the jettison analysis. With the presented satellite designs of Chapter 3, a propulsion system capable of 20 meters/second of delta-V could fit with the hardware sets defined. However, to also include a system for inter-satellite ranging would likely be outside the capacity of a 3U frame. By changing the 3U satellite frames to 6U frames, the increase in volume would certainly be well suited for any type of nanosatellite propulsion system as well as a system for accurate inter-satellite ranging.

Chapter 6

Conclusions and Recommendations

Actions need to be taken in the near future in the effort to combat climate change. One action of interest in this document is the consistent and repeatable collection of ice thickness data across polar regions. To date, ice sheet thickness and the bedrock topography below the ice sheet has been measured by airborne methods. However, the limitations of current methods have led to limited thickness datasets from a single platform over a short period of time. Over the past 20 years over 414,000 line-km of ice sounding radar data was collected over the Greenland ice sheets to form the high fidelity Greenland bed map[16]. Although this is a substantial amount of data, the disparate systems used and the large temporal baselines lead to errors in the interpolation of this data. To further extend the impact of ice sounding radar campaigns, new frontiers should be investigated. Naturally, the next frontier is ice sounding radars in space.

Several researchers have proposed mission concepts that would put an ice sounding radar on spacecraft to measure ice sheet thickness. All proposals that have been published, to date, have not assessed the vehicle but rather focused on the radar operations. Work done in this document contributes to this knowledge base by building upon proposed orbital ice sounding radar concepts by fully designing a mission architecture and performing the proper analysis of the vehicle dynamics. A driving design requirement of this report was to limit complexity, cost, and development time. This was the primary impetus to examine an uncontrolled constellation of nanosatellites for radar ice depth sounding with a focus on COTS hardware. The decision to analyze an uncontrolled constellation came from the understanding that propulsion systems for nanosatellites are not commercially available, and propulsion systems would greatly increase the cost and likely double development time of this mission concept from five years to 10 years.

Uncontrolled constellations are also of interest as they are not discussed in literature, at least in the context of proximity operations. The following section outlines all of the contributions and conclusions of this unique study.

6.1 Conclusions

Work in this report was done to assess the feasibility of an uncontrolled constellation of nanosatellites for radar ice depth sounding. In conducting this assessment, several unique contributions were made. These contributions are briefly summarized in the list below and discussed within this section.

- An adaptable satellite and mission design architecture for orbital radar ice depth sounding.
- A set of orbit propagation validation tables.
- The ideal constellation configuration, in terms of orbital elements, for radar ice depth sounding of the Antarctic and Greenland ice sheets.
- An error analysis to understand how jettison accuracy will affect mission success.

The first contribution of this works comes from the detailed mission design presented in Chapter 3. Firstly, a proper link budget was done for the defined radar operating parameters to verify that the detection of the faint signals from the ice-bedrock interface below the ice sheets is possible. The link budget was done in a conservative manner such that an SNR of 3 dB could certainly be achieved even if the operating parameters must be changed to better suit the mission type. With a successful link budget established, a mission architecture was thoroughly defined for supporting the radar payload. The mission requirements, satellite designs, and mission analysis detailed in this chapter are a unique contribution of this work. Not only does this mission architecture bring new understanding to the objective of orbital ice depth sounding, the architecture can be easily adapted to fit any nanosatellite mission design. The mission analysis methods used portray techniques that should be utilized by any satellite design.

After properly defining the architecture for this mission, a set of orbit propagation tools were developed in Chapter 4. The techniques used in this section are common in the orbital mechanics community. However, there is an apparent lack of validation data sets to verify the propagation techniques used. In this report, validation of the orbit propagation toolset utilized previous course-work, textbook examples, and industry standard computer programs. After successfully validating the implementation of the propagation methods, a data set of orbit propagation states was provided in this report for future researchers to verify their own propagation methods. Two data sets are given (2-Body only, and J2+Drag) in Appendix C so that users can incrementally validate their own code. This is another unique contribution of this work as no other validation data sets were readily available in the literature reviewed. Additionally, a github repository of the Matlab code used for this report was published as another reference for future researchers[70].

With the mission analysis complete and the propagation methods verified, it was confirmed that a single satellite was capable of maintaining control for this mission. The key contribution of this work came from the assessment of the uncontrolled multi-satellite mission defined. Using the developed orbit propagator, an assessment of the constellation was presented in Chapter 5. This chapter did broad sweeps of orbital element offsets between satellites to define the ideal constellation configuration for this mission type. It was found that although the constellation would collect over 100,000 line-km of depth sounding data over Antarctica and Greenland, the excessive risk of collision after 20 orbits would end the mission. Thus, it was found that the uncontrolled constellation was not well suited to conduct this mission type. However, the ideal configuration that was found should be used in future development of a controlled concept. The configuration itself and the analysis to support the above conclusion is a unique contribution of this work. This configuration was then used to understand how deviations in jettison position and velocity would affect mission success.

In an effort to understand the orbital injection phase of the uncontrolled constellation, a Monte Carlo study on jettison error was completed. This study showed that any amount of deviation from the ideal configuration would have detrimental impacts on mission success. The accuracy required

for the uncontrolled constellation to be jettisoned into the ideal configuration was sub-millimeter, which is beyond the capability of modern launch vehicles. As such, this result reinforced the previous conclusion that the uncontrolled constellation was not viable for this mission type. Additionally, this study shows that satellites should not be jettisoned directly into the ideal constellation configuration due to excessive collision risk in the first two orbits from any small deviations. However, this analysis also gives insight to the accuracy required for a controlled mission concept. In the case of controlled satellites, the error analysis highlighted that maneuvers must be similarly accurate to mitigate the chance of collision. To achieve this accuracy will require methods of accurately measuring the relative satellite positions. This inter-satellite ranging requirement necessitates additional hardware for the controlled mission concept. Follow-on studies are needed to understand the delta-V requirements for a propulsed concept to achieve and maintain the ideal configuration while minimizing collision risk. All of the analysis done in this error study serves as another set of unique contributions of this work.

Although the results given in this report may be contrary to the initial hypothesis, they represent a unique contribution to the field. No other published works have performed the necessary constellation assessment for the orbital ice sounding mission concept. This report focuses on the assessment of an uncontrolled constellation of satellites operating in near proximity, which is another unique contribution of this work. The knowledge gained from this study indicates that mission success is unlikely for uncontrolled constellations operating in proximity as the collision risk will be far too high without increasing the relative spacing beyond useful ranges for synthesizing an antenna array. However, the analysis done in this report supports the development of a controlled mission of the same type. It is indicated in this report that the individual vehicles are able to meet the mission requirements, but that collision risk of the uncontrolled constellation is too high to move forward with development. In summary, a COTS solution is not currently viable for the ice sounding mission. The concepts detailed in this work, suggesting the need for a controlled vehicle concept that also includes an inter-satellite ranging system, should be expanded upon by other researchers to properly adapt and analyze the mission architecture presented in the pursuit of

understanding and combating climate change.

6.2 Recommendations

Given the conclusions detailed in the previous section, it has been shown that the uncontrolled constellation for radar ice depth sounding should not be pursued further. However, the concepts and designs presented in this work could easily be adapted for a controlled mission concept. It is recommended that the investigation of a controlled concept be executed.

Future work should investigate nanosatellite control techniques within the context of this mission type. Traditional propulsion systems are an obvious starting point. Using the results from this report, a study should be done to understand the propulsion requirements, to include delta-V requirements and control methodology. By understanding what is required to maintain control of each satellite, the vehicle designs presented in this report can be adapted to better suit the mission.

Apart from investigating traditional propulsion techniques, it would be useful to explore techniques such as differential drag. This would require a higher fidelity method of estimating disturbance torques while on orbit and modeling their effects on the spacecraft. By using quaternions to represent the satellite state, the attitude control of the satellites can be modeled and properly evaluated. With the proper modeling, differential drag techniques can be analyzed to further control the positioning of the satellites and reduce the delta-V requirements of the propulsion system.

With increased knowledge of the ability to maintain position control of the satellites needed for this mission, the constellation studies done in this report can be extended. The constellation configuration selected in this report is noted as an ideal point rather than an optimum point. As such, a formal optimization should be done on the constellation configuration. In doing so, there should be a feedback loop to the error analysis presented as it is unknown if different configurations have different tolerances to deviation from the ideal configuration.

Concurrently, an orbital clutter simulator should be developed to discern the geographic conditions that are best suited for orbital ice depth sounding. The designs presented in this document are best suited for inland, slow-moving ice sheets where the bed topography is relatively flat. Towards

the ice sheet margins, it is expected that performance will degrade. A properly developed clutter simulator would investigate how different interface geometries and ice sheet conditions affect mission success. This is highly relevant to deducing the true quantity and quality of the data that could be collected by an orbital ice depth sounding mission.

Lastly, the previous MVDR study done by this author should be extended to better understand the effects of non-ideal array spacing. This report relied upon the array spacing conclusion given in that study, but it is believed that MVDR would be able to handle larger cross-track offsets between antenna elements. By extending this MVDR study, the allowable array spacing will be better understood. It may be found that a larger cross-track offset is acceptable which would relate to larger orbital offsets thereby reducing collision risk and could potentially eliminate the need for an inter-satellite tracking system. Properly understanding the upper bounds of MVDRs capabilities is necessary for future iterations of this mission design.

If the future work suggested above proves the feasibility of a controlled multi-satellite mission concept, the development of a radar system for orbital ice depth sounding should be pursued. This design and testing process could take longer than the construction and development of the related nanosatellite platforms. As such this should be pursued soon. The uncontrolled concept may not be feasible, but all of the mission design presented in this work can be built upon to realize a mission for orbital ice depth sounding. As presented, the design could be implemented within five years. With the necessary hardware changes, that timeline could easily double. But the sooner the work starts, the sooner data can be collected.

References

[1] IPCC, "IPCC Special Report on the Ocean and Cryosphere in a Changing Climate," *Intergovernmental Panel on Climate Change*, 2019.

[2] Intergovernmental Panel on Climate Change, *Climate Change 2013 – The Physical Science Basis: Working Group I Contribution to the Fifth Assessment Report of the Intergovernmental Panel on Climate Change*. Cambridge University Press, 2014.

[3] I. Joughin, I. M. Howat, M. Fahnestock, B. Smith, W. Krabill, R. B. Alley, H. Stern, and M. Truffer, "Continued evolution of jakobshavn isbrae following its rapid speedup," *Journal of Geophysical Research: Earth Surface*, vol. 113, no. F4, 2008.

[4] R. Thomas, E. Frederick, J. Li, W. Krabill, S. Manizade, J. Paden, J. Sonntag, R. Swift, and J. Yungel, "Accelerating ice loss from the fastest greenland and antarctic glaciers," *Geophysical Research Letters*, vol. 38, no. 10, 2011.

[5] J. T. Overpeck, B. L. Otto-Bliesner, G. H. Miller, D. R. Muhs, R. B. Alley, and J. T. Kiehl, "Paleoclimatic evidence for future ice-sheet instability and rapid sea-level rise," *Science*, vol. 311, no. 5768, pp. 1747–1750, 2006.

[6] E. Larour, J. Schiermeier, E. Rignot, H. Seroussi, M. Morlighem, and J. Paden, "Sensitivity analysis of pine island glacier ice flow using issm and dakota," *Journal of Geophysical Research: Earth Surface*, vol. 117, no. F2, 2012.

[7] F. Rodriguez-Morales, S. Gogineni, C. J. Leuschen, J. D. Paden, J. Li, C. C. Lewis, B. Panzer, D. Gomez-Garcia Alvestegui, A. Patel, K. Byers, R. Crowe, K. Player, R. D. Hale, E. J. Arnold, L. Smith, C. M. Gifford, D. Braaten, and C. Panton, "Advanced multifrequency radar

instrumentation for polar research," *IEEE Transactions on Geoscience and Remote Sensing*, vol. 52, no. 5, pp. 2824–2842, 2014.

[8] J. Li, J. Paden, C. Leuschen, F. Rodriguez-Morales, R. D. Hale, E. J. Arnold, R. Crowe, D. Gomez-Garcia, and P. Gogineni, "High-altitude radar measurements of ice thickness over the antarctic and greenland ice sheets as a part of operation icebridge," *IEEE Transactions on Geoscience and Remote Sensing*, vol. 51, no. 2, pp. 742–754, 2013.

[9] E. Rignot, J. Mouginot, C. Larsen, Y. Gim, and D. Kirchner, "Low-frequency radar sounding of temperate ice masses in southern alaska," *Geophysical Research Letters*, vol. 40, 10 2013.

[10] J. Mouginot, E. Rignot, Y. Gim, D. Kirchner, and E. L. Meur, "Low-frequency radar sounding of ice in east antarctica and southern greenland," *Annals of Glaciology*, vol. 55, no. 67, p. 138–146, 2014.

[11] M. E. Peters, D. D. Blankenship, and D. L. Morse, "Analysis techniques for coherent airborne radar sounding: Application to west antarctic ice streams," *Journal of Geophysical Research: Solid Earth*, vol. 110, no. B6, 2005.

[12] G. Durand, O. Gagliardini, L. Favier, T. Zwinger, and E. le Meur, "Impact of bedrock description on modeling ice sheet dynamics," *Geophysical Research Letters*, vol. 38, no. 20, 2011.

[13] E. M. Enderlin, I. M. Howat, and A. Vieli, "High sensitivity of tidewater outlet glacier dynamics to shape," *The Cryosphere*, vol. 7, no. 3, pp. 1007–1015, 2013.

[14] B. R. Parizek, K. Christianson, S. Anandakrishnan, R. B. Alley, R. T. Walker, R. A. Edwards, D. S. Wolfe, G. T. Bertini, S. K. Rinehart, R. A. Bindschadler, and S. M. J. Nowicki, "Dynamic (in)stability of thwaites glacier, west antarctica," *Journal of Geophysical Research: Earth Surface*, vol. 118, no. 2, pp. 638–655, 2013.

[15] J. Griggs and J. Bamber, "Antarctic ice-shelf thickness from satellite radar altimetry," *Journal of Glaciology*, vol. 57, no. 203, p. 485–498, 2011.

[16] J. L. Bamber, J. A. Griggs, R. T. W. L. Hurkmans, J. A. Dowdeswell, S. P. Gogineni, I. Howat, J. Mouginot, J. Paden, S. Palmer, E. Rignot, and D. Steinhage, "A new bed elevation dataset for greenland," *The Cryosphere*, vol. 7, no. 2, pp. 499–510, 2013.

[17] P. Fretwell, H. D. Pritchard, D. G. Vaughan, J. L. Bamber, N. E. Barrand, R. Bell, C. Bianchi, R. G. Bingham, D. D. Blankenship, G. Casassa, G. Catania, D. Callens, H. Conway, A. J. Cook, H. F. Corr, D. Damaske, V. Damm, F. Ferraccioli, R. Forsberg, S. Fujita, Y. Gim, P. Gogineni, J. A. Griggs, R. C. Hindmarsh, P. Holmlund, J. W. Holt, R. W. Jacobel, A. Jenkins, W. Jokat, T. Jordan, E. C. King, J. Kohler, W. Krabill, M. Riger-Kusk, K. A. Langley, G. Leitchenkov, C. Leuschen, B. P. Luyendyk, K. Matsuoka, J. Mouginot, F. O. Nitsche, Y. Nogi, O. A. Nost, S. V. Popov, E. Rignot, D. M. Rippin, A. Rivera, J. Roberts, N. Ross, M. J. Siegert, A. M. Smith, D. Steinhage, M. Studinger, B. Sun, B. K. Tinto, B. C. Welch, D. Wilson, D. A. Young, C. Xiangbin, and A. Zirizzotti, "Bedmap2: Improved ice bed, surface and thickness datasets for Antarctica," *Cryosphere*, vol. 7, no. 1, pp. 375–393, 2013.

[18] M. Morlighem, E. Rignot, H. Seroussi, E. Larour, H. Ben Dhia, and D. Aubry, "A mass conservation approach for mapping glacier ice thickness," *Geophysical Research Letters*, vol. 38, no. 19, 2011.

[19] M. Morlighem, E. Rignot, J. Mouginot, X. Wu, H. Seroussi, E. Larour, and J. Paden, "High-resolution bed topography mapping of russell glacier, greenland, inferred from operation icebridge data," *Journal of Glaciology*, vol. 59, no. 218, p. 1015–1023, 2013.

[20] M. Morlighem, E. Rignot, J. Mouginot, H. Seroussi, and E. Larour, "Deeply incised submarine glacial valleys beneath the Greenland ice sheet," *Nature Geoscience*, vol. 7, no. 6, pp. 418–422, 2014.

[21] J. N. Bassis, B. Berg, A. J. Crawford, and D. I. Benn, "Transition to marine ice cliff instability

controlled by ice thickness gradients and velocity," *Science*, vol. 372, no. 6548, pp. 1342–1344, 2021.

[22] R. M. DeConto and D. Pollard, "Contribution of Antarctica to past and future sea-level rise," *Nature*, vol. 531, no. 7596, pp. 591–597, 2016.

[23] R. M. DeConto, D. Pollard, R. B. Alley, I. Velicogna, E. Gasson, N. Gomez, S. Sadai, A. Condron, D. M. Gilford, E. L. Ashe, R. E. Kopp, D. Li, and A. Dutton, "The Paris Climate Agreement and future sea-level rise from Antarctica," *Nature*, vol. 593, no. 7857, pp. 83–89, 2021.

[24] Scientific Committee on Antarctic Research, "RINGS: Collaborative international effort to map all Antarctic ice-sheet margins." White Paper, 2020. https://www.scar.org/science/rings/home/.

[25] A. Aschwanden, M. A. Fahnestock, and M. Truffer, "Complex Greenland outlet glacier flow captured," *Nature Communications*, vol. 7, no. May 2015, pp. 1–8, 2016.

[26] J. L. Bamber, J. L. Gomez-Dans, and J. A. Griggs, "A new 1 km digital elevation model of the antarctic derived from combined satellite radar and laser data – part 1: Data and methods," *The Cryosphere*, vol. 3, no. 1, pp. 101–111, 2009.

[27] M. Morlighem, E. Rignot, T. Binder, D. Blankenship, R. Drews, G. Eagles, O. Eisen, F. Ferraccioli, R. Forsberg, P. Fretwell, V. Goel, J. S. Greenbaum, H. Gudmundsson, J. Guo, V. Helm, C. Hofstede, I. Howat, A. Humbert, W. Jokat, N. B. Karlsson, W. S. Lee, K. Matsuoka, R. Millan, J. Mouginot, J. Paden, F. Pattyn, J. Roberts, S. Rosier, A. Ruppel, H. Seroussi, E. C. Smith, D. Steinhage, B. Sun, M. R. den Broeke, T. D. Ommen, M. van Wessem, and D. A. Young, "Deep glacial troughs and stabilizing ridges unveiled beneath the margins of the Antarctic ice sheet," *Nature Geoscience*, vol. 13, no. 2, pp. 132–137, 2020.

[28] M. Morlighem, C. N. Williams, E. Rignot, L. An, J. E. Arndt, J. L. Bamber, G. Catania, N. Chauché, J. A. Dowdeswell, B. Dorschel, I. Fenty, K. Hogan, I. Howat, A. Hubbard,

M. Jakobsson, T. M. Jordan, K. K. Kjeldsen, R. Millan, L. Mayer, J. Mouginot, B. P. Noël, C. O'Cofaigh, S. Palmer, S. Rysgaard, H. Seroussi, M. J. Siegert, P. Slabon, F. Straneo, M. R. van den Broeke, W. Weinrebe, M. Wood, and K. B. Zinglersen, "BedMachine v3: Complete Bed Topography and Ocean Bathymetry Mapping of Greenland From Multibeam Echo Sounding Combined With Mass Conservation," *Geophysical Research Letters*, vol. 44, no. 21, pp. 11,051–11,061, 2017.

[29] W. A. Shiroma, L. K. Martin, J. M. Akagi, J. T. Akagi, B. L. Wolfe, B. A. Fewell, and A. T. Ohta, "CubeSats: A bright future for nanosatellites," *Central European Journal of Engineering*, vol. 1, no. 1, pp. 9–15, 2011.

[30] P. Gogineni, C. R. Simpson, J. B. Yan, C. R. O'Neill, R. Sood, S. Z. Gurbuz, and A. C. Gurbuz, "A cubesat train for radar sounding and imaging of antarctic ice sheet," vol. 2018-July, pp. 4138–4141, Institute of Electrical and Electronics Engineers Inc., 10 2018.

[31] S. J. Chung, S. Bandyopadhyay, R. Foust, G. P. Subramanian, and F. Y. Hadaegh, "Review of formation flying and constellation missions using nanosatellites," *Journal of Spacecraft and Rockets*, vol. 53, no. 3, pp. 567–578, 2016.

[32] K. Jezek, E. Rodríguez, P. Gogineni, A. Freeman, J. Curlander, X. Wu, J. Paden, C. Allen, C. . Jezek, E. Rodríguez, P. Gogineni, A. Freeman, J. Curlander, X. Wu, J. Paden, and C. Allen, "Glaciers and Ice Sheets Mapping Orbiter concept," *J. Geophys. Res*, vol. 111, pp. 6–20, 2006.

[33] J. Dall, H. F. Corr, N. Walker, B. Rommen, and C. C. Lin, "Sounding the Antarctic ice sheet from space: A feasibility study based on airborne P-band radar data," in *International Geoscience and Remote Sensing Symposium (IGARSS)*, vol. 2018-July, pp. 4142–4145, Institute of Electrical and Electronics Engineers Inc., oct 2018.

[34] U. Nixdorf, D. Steinhage, U. Meyer, L. Hempel, M. Jenett, P. Wachs, and H. Miller, "The

newly developed airborne radio-echo sounding system of the AWI as a glaciological tool," *Annals of Glaciology*, vol. 29, pp. 231–238, 1999.

[35] E. Arnold, C. Leuschen, F. Rodriguez-Morales, J. Li, J. Paden, R. Hale, and S. Keshmiri, "CReSIS airborne radars and platforms for ice and snow sounding," *Annals of Glaciology*, vol. 61, no. 81, pp. 58–67, 2020.

[36] C. C. Hernández, V. Krozer, J. Vidkjær, and J. Dall, "POLARIS: ESA's Airborne Ice Sounding Radar Front-End Design, Performance Assessment and First Results," *IEEE MTT-S International Microwave Symposium Digest*, no. May 2008, pp. 393–396, 2009.

[37] E. Arnold, F. Rodriguez-Morales, J. Paden, C. Leuschen, S. Keshmiri, S. Yan, M. Ewing, R. Hale, A. Mahmood, A. Blevins, A. Mishra, T. Karidi, B. Miller, and J. Sonntag, "HF/VHF radar sounding of ice from manned and unmanned airborne platforms," *Geosciences (Switzerland)*, vol. 8, no. 5, pp. 1–22, 2018.

[38] B. Miller, B. Randolph, J. Paden, and E. Arnold, "Effects of Known and Unknown Antenna Position Errors on MVDR," *IEEE International Symposium on Phased Array Systems and Technology*, vol. 2019-Octob, 2019.

[39] B. Miller, G. Ariho, J. Paden, and E. Arnold, "Multipass SAR Processing for Radar Depth Sounder Clutter Suppression, Tomographic Processing, and Displacement Measurements," *International Geoscience and Remote Sensing Symposium (IGARSS)*, pp. 822–825, 2020.

[40] C. Fish, C. Swenson, T. Neilsen, B. Bingham, J. Gunther, E. Stromberg, S. Burr, R. Burt, G. Crowley, I. Azeem, M. Pilinski, A. Barjatya, and J. Petersen, "DICE Mission Design, Development, and Implementation: Success and Challenges," *26th Annual AIAA/USU Conference on Small Satellites*, vol. 32114, pp. 801–594, 2012.

[41] A. T. Johnson, M. Shumko, and B. Griffith, "The FIREBIRD-II CubeSat mission: Focused investigations of relativistic electron burst intensity, range, and dynamics," *Review of Scientific Instruments*, 2020.

[42] N. A. Dallmann, J. G. Delapp, D. C. Enemark, T. D. Fairbanks, C. M. Fortgang, D. C. Guenther, S. L. Judd, G. M. Kestell, J. E. Lake, J. P. Martinez, K. P. Mccabe, J. M. Michel, J. M. Palmer, M. W. Powell, D. A. Prichard, M. C. Proicou, H. M. Quinn, R. S. Reid, E. B. Schaller, D. N. Seitz, P. S. Stein, S. A. Storms, E. A. Sullivan, J. L. Tripp, A. Warniment, and R. M. Wheat, "An Agile Space Paradigm and the Prometheus CubeSat System," *29th Annual AIAA/USU Conference on Small Satellites*, 2015.

[43] N. H. Roth, B. Risi, C. C. Grant, and R. E. Zee, "Flight results from the canx-4 and canx-5 formation flying mission," *4S Symposium*, pp. 1–15, 2016.

[44] S. Mauthe, F. Pranajaya, R. Zee, and U. of Toronto, "The design and test of a compact propulsion system for canx nanosatellite formation flying conference on small satellites," *19th Conference on Small Satellites*, p. 12, 2010.

[45] O. Ben-Yaacov and P. Gurfil, "Long-term cluster flight of multiple satellites using differential drag," *Journal of Guidance, Control, and Dynamics*, vol. 36, pp. 1731–1740, 2013.

[46] M. Zaberchik, D. R. Lev, E. Edlerman, and A. Kaidar, "Fabrication and testing of the cold gas propulsion system flight unit for the adelis-samson nano-satellites," *Aerospace*, vol. 6, 8 2019.

[47] Endurosat. Webpage, 2022. https://www.endurosat.com/.

[48] SpaceX, "Falcon 9 Launch Vehicle Payload User's Guide," p. 69, 2015.

[49] W. Lan, R. Munakata, R. Nugent, and D. Pignatelli, "Poly Picosatellite Orbital Deployer Mk III Rev. E User Guide," *California Polytechnic State University*, pp. 1–21, 2014.

[50] C. Wen, H. Zhang, and P. Gurfil, "Orbit injection considerations for cluster flight of nanosatellites," *Journal of Spacecraft and Rockets*, vol. 52, no. 1, pp. 196–208, 2015.

[51] Z. Yoon, Y. Lim, S. Grau, W. Frese, and M. A. Garcia, "Orbit deployment and drag control

strategy for formation flight while minimizing collision probability and drift," *CEAS Space Journal*, vol. 12, no. 3, pp. 397–410, 2020.

[52] R. Culberg and D. M. Schroeder, "Radar Scattering in Firn and its Implications for VHF/UHF Orbital Ice Sounding," *International Geoscience and Remote Sensing Symposium (IGARSS)*, pp. 4137–4140, 2019.

[53] Federal Communications Commision, *FCC Online Table of Frequency Allocations*, February 2021. https://transition.fcc.gov/oet/spectrum/table/fcctable.pdf.

[54] J. A. Macgregor, J. Li, J. D. Paden, G. A. Catania, G. D. Clow, M. A. Fahnestock, S. P. Gogineni, R. E. Grimm, M. Morlighem, S. Nandi, H. Seroussi, and D. E. Stillman, "Radar attenuation and temperature within the Greenland Ice Sheet," *Journal of Geophysical Research: Earth Surface*, vol. 120, no. 6, pp. 983–1008, 2015.

[55] M. Richards, J. Scheer, and W. Holm, *Principles of Modern Radar: Basic Principles*. SciTech Publishing, 2010.

[56] NASA, *CubeSat 101: Basic Concepts and Processes for First-Time CubeSat Developers*, 2017.

[57] The CubeSat Program, Cal Poly SLO, *CubeSat Design Specification*, 2020.

[58] W. Larson and J. Wertz, *Space Mission Analysis and Design*. Kluwer Academic Publishers, 1999.

[59] C. Brown, *Elements of Spacecraft Design*. AIAA, 2002.

[60] ISISpace. Webpage, 2021. https://www.isispace.nl/.

[61] AAC Clyde Space. Webpage, 2022. https://www.aac-clyde.space/.

[62] CubeSpace. Webpage, 2020. https://www.cubespace.co.za/.

[63] Novatel. Webpage, 2022. https://novatel.com/.

[64] Taoglas. Webpage, 2021. https://www.taoglas.com/.

[65] D. A. Vallado, *Fundamentals of astrodynamics and applications*, vol. 12. Springer Science & Business Media, 2001.

[66] E. Kreyszig, *Advanced Engineering Mathematics*. John Wiley & Sons, Inc., 10 ed., 2011.

[67] MATLAB, *version 9.9.0 (R2020b)*. Natick, Massachusetts: The MathWorks Inc., 2020.

[68] J. Picone, A. Hedin, D. P. Drob, and A. C. Aikin, "NRLMSISE-00 empirical model of the atmosphere: Statistical comparisons and scientific issues," 2002.

[69] STK, *version 12.2*. Exton, Pennsylvania: Ansys Government Initiatives, 2022.

[70] B. Miller, "Dissertation_Code," August 2022. https://github.com/gamer10bm/Dissertation_Code.

[71] Swedish Space Corporation. Webpage, 2018. https://sscspace.com/.

Appendix A

Satellite Hardware Tables

Table A.1: RX Satellite Hardware Breakdown

Component	Manufacturer	Cost ($)	Mass (g)	Size	Power (W)
Payload					
RX Radar	CReSIS	N/A	1500	[89, 95, 80]	15
VHF Antenna	ISISpace[60]	10000	89	[98, 98, 6]	N/A
Structure					
3U Frame	Endurosat[47]	3300	850	[100, 100, 340.5]	N/A
Communications					
UHF Antenna	Endurosat[47]	5000	85	[98, 98, 6.5]	N/A
UHF Transciever	Endurosat[47]	4600	90	[89, 95, 14]	1.4
X-Band Antenna	Endurosat[47]	7600	89	[98, 98, 6]	N/A
X-Band Transciever	Endurosat[47]	24100	270	[89, 95, 30]	2
Power					
Starbuck-Nano EPS	Clyde Space[61]	4000	88	[90, 96, 12.4]	N/A
40Whr CubeSat Battery	Clyde Space[61]	10000	351	[90, 96, 27.4]	1
1U Solar Panel (x2)	Endurosat[47]	2100	44	[82.6, 98, 2.2]	N/A
1.5U Solar Panel (x2)	Endurosat[47]	3100	65	[82.6, 154.7, 2.2]	N/A
3U Solar Panel	Endurosat[47]	5100	127	[82.6, 325, 2.2]	N/A
ADCS					
ADCS 3-Axis	CubeSpace[62]	37400	554	[90, 96, 75]	2.3
CD&H					
OBC	Endurosat[47]	6000	130	[89, 94, 19.5]	2.3
GNSS Reciever	Novatel[63]	N/A	31	[46, 71, 11]	1.8
GNSS Antenna	Taoglas[64]	Unknown	20	[35, 35, 6.9]	N/A

Table A.2: TX Satellite Hardware Breakdown

Component	Manufacturer	Cost ($)	Mass (g)	Size	Power (W)
Payload					
TX Radar	CReSIS	N/A	1800	[89, 95, 100]	115
VHF Antenna	ISISpace[60]	10000	89	[98, 98, 6]	N/A
Structure					
6U Frame	Endurosat[47]	12400	850	[100, 226.3, 366]	N/A
Communications					
UHF Antenna	Endurosat[47]	5000	85	[98, 98, 6.5]	N/A
UHF Transciever	Endurosat[47]	4600	90	[89, 95, 14]	1.4
X-Band Antenna	Endurosat[47]	7600	89	[98, 98, 6]	N/A
X-Band Transciever	Endurosat[47]	24100	270	[89, 95, 30]	2
Power					
EPS II + 80Whr Battery	Endurosat[47]	36500	1280	[89, 95, 80]	1
3U Solar Panel (x2)	Endurosat[47]	5100	127	[82.6, 325, 2.2]	N/A
6U Solar Panel	Endurosat[47]	12400	254	[165, 325, 2.2]	N/A
ADCS					
ADCS 3-Axis	CubeSpace[62]	37400	554	[90, 96, 75]	2.3
CD&H					
OBC	Endurosat[47]	6000	130	[89, 94, 19.5]	2.3
GNSS Reciever	Novatel[63]	N/A	31	[46, 71, 11]	1.8
GNSS Antenna	Taoglas[64]	Unknown	20	[35, 35, 6.9]	N/A

Appendix B

Constants and Symbols

Table B.1: Report Constants

Symbol	Value	Units	Description	Reference
$\dot{\theta}$	7.29211585530066E-05	rad/sec	rotation rate of Earth	[65]
R_{Earth}	6378.145	km	mean equatorial radius of Earth	[65]
V_A			relative velocity	
μ	398600.435	$\frac{km^3}{s^2}$	the standard gravitational parameter for Earth	
r			orbital radius	
$\hat{r}$			the unit vector in the direction of the satellite	
J_2	0.00108262668			[65]
C_D	1.28		coefficient of drag	
m			mass	
A			cross-sectional area	
r_0	298.145	km	the reference radius	
H	200	km	the scale height	
ρ_0	0.0004	$\frac{kg}{km^3}$	the reference density	

Appendix C

Orbit Propagator Validation Tables

Using the methods developed in Chapter 4, two sets of validation data were generated for use in verifying orbit propagator's to a high degree. The code developed for this project can be found at https://github.com/gamer10bm/Dissertation_Code and the script used to generate these data sets is Validate_Propagator_Table_Script[70]. Each propagated orbit is based on the orbit defined in Section 3.2.

The first validation set only includes contributions from 2-Body. The time values and position values are given in Table C.1. Ensure that the intial simulation point is exactly the same as the data given in the first row. Also, ensure that the constants of your propagator match those given in Appendix B. Lastly, the step size for time should also be the same. By propagating to 11518.37 seconds, the final row indicates the outputs of the propagator developed for this work. Some of the intermediate values are skipped for brevity.

The second validation set includes contributions from 2-Body, J2, and Drag. Use a mass of 3.33 kilograms, a drag coefficient of 1.28, and an area of .36 m^2. The drag model used is NRLMSISE-00 by way of the built-in function atmostnrlmsise00 in Matlab. The F10.7 81 day average was set to 78.71, the F10.7 of the previous day was set to 78, and the geomagnetic vector was set to [3 3 3 2 3 3 4]. The data values for this set are given in Table C.2. Please refer to Chapter 4 and the github repository above for more clarity on the propagator implementation.

Table C.1: Validation Data for 2-Body Propagation

t(sec)	X(m)	Y(m)	Z(m)	Vx(m/s)	Vy(m/s)	Vz(m/s)
0	-1207858.9402	6827112.5259	0	989.0423	174.9823	7515.5340
27.9572	-1179647.8538	6828812.9079	210080.6277	1028.9623	-53.3500	7512.0214
55.9144	-1150334.0744	6824129.9573	419964.8795	1067.9205	-281.6324	7501.4868
83.8716	-1119945.0034	6813068.0518	629456.5629	1105.8804	-509.6515	7483.9401
111.8288	-1088509.0474	6795637.5315	838359.8527	1142.8066	-737.1942	7459.3977
139.7861	-1056055.5918	6771854.6899	1046479.4733	1178.6645	-964.0478	7427.8824
167.7433	-1022614.9728	6741741.7584	1253620.8820	1213.4207	-1190.0002	7389.4239
195.7005	-988218.4495	6705326.8854	1459590.4503	1247.0426	-1414.8403	7344.0580
223.6577	-952898.1746	6662644.1103	1664195.6451	1279.4988	-1638.3578	7291.8271
251.6149	-916687.1642	6613733.3314	1867245.2088	1310.7589	-1860.3439	7232.7800
			⋮			
503.2298	-556539.0623	5902702.3272	3593989.1436	1533.8473	-3755.6880	6405.7939
			⋮			
1006.4596	259137.3926	3235111.7882	6126604.8870	1625.6780	-6577.2321	3404.3009
			⋮			
2012.9191	1442621.1277	-3896304.4192	5550319.1454	483.7198	-6133.5415	-4431.4515
			⋮			
3019.3787	1047786.6653	-6764918.6347	-1098364.5930	-1187.4583	1020.6292	-7418.9176
			⋮			
4025.8383	-493392.2903	-2232286.5090	-6545368.4062	-1559.4824	7058.1673	-2289.6214
			⋮			
5004.3406	-1487771.6994	4590182.5965	-4978468.3312	-275.2040	5529.6745	5180.6408
			⋮			
6010.8002	-898257.9936	6586956.2013	1968128.2305	1325.9315	-1970.6988	7200.7172
			⋮			
7017.2598	674006.3749	1377185.9886	6761468.8676	1476.4146	-7315.0039	1342.7566
			⋮			
8023.7193	1508865.4016	-5339312.1812	4157337.6506	11.6074	-4656.2351	-5984.2643
			⋮			
9002.2217	733583.0019	-6297925.5607	-2804705.8735	-1442.0473	2887.5391	-6861.1002
			⋮			
10008.6812	-843255.6632	-498862.8647	-6863559.0023	-1368.4519	7448.4966	-373.2501
			⋮			
11015.1408	-1497519.6347	5845987.2136	-3413247.1406	202.3159	3860.3306	6522.9589
			⋮			
11518.3706	-1179647.5231	6828812.8276	210082.9600	1028.9627	-53.3525	7512.0214

Table C.2: Validation Data for J2+Drag Propagation

t(sec)	X(m)	Y(m)	Z(m)	Vx(m/s)	Vy(m/s)	Vz(m/s)
0	-1207858.9402	6827112.5259	0	989.0423	174.9823	7515.5340
27.9572	-1179647.0843	6828808.5241	210080.4927	1029.0171	-53.6634	7512.0069
55.9144	-1150331.0264	6824112.4543	419963.8013	1068.0284	-282.2568	7501.4290
83.8716	-1119938.2215	6813028.7957	629452.9317	1106.0392	-510.5821	7483.8105
111.8288	-1088497.1412	6795568.0619	838351.2703	1143.0139	-738.4235	7459.1684
139.7861	-1056037.2454	6771746.7891	1046462.7732	1178.9174	-965.5659	7427.5265
167.7433	-1022588.9545	6741587.5197	1253592.1548	1213.7160	-1191.7948	7388.9152
195.7005	-988183.6192	6705118.7780	1459545.0762	1247.3770	-1416.8967	7343.3718
223.6577	-952853.4907	6662375.0416	1664128.3319	1279.8686	-1640.6594	7290.9400
251.6149	-916631.6889	6613396.7054	1867150.0348	1311.1604	-1862.8719	7231.6705
			⋮			
503.2298	-556362.3664	5901565.6360	3593300.1206	1534.3581	-3759.1655	6402.0504
			⋮			
1006.4596	259519.0801	3232951.3832	6122886.4041	1626.0127	-6576.9216	3397.0203
			⋮			
2012.9191	1444007.6122	-3895792.3542	5541256.7311	485.1294	-6131.2835	-4436.5721
			⋮			
3019.3787	1047790.6421	-6755393.4476	-1115267.0019	-1192.2895	1040.9796	-7422.4219
			⋮			
4025.8383	-498326.7997	-2203196.8208	-6547335.1127	-1562.6507	7065.3009	-2260.1043
			⋮			
5004.3406	-1493859.7161	4610230.7373	-4954404.9826	-274.3577	5508.2199	5199.9124
			⋮			
6010.8002	-900066.7430	6577037.0735	1998781.8424	1333.2381	-2005.5189	7189.3076
			⋮			
7017.2598	679269.1473	1344926.2058	6761534.5610	1481.9367	-7317.5114	1301.8138
			⋮			
8023.7193	1516701.7163	-5356215.8144	4120852.6615	9.5939	-4625.1956	-6013.3521
			⋮			
9002.2217	733319.1561	-6269708.7122	-2850837.0720	-1454.7729	2941.8940	-6841.5625
			⋮			
10008.6812	-854169.9351	-438276.0131	-6859769.5385	-1374.7507	7447.1529	-307.9622
			⋮			
11015.1408	-1509021.3278	5874312.0176	-3356735.6327	208.1896	3804.2428	6554.2779
			⋮			
11518.3706	-1186468.3112	6825337.0009	274338.7599	1041.3462	-121.2712	7509.5217